Reconstructing the attitude of the GRACE-FO mission based on fusion of star sensor, gyroscope and steering mirror data

MSc Thesis

Konstantinos Sfikas

Technische Universiteit Delft

TU Delft

Reconstructing the attitude of the GRACE-FO mission based on fusion of star sensor, gyroscope and steering mirror data

MSc Thesis

by

Konstantinos Sfikas

to obtain the degree of Master of Science
in Space Exploration at the Faculty of Aerospace Engineering
of Delft University of Technology,
to be defended publicly on Tuesday March 15, 2022 at 9:00 AM.

Student number:	4361369	
Thesis Committee:	Dr.ir. E.J.O. Schrama,	TU Delft, Committee chair
	Dr.ing. C. Siemes,	TU Delft, Supervisor
	Ir. C. de Wagter,	TU Delft, External examinator

An electronic version of this thesis is available at https://www.repository.tudelft.nl/

Cover photo: Courtesy of Airbus Space Systems

TU Delft Delft University of Technology

Preface

My mind hasn't fully realized it yet, but my student era is coming to an end. So many beautiful experiences, so many ups and downs, so many life lessons learned along the way. The final chapter of this exquisite journey is my MSc thesis work on the GRACE-FO attitude reconstruction. I guess what captivated me the most about this topic are the following two aspects: *attitude reconstruction* and *sensor data fusion*. Except from the fact that they represent two exciting areas of science and engineering, they also resemble a reflection of my journey within and without this thesis. The completion of this work wouldn't be possible without the presence and support of my family and my friends. I am really grateful for having you in my life, for all the love and strength that you are always giving me and all the life lessons that you are teaching me. You may not realise it, but you have been the perfect mirrors for me to see, to listen, to know and to understand myself. I would also like to express my deep appreciation to my supervisor Christian Siemes. Thank you for all the time that you have spent with me on this thesis, for your guidance and your heart-warming energy.

Konstantinos Sfikas
Delft, February 28, 2022

Abstract

On May 22, 2018, the Gravity Recovery and Climate Experiment Follow On (GRACE-FO) mission was launched with the goal to map the spatiotemporal variations in the Earth's gravity field and to extend the 15-year monthly mass change observations of its predecessor, the GRACE mission. Similarly to GRACE, the measurement principle of GRACE-FO is based on three different key elements, namely inter-satellite ranging, precise orbit determination and accelerometry. The accurate estimation of the satellites' attitude has an influence on all three of them. Therefore, any unmodeled errors in the attitude dataset product can propagate to the gravity field solutions and degrade the results. The objectives of this thesis are twofold. Firstly, to analyse the in-flight performance of the GRACE-FO star cameras, fiber-optic gyroscopes, accelerometers and steering mirrors. Secondly, to propose a method that accounts for the instruments' noise and errors and fuses the data, giving an improved attitude solution.

The noise and error characteristics of each instrument are determined by examining their measurements in the time and frequency domain, as well as investigating their differences in geographic plots. These analyses are performed for May 2020, when all instruments could provide nominal data. Motivated by the improved attitude quaternions and gravity field results that were obtained from the latest GOCE gradiometer data calibration process, the proposed on-ground attitude reconstruction for GRACE-FO is composed of three elements. The first one is the optimal combination of star camera and steering mirror quaternions by minimizing the weighted residual sum of squares of the elements of the noise quaternions. Within this combination, a set of constant parameters are also estimated that describe the relative alignment of these sensors. The second element is the reconstruction of the satellite angular rates in the frequency domain by applying respectively a highpass and a lowpass filter to the IMU and to the combined star camera and steering mirror derived angular rates. Lastly, the third element is the attitude reconstruction, for which attitude quaternions, resulting from the smooth reconstructed angular rates, are fitted to the optimally combined quaternions by means of a generalised least-squares adjustment.

The proposed attitude data fusion method produces an improved attitude solution that incorporates more accurately the noise and error characteristics of the star camera, the steering mirror and the IMU measurements. At the level of quaternions, it performs better than the official method, which is based on Kalman filtering, with noticeable improvements at frequencies above 10 mHz. However, based on a comparison of the corresponding derived antenna offset correction for range rate, very minor improvements are expected at the level of the gravity field. This is due to the K/Ka-band ranging system noise being the dominant source at the higher frequencies. The findings of this thesis work are valuable for the design of future gravity missions such as the Next Generation Gravity Mission proposed by ESA, for which a redundant accelerometer design is considered. Given the estimated noise characteristics of the above instruments and the proposed angular rate reconstruction method, the most favorable placement of the accelerometers is found to be in the along-track direction. If an accelerometer fails in this configuration, the noise in the required centrifugal and Euler acceleration corrections will be less than that of the laser ranging system.

Contents

List of Figures

List of Tables

List of Symbols

Latin symbols	Definition	Units
a	Change in average angular velocity or slope of noise PSD	[rad/s ; -]
$\mathbf{a}$	Measured linear or angular acceleration	[m/s^2 ; rad/s^2]
$\mathbf{A}$	Linear model that approximates the observation equations	[-]
$\mathbf{A}^+$	Penrose-Moore pseudo-inverse of matrix $\mathbf{A}$	[-]
$\mathbf{b}_i^{\mathrm{SCF}_i}$	Boresight vector of the i^{th} star camera expressed in the star camera frame	[-]
c	Speed of light	[m/s]
$\mathbf{e}_i$	Vector containing small rotation angles defined in the i^{th} star camera frame	[rad]
$\tilde{\mathbf{e}}_i$	Vector containing small rotation angles of the i^{th} star camera rotated in the common reference frame	[rad]
f	Focal length or frequency vector	[m ; Hz]
f_{SCAi}	Flags of quaternions for the i^{th} star camera	[-]
$\boldsymbol{F}_S$ and $\boldsymbol{F}_G$	Lowpass and highpass filter for the star camera and the inertial measurement unit angular rates	[-]
h_k	Weights for the Wiener filter at frequency k	[-]
$\mathbf{H}$	Sensor geometry matrix that describes the configuration of the redundant IMU system	[-]
I	Number of star cameras	[-]
$\boldsymbol{I}$	Identity matrix	[-]
k	Iteration counter or scale factor	[-]
K	Length of window during quaternion fitting	[-]
m_{Gi}	Angular rate measurement of gyro i	[rad/s]
$\mathbf{m}$	Measurement vector containing angular rates measured by each gyro of the inertial measurement unit	[rad/s]
$\mathbf{n}$	Unit vector representing the axis of rotation of a quaternion	[-]
N	Total number of epochs	[-]
N_F	Length of a filter	[-]
$\mathbf{P}_i$	Weight matrix that expresses the anisotropic measurement noise of camera i	[-]
$\boldsymbol{P}_S$ and $\boldsymbol{P}_G$	Noise PSD of the star camera and the inertial measurement unit angular rates	[-]
$\mathbf{q}$ or $\mathbf{Q}$ or Q	Quaternion	[-]
$\dot{\mathbf{q}}$	First time derivative of a quaternion	[-]
$\mathbf{r}$	Position vector of the satellite in inertial Earth-centered frame	[m]
$\mathbf{r}_{\mathrm{pc}}$	Center-of-mass to antenna phase center vector	[-]
$\mathbf{R}$	Rotation matrix	[-]
S	Weighted residual sum of squares	[-]
$\mathbf{s}^i$	Vector that describes the orientation of the i^{th} gyro axis in the satellite frame	[-]
t or $\mathbf{t}$	Time	[s]
v	Average angular velocity	[rad/s]
$\mathbf{W}_{A,B}^B$	Four dimensional vector that contains the angular rates describing the rate of rotation of the B-frame axes with respect to a stationary A-frame axes, resolved about the B-frame axes	[-]
x	Coordinate axis	[-]
$\mathbf{x}$	Vector representing the x axis of a reference frame	[-]
$\mathbf{X}$	The design matrix of a generalized least-squares adjustment	[-]

y	Coordinate axis	[-]
$\mathbf{y}$	Observation vector of a generalized least-squares adjustment or vector representing the y axis of a reference frame	[-]
z	Coordinate axis	[-]
$\mathbf{z}$	Vector representing the z axis of a reference frame	[-]

Greek symbols

$\boldsymbol{\beta}$	Parameter vector of a generalized least-squares adjustment	[-]
δ or ϵ	Small angle	[rad]
$\boldsymbol{\Delta}_{\text{ij}}$ or $\boldsymbol{d}_{\text{ij}}$	Vector containing small rotation angles from the difference of quaternion i and j	[rad]
Δt	Small increment of time	[s]
$\Delta\mathbf{G}^m$	Misalignment error in the gyroscope measurements	[rad]
$\Delta\mathbf{G}^k$	Scale factors in the gyroscope measurements	[-]
$\Delta\mathbf{G}^b$	Bias error in the gyroscope measurements	[rad/s]
θ	Arbitrary angle of rotation or pitch pointing angle	[rad]
ϕ	Absolute argument of latitude or yaw pointing angle	[rad]
σ^2_k	Variance at frequency k	[-]
σ^2_0	Posteriori variance factor	[-]
Σ	Covariance matrix	[-]
$\boldsymbol{\omega}$	Angular rate vector	[rad/s]
ω_{gi}	Angular rate measured by the i^{th} gyro	[rad/s]
$\boldsymbol{\omega}^B_{A,B}$	Angular rate vector describing the rate of rotation of the B-frame axes with respect to a stationary A-frame axes, resolved about the B-frame axes	[rad/s]

List of Abbreviations

ACC	Accelerometer
AF	Accelerometer Frame
AOC	Antenna Offset Correction
AOCS	Attitude and Orbit Control Subsystem
ARR	Angular Rate Reconstruction
ASD	Amplitude Spectral Density
ATTR	Attitude Reconstruction
BS	Beam Splitter
CCD	Charged Coupled Device
CHAMP	Challenging Minisatellite Payload
CMOS	Complementary Metal-oxide Semiconductor
CoM	Center of Mass
CRF	Common Reference Frame
DTU	Danmarks Tekniske Universitet
DWS	Differential Wavefront Sensing
DLR	Deutsches Zentrum Für Luft und Raumfahrt
EGG	Electrostatic Gravity Gradiometer
ESA	European Space Agency
FOG	Fiber-optic Gyroscope
FoV	Field of View
FPGA	Field Programmable Gate Array
FSM	Fast Steering Mirror
GFZ	GeoForschungsZentrum
GGT	Gravity Gradient Tensor
GNSS	Global Navigation Satellite System
GOCE	Gravity field and steady-state Ocean Circulation Explorer
GPS	Global Positioning System
GRACE	Gravity Recovery and Climate Experiment
GRACE-FO	Gravity Recovery and Climate Experiment Follow-On
GRF	Gradiometer Reference Frame
IBA	Inter-boresight Angle
ICRF	International Celestial Reference Frame
I-FOG	Interferometric Fiber-optic Gyroscope
IMU	Inertial Measurement Unit
IPU	Instrument Processing Unit
JPL	Jet Propulsion Laboratory
KBR	K-band Ranging
KF	K-Frame
LOSF	Line of Sight Frame
LRI	Laser Ranging Interferometer

LRP	Laser Ranging Processor
μASC	Micro Advanced Stellar Compass
MWI	Microwave Instrument
NEA	Noise Equivalent Angle
NGGM	Next Generation Gravity Mission
OBA	Optical Bench Assembly
OBC	On-board Computer
OBE	Optical Bench Electronics
PhC	Phase Center
PSD	Power Spectral Density
QPR	Quadrant Photo-receiver
SCA	Star Camera
SCF	Star Camera Frame
SDS	Science Data System
SF	Satellite Frame
SRF	Science Reference Frame
STR	Star Tracker Assembly
SuperSTAR	Super Space Three-axis Accelerometer for Research
TMA	Triple Mirror Assembly
TTL	Tilt-To-Length
USO	Ultra-stable Oscillator
UTCSR	University of Texas Center for Space Research

1 Introduction

Over the past two decades, dedicated gravity field space missions improved significantly our knowledge of the Earth's gravity field, both in terms of accuracy and spatial resolution. The gravity field acts as a mirror into the Earth's interior. From the comparison of corresponding measurements with solutions from an idealised Earth model in hydrostatic equilibrium, gravity anomalies can be derived, which in turn can give an indication of mass imbalanced states in the interior of the Earth as well as increase the understanding of the Earth's dynamics [Rummel et al., 2002]. Satellite gravimetry facilitated for the first time measurements of a homogeneous and worldwide gravity dataset and advanced our knowledge of mass distribution and mass change processes in the Earth system. This in turn had a significant benefit to the fields of continental hydrology, oceanography, cryospheric, solid Earth and atmospheric sciences [Pail et al., 2015].

In 2000, the German Challenging Minisatellite Payload (CHAMP) mission was the first one to allow the scientific community to derive large-scale static gravity fields. Since the launch of the US/German Gravity Recovery and Climate Experiment (GRACE) mission in 2002, monthly gravity field estimates were also produced and observations of the seasonal and long-term variations in the gravity field could be made. Later on in 2009, with the launch of ESA's Gravity Field and Steady-State Ocean Circulation Explorer (GOCE) spacecraft, mean Earth gravity field estimates at high spatial resolution could be determined. In 2012, with the GRACE satellites already exceeding their nominal mission duration of five years, the GRACE Follow-on mission was formed. Its main objective is to provide continuity in monitoring the variations of the Earth's gravity field over time and extend the record initiated by the GRACE mission [Kornfeld et al., 2019].

For all the above-mentioned gravity field missions, the accurate estimation of the satellites' attitude plays one way or another a critical role in achieving their mission objectives. For example, for GOCE the former is essential for the precise calibration of the gradiometer and for extracting the gravity gradients [Stummer et al., 2012]. For GRACE and GRACE-FO, however, their measurement principle is based on three different key elements, namely precise orbit determination, accelerometry and inter-satellite ranging. And as a matter of fact, the on-ground final attitude solution has an influence on all three elements, i.e. it affects the calibration of K-Band ranging (KBR) and star camera parameters, the rotation of the accelerometer data and of the GPS phase center offset vector in the celestial reference frame and the determination of the inter-satellite pointing. Specifically, the latter is essential for the estimation of the gravity field, because the inter-satellite KBR measurements must be related to the center of mass (CoM) of each satellite. This is achieved by applying a geometric correction, called the antenna offset correction (AOC), depicted in Figure 1.1, which corrects not only for the offset of the KBR antenna phase center (PhC) from the CoM, but also for any imperfect pointing between the satellites. The AOC depends on the estimated relative attitude of the satellites, therefore, any unmodeled errors in the estimation can propagate to the gravity field solutions and degrade the results [Bandikova, 2015].

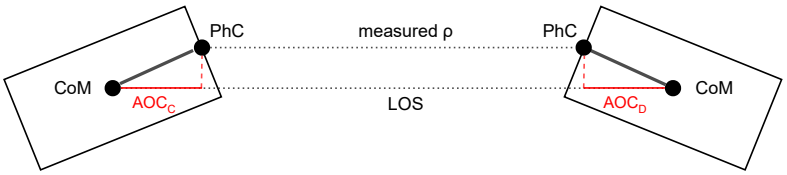

Figure 1.1: Antenna offset correction for range for the GRACE-FO satellites.

Additionally, knowledge about the noise and errors in the reconstructed satellite attitude and angular rates could be of great importance for the design of the Next Generation Gravity Mission (NGGM) proposed by ESA. The intended measurement principle of NGGM is the same as with GRACE and GRACE-FO, i.e. based on inter-satellite ranging, but now two accelerometers will be placed symmetrically around the satellites' CoM [Haagmans et al., 2020]. In case one of them fails, the measurements of the other accelerometer have to be corrected for gravity gradient, centrifugal and Euler effects in order to obtain the non-gravitational accelerations. In fact,

the last two effects are computed given the satellite angular rates. To achieve an accurate estimation of the latter and to ensure that the noise in the required centrifugal and Euler acceleration corrections are not affecting the mission objectives, a comprehensive understanding of the performances of the relevant instruments is necessary as well as a method that can fuse their measurements in the most optimal way. In this MSc thesis, the focus lies on the accurate on-ground attitude reconstruction of the GRACE-FO mission.

Already for CHAMP, GRACE and GOCE, a considerable amount of research has been invested in analysing and improving the satellites' attitude estimates. This includes either better calibration, noise and error modelling of the on-board attitude sensors (e.g. [Harvey, 2016]) or on-ground attitude reconstruction methods based on the fusion of measurements from the star cameras and from other instruments that contain attitude information. For example, for GOCE, in the early stages of the mission a Kalman filter approach, that combined star camera and gradiometer data, was utilized to reconstruct the angular rates and the attitude quaternions [Castini & Cesare, 2008]. Later on, however, an angular rate reconstruction method was developed that combined data from the two instruments using Wiener filtering, the result of which was then used for reconstructing the attitude of the satellite based on a generalised least squares adjustment method [Siemes, 2018]. In fact, the outcome of the latter was found to be better than the one obtained from the original method. As far as the GRACE mission is concerned, a variance component estimation method was initially introduced that fused together star camera and accelerometer data [Klinger & Mayer-Gürr, 2014]. A few years later a Kalman filter approach was developed, that combined again data from the same instruments, but based on their improved error models [Harvey & Sakumura, 2019]. This method is now adopted by the GRACE-FO mission, but with the modification of using measurements from the on-board fiber-optic gyroscopes instead of the accelerometer.

Nevertheless, no detailed analysis has been published yet on the performance of the latter method, on the contribution of each sensor to the final attitude estimate, as well as on the error and noise characteristics of the sensors' measurements. In addition, considering that between the gravity missions different attitude reconstruction approaches have been employed, it poses the question of which one accounts better for the instruments' noise and achieves a better solution for GRACE-FO. At the same time, the twin satellites of GRACE-FO are equipped with the laser ranging interferometer (LRI), which has the same function as the microwave instrument (MWI), i.e. it is used to measure the fluctuations in the separation between the two satellites. A key component of the interferometer is the fast steering mirror assembly, which is responsible for aligning the local and the incoming laser beam so that the maximum heterodyne efficiency can be achieved. On this basis, additional attitude information could be derived from the steering mirror commanded angles.

In this MSc thesis, the noise and error characteristics of the GRACE-FO star cameras, fiber-optic gyroscopes, accelerometers and steering mirrors will be analysed. To avoid any confusion the following definitions of *noise* and *error* are used within this work: *noise* corresponds to random effects in the data in comparison to *errors* that refer to non-random, or systematic, effects that could be modeled by a set of parameters. Additionally, appropriate calibration and data fusion methods will be proposed that ensure any significant systematic errors in the measurements are correctly accounted for and an improved attitude dataset can be provided. The performance of the new attitude reconstruction method will be compared to the official one, which is based on Kalman filtering. Finally, the impact of the proposed approach on the GRACE-FO mission will be addressed and given the estimated noise characteristics of the above instruments, a recommendation will be given for NGGM.

The report is structured in the following way. In Chapter 2, an overview of the GRACE-FO mission is given, together with its objectives and its measurement concept. In the same chapter, a description of the measurement principle and the current performance of the star cameras, the fiber-optic gyroscopes, the accelerometer and the steering mirrors is provided. Chapter 3 reviews the previous research conducted on satellite attitude reconstruction with a focus on the GRACE and GOCE missions. At the end of this chapter, the research gap is identified and the main research question and sub-questions are derived. Next, in Chapter 4, four main processing algorithms are described, that were implemented during this thesis as building blocks for the instruments' error assessment and for the attitude reconstruction process. Afterwards, Chapter 5 explains the various proposed methods for calibrating and combining the measurements of the instruments under consideration, and Chapter 6 presents the verification of the previously-mentioned algorithms. Then, in Chapter 7 the identified noise and error characteristics of each instrument are addressed and the results obtained from the data calibration and the data fusion methods are analysed. Within this chapter, the solution of the proposed attitude reconstruction method is compared to the one acquired from the official attitude data product. At the end, the impact of the new attitude solution on the GRACE-FO mission is discussed and a recommendation is given for NGGM. Finally, Chapter 8 provides detailed conclusions, that answer the research question, and recommendations for future work.

2

GRACE Follow-On Mission

This chapter provides an overview of the GRACE-FO mission in terms of its objectives (Section 2.1) and its measurement concept (Section 2.2). In Section 2.3 follows a description of the four instruments on-board the satellites that could be used for reconstructing the satellites' attitude. Lastly, Section 2.4 presents the mission data products that were utilized in this thesis work.

2.1. Overview & Objectives

The GRACE-FO (Gravity Recovery and Climate Experiment Follow-On) mission, is a joint US/German space mission launched in May 2018 with a designed lifetime of 5 years and the goal to map the spatiotemporal variations in the Earth's gravity field and to extend the 15 year monthly mass change observations of its predecessor, the GRACE mission, which was decommissioned in June 2017. The two missions share many similarities, such as the measurement concept, the spacecraft design and several instruments, but GRACE-FO incorporates numerous improvements based on the lessons learned from GRACE. Each of the GRACE-FO satellites is equipped with three star trackers, one inertial measurement unit (that consists of four fiber-optic gyroscopes), a precise accelerometer in the satellite's CoM, magnetorquers, cold-gas thrusters, the GNSS receiver assembly and the MWI. In addition, a change in the design of the satellites had to be made to accommodate the LRI, which is used to demonstrate the first-ever satellite-to-satellite ranging laser interferometry [Landerer, Flechtner, et al., 2020]. In Figure 2.1 an artist's rendering of the twin GRACE-FO spacecraft is shown in orbit around the Earth. The MWI ranging is indicated by the white line that connects the two satellites, while the laser ranging by the two red lines, which are separated to achieve the "race-track" configuration (explained in more detail in Section 2.3.4).

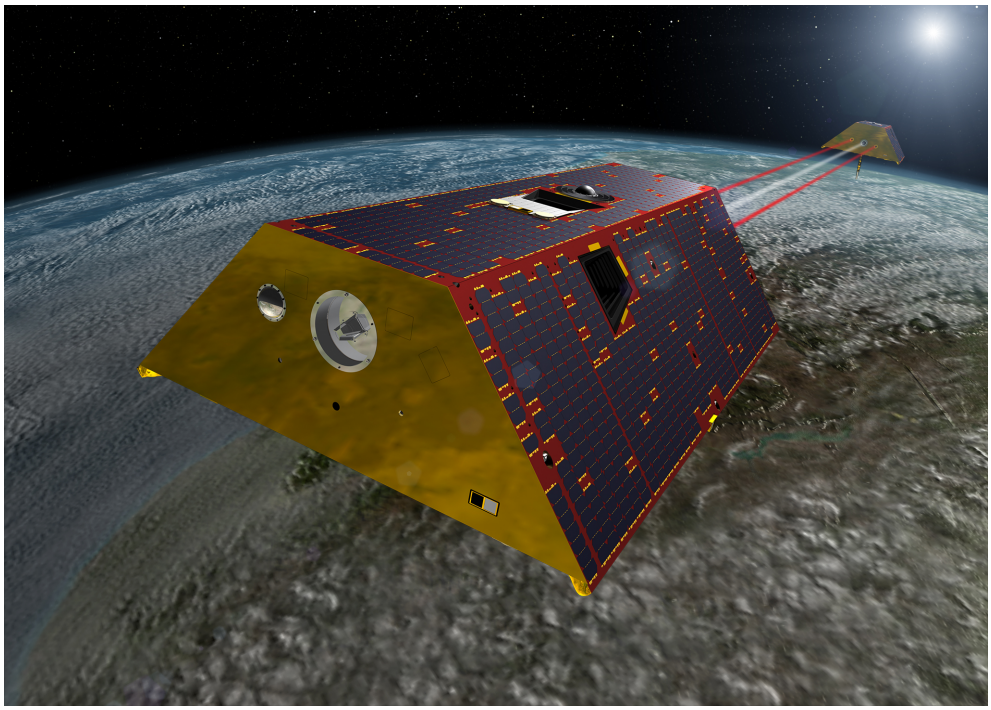

Figure 2.1: An artist's impression of the two GRACE-FO satellites in orbit around Earth. Source: [NASA/JPL-Caltech, 2020]

As underscored in the 2018 Decadal Strategy for Earth Observation from Space, the mass change observations are one of the most significant measurements to continue obtaining in the next decade [National Academies of Sciences, Engineering & Medicine, 2018]. The main science objective of the GRACE-FO mission is to continue monitoring the variations of the gravity field over time, i.e. to extend the record that was initiated by the GRACE mission. As with its predecessor, this objective is achieved by measuring precisely the range between two spacecraft. In addition to the monthly gravity field maps, the GRACE-FO mission will continue atmospheric profiling observations from GPS radio occultations that can be used to support weather forecasting (e.g. [Anlauf et al., 2011; Kornfeld et al., 2019; Pingel et al., 2010]). Last but not least, the GRACE-FO satellites are demonstrating the LRI design as a means to improve the performance of satellite-to-satellite range measurements, and thus serving as a pathfinder for future GRACE-like geodetic missions [Wen et al., 2019].

2.2. Measurement Concept

The measurement concept of the GRACE-FO mission is equivalent to that of GRACE, i.e two identical satellites are in near-polar orbits, with a separation in the along track direction between 170 to 270 km and at an initial altitude of about 491 km. Over the course of the mission, the orbits of the satellites are allowed to decay, however, systematic orbit maintenance maneuvers are performed to keep the satellites at the nominal separation distance between 170 and 270 km. Similar to GRACE, the two satellites are equipped with a dual frequency K/Ka-band MWI that measures variations of the inter-satellite range due to orbital perturbations arising from temporal and spatial changes in the gravity field of Earth. In parallel to the MWI, the LRI also measures range variations, which are later used to compare the two ranging observations.

While in orbit, any gravitational and non-gravitational forces experienced by the twin spacecraft will change the distance between them. Non-gravitational forces include among others solar and Earth radiation pressure, atmospheric drag and residual imbalanced thruster firings. These accelerations are measured by the on-board accelerometer on each satellite and later on they are used so that variations in the inter-satellite range caused by purely gravitational forces can be precisely distinguished. Furthermore, the on-board GPS receivers enable precise orbit determination and time tagging necessary for the data analysis.

There are four main error contributors when deriving gravity field models from GRACE-FO observations, namely the inter-satellite range measurement errors, the non-gravitational acceleration measurement errors, the precise orbit determination errors, aliasing due to spatial and temporal under-sampling, and errors in the models used for de-aliasing. The on-ground attitude estimate plays has key role for both the KBR and the accelerometer. For the observations of the former, a geometric correction needs to be applied (see Figure 1.1), so that the offset of the KBR antenna PhC from the CoM as well as any imperfect pointing between the satellites are corrected. For the accelerometer, the measured accelerations need to be accurately projected along the CoM-CoM line. Therefore, any unmodelled noise and errors in the attitude product can contribute to the inter-satellite range and non-gravitational acceleration measurement errors [Kornfeld et al., 2019].

2.3. Attitude Sensors and Instruments

In this section, a description is provided for the four instruments on-board the GRACE-FO satellites, that can either measure the inertial or the relative satellite attitude and could be used for the attitude reconstruction process. These instruments include the star cameras (Section 2.3.1), the inertial measurement unit consisting of fiber-optic gyroscopes (Section 2.3.2), the accelerometer (Section 2.3.3) and the steering mirrors of the LRI (Section 2.3.4). For each one of them, the measurement principle, the accuracy and the corresponding mission data products are presented.

2.3.1. Star Tracker Assembly

A star camera is one of the most important attitude determination sensors on-board a satellite and especially for the two GRACE-FO satellites, as they provide the most accurate inertial attitude information of a spacecraft. As the name suggests, the sensor uses stars as the reference objects for attitude determination. A star camera measurement involves capturing a picture of the stars in the field-of-view (FoV), identifying them using an on-board star catalog and in the end determining the attitude of the sensor frame with respect to the inertial frame in terms of quaternions [Bandikova, 2015]. A star camera is essentially a digital camera, which is populated by either charge coupled device (CCD) or complementary metal-oxide semiconductor (CMOS) pixels and has a focal plane that is found at a distance f (focal length) behind the vertex. With the vertex of the optical system

as the origin, an *x*-*y*-*z* coordinate system is defined with the *z* axis being along the optical, or otherwise called boresight axis [Markley & Crassidis, 2014]. In Figure 2.2, the basic geometry of a star camera is depicted.

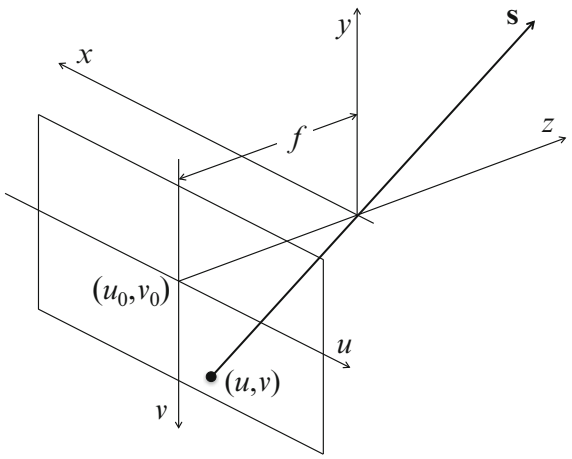

Figure 2.2: Star camera geometry. Source: [Markley & Crassidis, 2014]

The point where the optical axis touches the focal plane is designated by (u_0, v_0) and the focal plane makes use of a (u,v) coordinate system. The vector **s** is defined as the unit vector from the spacecraft to a star and can be computed from the focal plane coordinates of the centroid of its image as: [Markley & Crassidis, 2014]

$$\mathbf{s} = \frac{1}{\sqrt{f^2 + (u-u_0)^2 + (v-v_0)^2}} \begin{bmatrix} u-u_0 \\ v-v_0 \\ f \end{bmatrix} \tag{2.1}$$

Both GRACE-FO satellites are equipped with three star cameras. More specifically, they are supplied with the Micro Advance Stellar Compass (μASC) Star Tracker Assembly (STR), which was designed and built by the Technical University of Denmark (DTU). In general, the performance of a star tracker can be affected by several factors, among others the sensitivity to starlight, the size of the FOV, the accuracy of the star centroiding and the number of stars in FOV. Figure 2.3 shows an error breakdown for a typical star tracker.

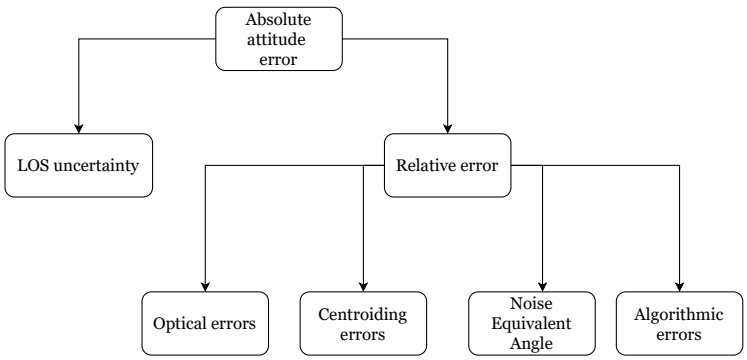

Figure 2.3: Star camera attitude error breakdown.

The absolute attitude error is the overall star tracker error with respect to its mounting plane and it is subdivided into two categories: the relative error and the line of sight (LOS) uncertainty. The former is further categorized to optical errors, centroiding errors, Noise equivalent angle (NEA) and algorithmic errors. LOS uncertainty refers to any excursion caused by thermal drift, launch effects, ground calibration residuals, etc. As the name suggests, optical errors include any ground calibration errors related to the optics as well as chromatic, thermal and optical distortion. Centroiding errors include centroid algorithm uncertainty, quantization error and pixel light sensitivity non-uniformity. NEA refers to the ability of a star camera to replicate the same attitude given an identical optical stimulation. This errors consists of dark current noise, photon noise, readout

noise and stray light noise. Last but not least, algorithmic errors consist of star catalog, thresholding and time stamp uncertainties as well as any other algorithmic approximations [Eisenman & Liebe, 1998; Liebe, 2002].

The NEA of a star tracker can be split into the cross-boresight and the boresight NEA, referring to how accurate the rotations around each axis of the camera frame can be resolved. In general, a star tracker will be 6-16 times more accurate in the cross-boresight axes [Liebe, 2002]. Based on the specifications of the (μASC) cameras, the latter axes can be measured with an accuracy of 2 arcseconds [Jørgensen et al., 2012]. At the same time, according to Landerer, Flechtner, et al. [2020], the RMS point-by-point noise for camera 1 of GRACE-FO was estimated, via an attitude Kalman filter, to be equal to 1.6, 1.4 and 28 arcseconds for the cross-boresight and the boresight axes respectively. In addition to random noise, star tracker measurements are prone to systematic errors such as the drift, that was observed for GRACE, on the orientation of the cameras during the lifetime of the mission. This drift was on the order of hundreds of arcseconds and was attributed to thermal conditions [Harvey, 2016]. For the GRACE-FO satellites to comply with the thermal requirements, the three camera heads are mounted to a silicon carbide cube that provides both structural and thermal stability. Another important systematic effect that was found for GRACE, was FoV dependent errors.

As far as the star camera operation on-board the satellites is concerned, each one provides measurements with approximately 2 Hz sampling rate. The SCA1A data product contains these measurements, which express the rotation between each of the three star camera frames (SCFs) and the inertial frame. The measurements can be defined with respect to the science reference frame (SRF), which is aligned with the main satellite axes, using the QSA1B data product that includes the quaternions that describe the rotation between each of the three SCFs and the SRF. For the full definition of the above reference frames, the reader is referred to Appendix A.2. The noise modelling performed for GRACE is used for the GRACE-FO mission as well. As indicated by Wen et al. [2019], star camera noise is modelled "as point-by-point white noise, FoV dependent noise and alignment error on each camera".

2.3.2. Fiber optic gyroscopes

A gyroscope is a device for maintaining the orientation or measuring the angular rates of a system. The GRACE-FO gyroscopes are used to achieve the latter. Compared to other means of measuring angular rates, such as angular accelerometers, the gyroscopes have proved to be the most accurate for purposes of navigation [Jekeli, 2001]. In general, there are three main categories of gyroscope technologies, namely spinning mass, optical and vibratory [Groves, 2008]. Each GRACE-FO satellite is equipped with optical gyros, more specifically, with four fiber-optic gyroscopes (FOG) in tetrahedral configuration [Wen et al., 2019]. This type of gyro measures the phase difference of two light beams that travel through a loop of fiber optic. The measurement principle is based on the Sagnac effect, which occurs when light travels around a closed-loop waveguide, which itself is rotating about an axis perpendicular to its plane. From the perspective of an inertial frame, if the light propagates in the same direction as the rotation of the waveguide then the light-path length is increasing. On the contrary, if the waveguide is rotating in the opposite direction, the light-path length is decreasing. The angular rate of the waveguide with respect to an inertial frame can then be determined by measuring the changes in path length [Groves, 2008].

The gyros compose what is called the Inertial Measurement Unit (IMU) of the satellite. The GRACE-FO satellites carry the Astrix 120 IMU manufactured by Airbus Defence and Space [Gath, 2016]. The IMU, apart from directly measuring the angular rates, is used to propagate the attitude of the spacecraft between star camera measurements [Kornfeld et al., 2019]. The optical gyroscope is a single degree-of-freedom instrument, hence at least three gyros are required to provide a three-dimensional reference for attitude and measure all three angular rates. Since the sensing principal of optical gyros is based on light, and because it has no mass, nominally the dynamics of the environment, within which the gyroscope operates, do not affect the measurements [Jekeli, 2001]. However, there are situations, for instance at attitude thruster firings, when the instrument has short outages.

The IMUs are performing with high accuracy in high frequency band, however, their measurements in low frequency band are limited by the stability of bias and scaling factors [Bandikova, 2015]. Table 2.1 shows the performance specifications as provided by the supplier. The main noise contributor for the Astrix 120 IMU is the angle random walk with a magnitude of about $0.0016^\circ/\sqrt{h}$ [Airbus Defense and Space, 2020]. As mentioned by Wen et al. [2019], the noise of the IMUs is "modeled with bias random walk, once-per-revs and twice-per-revs model". Two IMU data products are provided for the GRACE-FO mission, the IMU1A and IMU1B. Both of them contain filtered angles resolved in the individual gyro frames at a sampling rate of 8 Hz. The filter used is "a predetermined but selectable 2nd-order low-pass filter". The only difference between the two products is that IMU1A is given in OBC Time, while IMU1B in GPS Time [Wen et al., 2019]. For the full definition of these

time frames, the reader is referred to Appendix A.1

Table 2.1: Performance of the Astrix 120 IMU. Source: [Airbus Defense and Space, 2020]

General	
Full performance measurement range	$\pm 10°/s$
Measurement range	up to $\pm 140°/s$
Scale factor knowledge and stability	
Linearity over full performance range	3σ < 10 ppm
Thermal modelling error	3σ < 10 ppm
Bias knowledge and stability	
Stability over 1 hour	$3\sigma < 0.01°/h$
Thermal modelling error	$3\sigma < 0.03°/h$

2.3.3. SuperSTAR Accelerometer

The purpose of an accelerometer is to measure the non-gravitational forces acting on a satellite. Such forces include the solar radiation pressure, atmospheric drag, Earth radiation force, thermal forces and even forces created by the attitude control system. For the GRACE-FO mission it is essential that these forces are measured as accurate as possible so that variations in the inter-satellite range caused by purely gravitational forces can be precisely distinguished. To minimize the coupling of rotational accelerations, such as Euler and centrifugal accelerations, and only measure non-gravitational forces, the accelerometer is placed at the center of gravity of each satellite [Kornfeld et al., 2019]. The two GRACE-FO satellites are equipped with the SuperSTAR, which stands for Super Space Three-axis Accelerometer for Research [Touboul et al., 2009]. It is supplied by ONERA and is based on a family of accelerometers previously used by the GOCE, the CHAMP and the GRACE mission, but it incorporates a number of improvements [Kornfeld et al., 2019]. The measurement principle of the SuperSTAR is based on the electrostatic levitation of a proof mass within a cage made up of six electrode pairs. These electrodes play the role of capacitive sensors and electrostatic actuators. When a non-gravitational force acts on the satellite, the cage is displaced with respect to the proof mass. Then, the electrodes, functioning as sensors, measure their instantaneous capacity, which varies with the position of the proof mass with respect to the electrodes. The measured displacement signal is sent to a proportional integral derivative (PID) controller to determine the control voltages to apply to the electrode pairs. The electrodes, functioning as electrostatic actuators now, apply the necessary electrostatic force to recenter the proof mass inside the cage [Gomez et al., 2007; Touboul et al., 2004].

Figure 2.4 shows the noise sources of the acceleration measurements along the satellite to satellite axis determined on-ground for SuperSTAR. As it can be seen from the figure, above 0.1 Hz, the main noise source is the capacitive detector noise, between 0.1 mHz to 0.1 Hz is the measurement chain noise and below 0.1 mHz is the temperature stability around the accelerometer [Christophe et al., 2015]. At the same time, Kornfeld et al. [2019] mentioned that "the achieved on-ground acceleration tone errors are 1.64×10^{-10}, 2.96×10^{-12} and $2.49 \times 10^{-12} m/s^2$ for the X, Y, and Z axes of one accelerometer unit, and 1.53×10^{-10}, 2.64×10^{-12} and $2.78 \times 10^{-12} m/s^2$ for the other unit, respectively."

The GRACE-FO C accelerometer is performing as good or slightly better in-orbit, than the ones of GRACE. In contrast, for GRACE-FO D, as of 21 June 2018, the accelerometer is under-performing, with the its measurements being degraded due to bias jumps and noise, which is highly correlated across all six accelerometer axes. Although, it can still measure non-gravitational accelerations, these measurements cannot be used to estimate Earth's gravity field. For this reason, an accelerometer data transplant is implemented that models and predicts the GRACE-FO D non-gravitational accelerations by making use of GRACE-FO C accelerometer observations and GRACE-FO D thruster information [Landerer, Flechtner, et al., 2020].

In addition, both accelerometers experience phantom accelerations, which denote large and spurious accelerations and of unknown origins. So far it was observed that they occur away from thruster firings and reveal geographical and beta-angle correlations. The beta-angle is defined as the angle between the satellite orbit and the vector to the Sun. The latest hypothesis assumes that the phantom accelerations are internal accelerations,

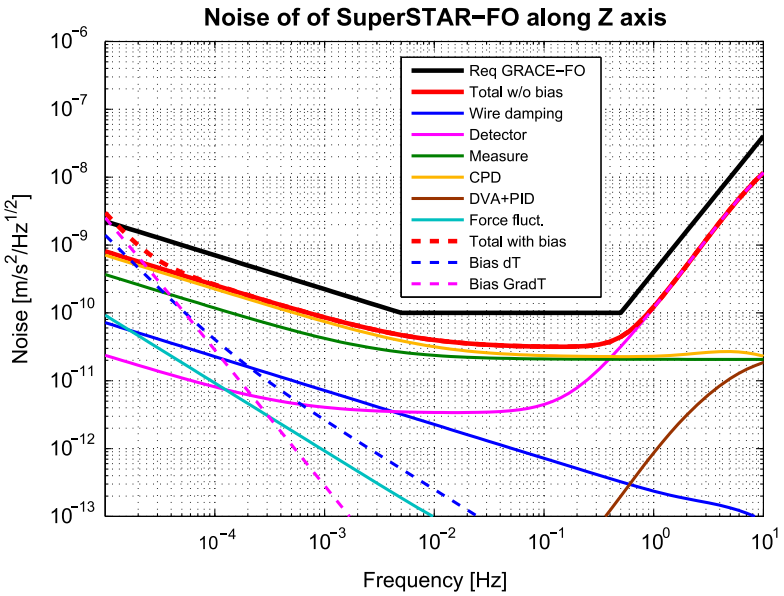

Figure 2.4: SuperSTAR accelerometer worst case performance along the z-axis of the accelerometer. Source: [Christophe et al., 2015]

which are aliased into the nominal measurements when the analog signals are converted into digital. Because they can have a large magnitude and do not always integrate to zero and as a consequence they can deteriorate gravity field estimates, they need to be removed. The latter is achieved by removing any outliers, which are defined as data with a deviation from the mean exceeding a predefined threshold. Then, any gaps in the data are filled with a linear interpolation [McCullough et al., 2019].

Finally, the SuperSTAR provides the measured angular and linear acceleration components of the proof mass in the accelerometer frame (AF), at 10 Hz. These measurements can be found in the ACC1A data product. Housekeeping data are found in the AHK1A and AHK1B data products. The difference between the two is that time-tags of the latter is in GPS, instead of OBC Time [Wen et al., 2019].

2.3.4. Laser Ranging Interferometer

The LRI is the first heterodyne laser interferometer operated between two distant spacecraft and it was added to the GRACE-FO mission as technology demonstrator in support of future gravity missions. Similar to the MWI, it is used to measure the variations in the distance between the two satellites [Sheard et al., 2012]. In Figure 2.5 the optical layout of the LRI is shown.

For an interferometer instrument, light is transmitted from a single source and split into two beams which propagate in different optical paths. Then, the two are combined to produce an interference. When the two beams have close frequencies then a heterodyne beat note is created [Saptari, 2003]. For the GRACE-FO LRI, light from the laser is routed through the 2-axis fast steering mirror and is split by the beam splitter (BS) into two beams of 10% and 90% intensity of the original beam. The 10% is used as the local oscillator that enables heterodyne detection of the received light. The incoming light first passes through an aperture before arriving at the BS. Both the local and the incoming laser beam are then imaged, with a two-lens imaging system, onto a quadrant photo-receiver (QPR). The other 90% of the local laser beam passes through the triple mirror assembly (TMA), whose goal is to direct the laser light around the microwave ranging assembly and the cold gas fuel tanks. The TMA consists of three mirrors in a corner cube reflector arrangement, i.e. the three mirror planes are perpendicular with respect to each other. This design has the special property of allowing the vertex point of the retro-reflector (the intersection point of the three mirror planes) to be located outside the mirror device. This, in turn, lets the fiducial measurement point to align with the CoM of the two satellites [Sheard et al., 2012].

In the nominal spacecraft fine-pointing mode, the LRI requires a higher pointing accuracy compared to the one that is achieved solely from the spacecraft attitude and orbit control system. To attain the higher precision, the fast steering mirror assembly and the QPR measurements are used in a feedback loop. The latter can measure the misalignment between the local and the incoming laser beam using the differential wavefront

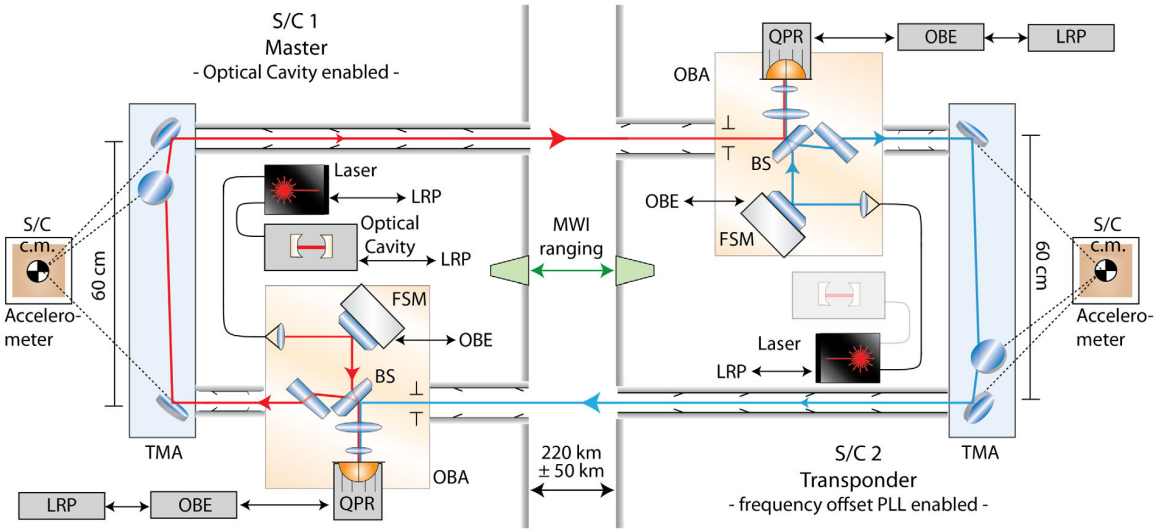

Figure 2.5: Optical layout of the laser ranging interferometer. Source: [Abich et al., 2019]

sensing (DWS) technique.

Lastly, Sheard et al. [2012] indicated that the two primary noise sources for the LRI measurements are the laser frequency noise and the pointing-induced noise. At lower frequencies, the LRI sensitivity was designed to be limited by tilt-to-length (TTL) coupling. This effect originates from the satellite attitude jitter together with coupling factors of a few 100 μm/rad arising from alignment tolerances [Abich et al., 2019]. As far as the performance of the steering mirrors is concerned, Schütze et al. [2014] have confirmed that the proposed beam steering method can accomplish an inter-satellite laser interferometer link with beam pointing error of less than 10 μrad and stability of 10 μrad/$\sqrt{\text{Hz}}$ at 0.002 to 0.1 Hz. In addition, Wegener et al. [2020] stated that quantization noise of the steering mirror readout limits the resolution of the measured and down-linked yaw and pitch angles to about 1 μrad/$\sqrt{\text{Hz}}$ for each axis. The LRI steering mirror measurements are contained in the LSM1A data product and are defined in LRI Time and in LRI field programmable gate array (FPGA) Frame. It should be noted that the steering mirror only provides yaw and pitch angles. The LSM1B data product corresponds to 10-Hz LRI steering mirror data, which describe the laser pointing to the other spacecraft, in the SRF with time-tags in GPS Time [Wen et al., 2019].

2.4. Data products

The Science Data System (SDS) of GRACE-FO processes, archives, verifies and distributes the telemetry and science data of the satellites. It includes the Jet Propulsion Laboratory (JPL), the University of Texas Center for Space Research (UTCSR) and the German Research Center for Geosciences (GFZ). The SDS is organized into three sequential processing levels, with each one producing its corresponding data product. The Level-1A through Level-3 data products are made available to the scientific community and can be retrieved from the Physical Oceanography Distributed Active Archive Center (PO.DAAC) of JPL [JPL GRACE-FO project, 2019]. The processing levels that are of interest for this thesis are listed below [Wen et al., 2019]:

- **Level-1A** data is the product from a "non-destructive" processing applied to Level-0 data (raw spacecraft and instrument telemetry data). More specifically, engineering units are derived from the binary encoded measurements, data is time tagged to the corresponding satellite receiver clock time and quality control flags are included.
- **Level-1B** data involves a further processing to Level-1A data to a point where a reversion to the previous state is not possible. That is to say, data is filtered, down-sampled to a lower rate and re-tagged or re-sampled to GPS Time. The Level-1A and Level-1B processing is collectively called Level-1 processing.

Within these two levels, there are several data products that are important for reconstructing the attitude of the GRACE-FO satellites and assessing its performance. A few of them have already been mentioned in Section 2.3, but in Table 2.2 an overview of all that were used during this MSc project is given.

Table 2.2: Overview of all data products that have been used within this MSc project.

Data product	Content
	Level-1A
SCA1A	Quaternions, star camera ID, quality flags
IMU1A	Angle measurements, gyro ID, quality flags
ACC1A	Angular acceleration in accelerometer frame
	Level-1B
SCA1B	Quaternions from Inertial frame to SRF
LSM1B	Pitch and yaw pointing angles
QSA1B	Quaternion rotation from individual SCF to SRF
GNI1B	Trajectory states in Inertial frame
GNV1B	Trajectory states in Earth-fixed frame
CLK1B	Clock offsets for conversion from Receiver to GPS Time
TIM1B	Clock mapping from OBC to Receiver Time
THR1B	Thruster activation data
VKB1B	KBR Antenna Phase Center Location

3

Previous Research in Satellite Attitude Reconstruction

This chapter is dedicated on the various methods and techniques that have been used so far on the satellite attitude reconstruction of gravity missions. Specifically, the focus is placed on the GRACE (Section 3.1) and GOCE (Section 3.2) missions, for which a considerable amount of research has already been performed. In fact, the latest attitude reconstruction approach developed for GRACE is also used for its successor. Next, in Section 3.3, based on the findings of previously-mentioned sections and of Section 2.3, a research gap is identified. Finally, in Section 3.4 the research objective and the research questions for this MSc thesis are formulated.

3.1. GRACE

Up until 2014, analysis performed on GRACE combined star camera data reported an unexpectedly higher noise. Their impact on the processing of the accelerometer data and the K-band ranging prompted Bandikova and Flury [2014] to re-examine the star cameras' official processing method. They independently derived the official method and implemented an additional one that merges only the well determined star tracker boresight directions. The former method is based on the approach presented by Romans [2003], for which multiple star cameras are combined in an optimal way by minimizing the weighted residual sum of squares of the elements of the star cameras noise quaternions. Based on this, the optimal quaternions for two star cameras is equal to

$$\mathbf{Q}^* = \tilde{\mathbf{Q}}_1\left(1, \frac{1}{2}(\tilde{\mathbf{P}}_1 + \tilde{\mathbf{P}}_2)^{-1}\tilde{\mathbf{P}}_2\boldsymbol{\Delta}_{12}\right) \tag{3.1}$$

where $\tilde{\mathbf{Q}}_1$ is the quaternion, measured by camera head 1, that describes the attitude of the satellite with respect to celestial frame, $\mathbf{P}_i$ is the weighting matrix that expressed the anisotropic measurement noise of camera i and $\boldsymbol{\Delta}_{12}$ are the small differences in attitude of the two star cameras. On the other hand, for the second approach the uncertainty in the rotation about the boresight axis is omitted by merging the boresight axes of the two star cameras into a common reference frame (CRF). This idea was developed for the star camera data processing of the CHAMP mission [Mandea et al., 2010] and it was also tested for the GOCE star camera data [Stummer et al., 2011].

By comparing the power spectral density (PSD) of the angular rates derived from the two above-mentioned techniques, Bandikova and Flury [2014] found out that the two approaches gave almost identical results and provided an optimal attitude solution. The advantage of the strategy proposed by Romans [2003] is, however, that multiple star cameras can be more easily combined in contrast to the other one. An additional comparison was made between the first and the official processing method, which revealed the existence of incorrect implementation of the algorithms in the JPL processing routines. The mistake was attributed to the fact that the SCA anisotropic measurement noise was not taken into account correctly. Last but not least, Bandikova and Flury [2014] suggested that subsequent improvement can be obtained when the exact variance of the sensor noise is taken individually for each SCA head.

In the meantime, Klinger and Mayer-Gürr [2014] identified that accelerometer measurements can improve the attitude estimate by providing additional attitude information in terms of angular accelerations. Hence, a sensor fusion technique was proposed that combined both star camera and angular accelerometer data in a least squares adjustment. The combination of the two data types was achieved using variance component estimation. The input data for the sensor fusion included the star camera quaternions that describe the rotation from the satellite to the inertial frame and accelerometer angular accelerations in the x, y and z direction. The output was estimated quaternions and optionally angular rates and accelerations. Figure 3.1 shows the PSD of angular accelerations in the y-direction. The blue and red line represent the angular accelerations from accelerometer and from star camera data respectively, while the red one are accelerations estimated from the sensor fusion. It is clear that the proposed sensor fusion approach yields better angular acceleration estimates, for which the accelerometer observations contributed to a better estimation of the higher frequencies, while

the star camera data to the lower ones. In addition, the noise within the antenna offset correction was reduced notably, which improved the gravity field solutions.

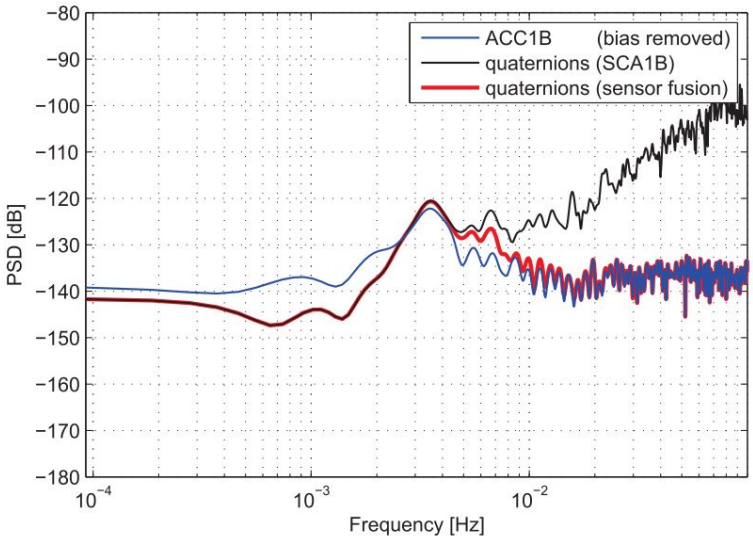

Figure 3.1: Power spectral density of angular accelerations in y-direction as computed by Klinger and Mayer-Gürr [2014]

Similarly to the previous approach, within JPL's V03 GRACE attitude processing strategy Harvey and Sakumura [2019] presented a Kalman filter setup that combined star camera data and angular accelerations measured by the on-board accelerometer of each satellite to produce a smooth attitude solution. Table 3.1 presents an overview of this Kalman filter setup. All the state space variables were provided at each epoch except for the camera quaternions relative to the spacecraft frame that were given once per day. Moreover, it should be noted that 10 Hz linear accelerations were averaged over 1 second intervals and, as the 1 Hz angular accelerations, they were re-interpolated from the accelerometer to the star camera epochs. The smoothed quaternions were also re-interpolated to GPS Time.

Table 3.1: Overview of the GRACE Kalman filter setup. Source: [Harvey & Sakumura, 2019]

State Space	**Primary Measurements**
Spacecraft quaternions relative to inertial space	1 Hz star camera quaternions (SCA1A)
Camera quaternion relative to spacecraft frame	1 Hz angular accelerations
Angular velocity	**Secondary Measurements**
Angular acceleration	10 Hz linear accelerations
Star camera and accelerometer error terms	
State Evolution	**Output**
Rigid body dynamics based on quaternions, angular velocities and angular acceleration	Smoothed quaternions at each epoch

The Kalman filter applied rigid body dynamics in attitude quaternions, iterated once, then recalculated Kalman filter partials at each iteration including a small random walk term that compensated for the lack of resolution in accelerometer measurements. The dynamic equations used, can be written as:

$$v(t+1) = v(t) + a(t) \tag{3.2}$$

$$Q_v(t) \approx \left(1, \frac{v_x}{2}, \frac{v_y}{2}, \frac{v_z}{2}\right) \tag{3.3}$$

$$Q_p(t+1) = Q_p(t)Q_v(t)Q_r(t) \tag{3.4}$$

where $v(t)$ is the average angular velocity over the interval t to $t+1$, $a(t)$ is the change in average angular velocity between consecutive 1-s intervals, Q_v represents $v(t)$ in quaternion form, $Q_p(t)$ represents the spacecraft

attitude quaternion at epoch t and $Q_r(t)$ is the additional random walk term. The star camera error model was also improved by incorporating point-by-point white noise, FoV dependent noise (approximated using a cubic spline) and alignment errors on each camera with respect to the science reference frame. As far as the accelerometer model is concerned, the accelerometer errors are modelled as: white noise, bias with random walk and low rate noise, approximated by cubic splines. Moreover, Harvey and Sakumura [2019] investigated aliasing effects on the accelerometer data and found out that the accelerometer measurements could possibly contain two cross-term error sources that would prompt aliasing between linear and angular accelerations. The first error source arise from capacity gradient uncertainties and voltage potential between chromium-coated proof mass and gold-coated electrodes which will lead to a difference between true and measured accelerations by a factor of 1%. The second error source originates from the uneven charge distribution on each electrode plate and geometry errors. This in turn, will place the center of the exerted electrode net acceleration at an offset from the charge-plate center.

All in all, the Level-1 V03 reprocessing for GRACE corrected any errors in the attitude products identified by Bandikova and Flury [2014] and Harvey [2016] and provided an improved spacecraft attitude reconstruction. Including accelerometer data and solving for an alignment of star camera 2 relative to camera 1 allowed the Kalman filter to fill small gaps in star camera data, reduce the number of gaps in the final attitude and the attitude jumps at camera outages. Although, using the V03 attitude products, resulted in minimal gravity field improvements during most of the GRACE mission, noticeable reductions were observed in zonal harmonic and high frequency error patterns during isolated months early and late in the mission. In fact, these months were characterised with higher noise environments.

3.2. GOCE

A significant amount of research on attitude reconstruction has also been performed by the scientific community for the GOCE mission. GOCE is a gravity field mission, operated from 2009 until 2013, with its main goal to measure the mean gravity field at high spatial resolution using an electrostatic gravity gradiometer (EGG). Same as for the GRACE and GRACE-FO satellites, accurate attitude reconstruction over the course of their mission played an important role for the recovery of precise Earth gravity field models.

Castini and Cesare [2008] were one of the first to perform a nominal angular rate reconstruction (ARR) for the GOCE mission in the context of the gradiometer in-orbit calibration procedure. Within this scheme, the inertial attitude was also determined simultaneously. The ARR combined star tracker and gradiometer data by means of iterative computation of a least-squares solution in the time domain. The inputs for the Kalman filter approach included the star tracker quaternions and the angular accelerations of the gradiometer, which are integrated to derive the angular rates. In the prediction step, the EGG angular rates were then used to rotate the attitude quaternions from the current epoch to the next. As a result, predicted attitude quaternions as well as star camera quaternions were available for future epochs. In the correction step of the iterative process, the correction for the angular rate estimates and the current attitude quaternion were computed from the difference between the two previously-mentioned sets of quaternions [Stummer et al., 2011].

Later on, Stummer et al. [2011] investigated an alternative method for determining the inertial angular rates of GOCE. Similarly to the method described above, Stummer et al. [2011] combined attitude information of the star sensors and the gradiometer at the level of angular rates based on their stochastic properties. Wiener filtering was used to combine the two sensors' data in the spectral domain. The spectral combination of the three angular rate components was done in the gradiometer reference frame (GRF), whose axes are determined with respect to the inertial reference frame. Figure 3.2 illustrates this new angular rate reconstruction method.

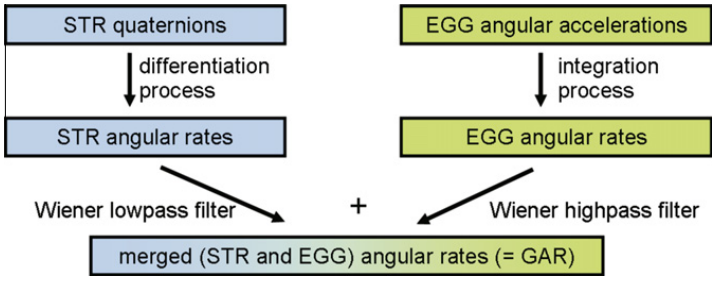

Figure 3.2: GOCE angular rates reconstruction based on Wiener filtering. Source: [Stummer et al., 2012]

The first step of this method was to obtain the star tracker quaternions that describe the rotation from the inertial to the GRF. Afterwards, the star tracker angular rates were calculated by differentiating the rotated quaternions. The next step was to determine the angular rates from the gradiometer, which was accomplished by numerically integrating the measured angular accelerations. Finally, the PSD of the noise of the angular rate components for the two instruments were weighted and the optimal combination between their angular rates was achieved. The weights h_k for the Wiener filter were calculated as

$$h(STR)_k = \frac{\sigma_k^2(EGG)}{\sigma_k^2(EGG) + \sigma_k^2(STR)} \tag{3.5}$$

$$h(EGG)_k = \frac{\sigma_k^2(STR)}{\sigma_k^2(EGG) + \sigma_k^2(STR)} \tag{3.6}$$

where the σ_k^2 are the variances of the gradiometer and the star tracker noise at frequency k. Consequently, for all frequencies the sum of the weights equals one, i.e. $h(STR)_k + h(EGG)_k = 1$. The angular rates are merged component-wise according to

$$F(\text{merge})_k = F(STR)_k \cdot h(STR)_k + F(EGG)_k \cdot h(EGG)_k \tag{3.7}$$

where F is the frequency domain representation of the STR, EGG or merged angular rate component at frequency k. Then, the combined angular rates are obtained by transforming the merged angular rates back to the time domain. Comparing the new angular rates with those of the previous approach, it was found that for frequencies lower than 5 mHz the Wiener filter method performs much better than the nominal ARR presented by Castini and Cesare [2008]. However, within the measurement bandwidth (MBW), i.e. from 5 to 100 mHz, no difference was observed between them.

In 2018, a full reprocessing of GOCE mission data was performed to improve the gravity gradients as well as to introduce an improved method for calibrating and combining attitude data from all three star cameras onboard the GOCE satellite. The combination method presented by Siemes et al. [2018] extended the approach by Romans [2003] by including constant offsets and extra parameters that modelled linearly small, temperature-dependent offsets in the star camera data. The comparison of the inter-boresight angles (IBA) that the star cameras observed in-flight with the pre-flight ones, revealed the existence of offsets and small changes about the mean for all three IBAs. These small variations were found to be correlated with star tracker CCD temperatures. The application of this calibration and combination procedure, improved the GOCE gravity gradients below 2 mHz.

The complete attitude reconstruction for GOCE was later described in great detail by Siemes [2018] and it was based on the above-mentioned angular rate reconstruction and star trackers calibration and combination methods. However, compared to the method proposed by Stummer et al. [2011], a slightly different approach was used by Siemes [2018] for obtaining the relative weights for the star cameras and gradiometer angular rates. Furthermore, a minor part was added to the algorithm that reduces the transient effects due to the filtering. As far as the proposed attitude reconstruction is concerned, its objective was to improve the attitude produced by the combined star cameras by incorporating the reconstructed angular rates. This was achieved by fitting the attitude quaternions derived from the latter to the combined star camera quaternions using a proper weighting scheme in the adjustment.

3.3. Research Gap

From the research done so far on the attitude reconstruction of gravity missions, there has been a significant contribution 1) to the understanding of how measurements of instruments, other than the main attitude sensors, relate to the satellite's attitude and 2) to the implementation of sensor fusion methods that manage to achieve a more accurate attitude determination on-ground than what could be achieved solely by the star cameras. Within the context of the last point, many authors illustrated that poor error modelling of the star cameras (e.g. in [Harvey, 2016] and [Siemes et al., 2018]) as well as of other instruments (e.g. in [Harvey & Sakumura, 2019]) was leading to a degraded attitude solution. Thus, more elaborate noise models for the various sensors were introduced and implemented by the scientific community, which lead to an improved attitude reconstruction. Another interesting point that can be made is the different choice of attitude reconstruction methods between GRACE and GOCE. For the case of the former the use of Kalman filtering was made and for the latter a generalized least-squares adjustment was used. Still, as stated by Stummer et al. [2011], in

the early stages of the GOCE mission a Kalman filtering approach was used for its attitude reconstruction, however, it was later proven that the use of a new angular rate reconstruction method together with a generalized least-squares adjustment granted a better attitude solution.

Currently, as mentioned by Landerer, Flechtner, et al. [2020], the GRACE-FO star cameras have shown to be operating nominally and by combining gyroscopic data, by means of Kalman filtering, the estimated white noise for the star cameras revealed to be two times lower than that of GRACE, however, no comprehensive analysis has been published yet on the star camera error and noise characteristics as well as of the fiber-optic gyroscopes for the GRACE-FO mission. On the other hand, as stated by Kornfeld et al. [2019], the accelerometer on the GRACE-FO D satellite does not perform as expected and no definite cause has been found yet. Previous research has shown, however, that a sensor fusion approach can provide an insight into the performance and behavior of the various instruments used in the process and by better modelling their respective noise an improved attitude solution can be achieved. In other words, by understanding the performance of the angular accelerations measured by that accelerometer, a clearer picture could be gained of the noise in the linear measurements. Needless to say, no analysis has been performed yet on the extend each GRACE-FO sensor contributes to the final attitude solution. Equally important, it has not yet been investigated which method, one being the Kalman filter and the other the generalised least-squares, accounts better for the instruments' noise and achieves a better attitude for GRACE-FO.

3.4. Research Objective & Questions

Taking the above as a basis, the goal of this MSc thesis is to analyse the noise characteristics of the GRACE-FO sensors that relate measurements to the satellite's attitude and develop a method that accounts for the instruments' noise and fuses the data giving an improved attitude solution. An accurate attitude reconstruction method can benefit the objectives of the GRACE-FO mission, by positively affecting the antenna offset correction and in turn the KBR measurements. A sensor fusion method can also be very valuable for understanding better the performance of the accelerometers on GRACE-FO as well as of the star cameras, the fiber-optic gyroscopes and the LRI steering mirrors. This in turn, can be beneficial for the design of future gravity missions such as the NGGM proposed by ESA, for which a redundant accelerometer design is considered. Given a proper estimate of the noise characteristics of the above instruments, the most favorable placement of the accelerometers can be suggested, so that in case one of them fails, the noise in the required centrifugal and Euler acceleration corrections are within the overall system performance requirements. The research objective of this MSc thesis is then defined as follows:

to develop a method for the combination, error and noise characterization of the measurements of the GRACE-FO star trackers, fiber-optic gyroscopes, accelerometers and laser ranging interferometer's steering mirrors by means of least-squares adjustment.

The research question linked to the research objective is the following:

to what extent can a new attitude sensor data fusion method improve the current attitude solution by incorporate accurately the noise and error characteristics of the GRACE-FO star trackers, fiber-optic gyroscopes, accelerometers and laser ranging interferometer's steering mirrors?

Below follows a list of questions and sub-questions that are derived from the main research question and can help to structure this work and achieve the research objective:

1. **What properties describe the noise and error characteristics of the GRACE-FO star cameras, fiber-optic gyroscopes, accelerometer and laser ranging interferometer's steering mirror measurements?**
    a) What methods are suited to analyse and determine the noise and error characteristics of each instrument?
    b) How does each instrument behave with respect to its specifications?
    c) How does the performance of same instruments compare between the two satellites?
    d) What time windows will be used for the analyses?
2. **What methods can be used to fuse the measurements of the star cameras, the fiber-optic gyroscopes, the accelerometer and the laser ranging interferometer's steering mirrors?**
    a) How can the instruments' noise and error characteristics be modeled best?

b) What functional model will be used to connect the measurements to the satellite attitude?

3. **To what extent can the newly-developed methods improve the already existing satellite attitude dataset for the GRACE-FO mission?**

   a) How does the solution from the newly-developed method compare to the one using a Kalman filter approach?

   b) How much does each sensor contribute to the quality of the final attitude solution based on the newly-developed method?

4. **To what extent can an improved attitude reconstruction method benefit the GRACE-FO mission?**

4

Processing Algorithms

This chapter is dedicated to the description of four main processing algorithms that were implemented during this thesis. Some of these are important building blocks for the instruments' error assessment and the attitude reconstruction process, while others will be used to evaluate the latter's performance. In Section 4.1 the steps to calculate the inter-satellite pointing angles are presented and in Section 4.2 the derivation procedure of the angular rates from each instrument is given. Next, Section 4.3 explains the process of calculating the star camera inter-boresight angles (IBA) and finally, in Section 4.4 the computation for the antenna offset correction is described.

4.1. Inter-satellite pointing angles

The precise knowledge of the inter-satellite pointing is fundamental for the GRACE-FO mission, so that the true distance between the CoMs of the two satellites can be measured, which is necessary for deriving gravity field models. In an ideal situation the KBR PhC of the antenna horn will be aligned with the line-of-sight between the satellites, resulting in the measurement of the real separation between them. However, due to attitude perturbations caused by external forces, such as the solar radiation pressure and the aerodynamic force, the inter-satellite pointing is affected [Bandikova, 2015]. Figure 4.1a and Figure 4.1b demonstrate the ideal and the real pointing of the two satellites.

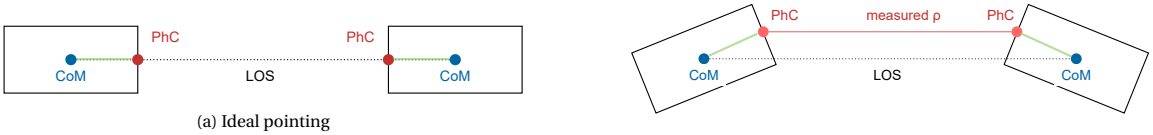

(a) Ideal pointing

(b) Real pointing

Figure 4.1: Representation of the ideal and the real inter-satellite pointing for GRACE-FO.

Geometrically, the inter-satellite pointing can be interpreted as the angular deviations of the CoM-to-PhC vector from the line-of-sight. Mathematically, it is expressed as a sequence of three angles, which can be derived from the rotation matrix $\mathbf{R}_{\mathrm{KF}\rightarrow\mathrm{LOSF}}$. This matrix describes the rotation that transforms a vector from the K-frame (KF) to the line-of-sight frame (LOSF). The x axis of the former coincides with the calibrated CoM-to-PhC vector, while for the latter with the imaginary line that connects the CoMs of the satellites (see Figure 4.2). For the full definition of these reference frames as well as the ones presented below, the reader is referred to Appendix A.2.

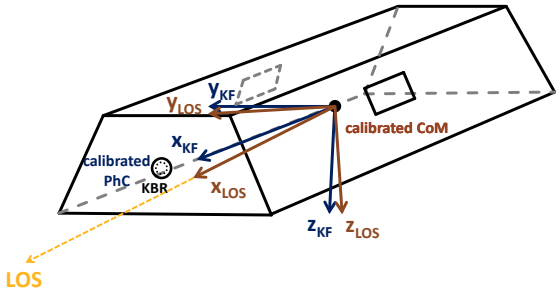

Figure 4.2: Illustration of the K-frame and the line-of-sight frame. Source: [Bandikova, 2015]

The previously-mentioned rotation sequence can then be written as [Bandikova, 2015]

$$\mathbf{R}_{\text{KF}\rightarrow\text{LOSF}} = \mathbf{R}_x(\theta_x)\mathbf{R}_y(\theta_y)\mathbf{R}_z(\theta_z) \tag{4.1}$$

where $\mathbf{R}_x(\theta_x)$ denotes a rotation around the x axis by an angle θ_x, which is called roll angle, $\mathbf{R}_y(\theta_y)$ denotes a rotation around the y axis by an angle θ_y, which is called pitch angle and $\mathbf{R}_z(\theta_z)$ denotes a rotation around the z axis by an angle θ_z, which is called yaw angle. Equation (4.1) can also be written as the multiplication of two rotation matrices, i.e.

$$\mathbf{R}_{\text{KF}\rightarrow\text{LOSF}} = \mathbf{R}_{\text{Inertial}\rightarrow\text{LOSF}} \cdot \mathbf{R}_{\text{KF}\rightarrow\text{Inertial}} \tag{4.2}$$

The first matrix that describes a rotation from the inertial frame to the LOSF can be determined using the following relations

$$\mathbf{R}_{\text{Inertial}\rightarrow\text{LOSF}} = \begin{bmatrix} (\mathbf{x}_{\text{LOSF}})^T \\ (\mathbf{y}_{\text{LOSF}})^T \\ (\mathbf{z}_{\text{LOSF}})^T \end{bmatrix} \quad \text{with} \quad \begin{aligned} \mathbf{x}_{\text{LOSF}} &= \frac{\mathbf{r}_{\text{other}} - \mathbf{r}}{|\mathbf{r}_{\text{other}} - \mathbf{r}|} \\ \mathbf{y}_{\text{LOSF}} &= \mathbf{x}_{\text{LOSF}} \times \frac{\mathbf{r}}{|\mathbf{r}|} \\ \mathbf{z}_{\text{LOSF}} &= \mathbf{x}_{\text{LOSF}} \times \mathbf{y}_{\text{LOSF}} \end{aligned} \tag{4.3}$$

where the vector $\mathbf{r}$ represents the position of one satellite in inertial Earth-centered frame and $\mathbf{r}_{\text{other}}$ the position of the other. The rotation matrix $\mathbf{R}_{\text{KF}\rightarrow\text{Inertial}}$ can be obtained from the measured quaternions of the star cameras. As already mentioned in Section 2.3.1, the cameras measure the quaternions that describe the rotation from inertial to the individual SCF, so firstly it is required to transform the latter to the satellite frame (SF). This is achieved with the QSA quaternions that describe the rotation from the SCF to SF. In equations form this reads

$$\mathbf{q}_{\text{Inertial}\rightarrow\text{SF}} = \mathbf{q}_{\text{Inertial}\rightarrow\text{SCF}} \cdot \mathbf{q}_{\text{SCF}\rightarrow\text{SF}} \tag{4.4}$$

Afterwards, by converting the above quaternions to their rotation matrix representation, the $\mathbf{R}_{\text{Inertial}\rightarrow\text{SF}}$ matrix is derived. The rotation matrix $\mathbf{R}_{\text{Inertial}\rightarrow\text{KF}}$ is then obtained with the following relations

$$\mathbf{R}_{\text{Inertial}\rightarrow\text{KF}} = \begin{bmatrix} (\mathbf{x}_{\text{KF}})^T \\ (\mathbf{y}_{\text{KF}})^T \\ (\mathbf{z}_{\text{KF}})^T \end{bmatrix} \quad \text{with} \quad \begin{aligned} \mathbf{x}_{\text{KF}} &= (\mathbf{R}_{\text{Inertial}\rightarrow\text{SF}})^T \frac{\mathbf{r}_{\text{pc}}}{|\mathbf{r}_{\text{pc}}|} \\ \mathbf{y}_{\text{KF}} &= \mathbf{z}_{\text{KF}} \times \mathbf{x}_{\text{KF}} \\ \mathbf{z}_{\text{KF}} &= \mathbf{x}_{\text{KF}} \times \mathbf{y}_{\text{SF}} \end{aligned} \tag{4.5}$$

where $\mathbf{r}_{\text{pc}}$ is the CoM-to-PhC vector in the SF and can be obtained from the VKB1B data product. The results of Equation (4.5) and Equation (4.3) are then substituted in Equation (4.2) and by solving for θ_x, θ_y and θ_z, the desired pointing angles can be acquired. For the case of the IMU or accelerometer data, their corresponding measured angular rates can be used in combination with initial values from the star cameras to compute the equivalent quaternions that describe the rotation from the inertial to the SF. However, due to error propagation in the integration process, this method is only accurate for a short time span.

4.2. Satellite angular rates

The calculation of the satellite's angular rates is a salient part for the attitude reconstruction process. As already mentioned in Section 2.3, each of the four instruments under consideration has a different measurement principle, however, they can all measure the same variations of the satellite's attitude which can be translated to angular rates. In this section, the derivations of the latter for the star cameras, the IMU and the accelerometers are presented.

4.2.1. Star Tracker Assembly

The star camera measurements provide the inertial attitude of the satellite in terms of quaternions. Similar to a rotation matrix, a quaternion represents a rotation of elements in three dimensional space. The GRACE-FO star camera quaternions express the rotation of the inertial into the individual SCF (i.e. $\mathbf{q}_{\text{Inertial}\rightarrow\text{SCF}}$). In general, a quaternion $\mathbf{q} \in \mathbb{H}$, can be represented as a four dimensional vector [Teunissen & Montenbruck, 2017]

$$\mathbf{q}(\theta, \mathbf{n}) = \begin{bmatrix} \cos(\frac{\theta}{2}) & \mathbf{n} \cdot \sin(\frac{\theta}{2}) \end{bmatrix}^T \tag{4.6}$$

where θ is the angle of rotation and $\mathbf{n}$ is a unit vector that represents the axis of rotation. One way to relate quaternion rates to angular rates is with the following relation [Groves, 2008]

$$\dot{\mathbf{q}}_{A\to B} = \mathbf{q}_{A\to B}\mathbf{W}^{B}_{A,B} \tag{4.7}$$

where the quaternion $\mathbf{q}_{A\to B}$ represents the rotation from reference frame A to reference frame B and $\mathbf{W}^{B}_{A,B}$ is a vector that contains the angular rates

$$\mathbf{W}^{B}_{A,B} = \begin{bmatrix} 0 & \omega^{B}_{A,B,x}/2 & \omega^{B}_{A,B,y}/2 & \omega^{B}_{A,B,z}/2 \end{bmatrix}^{T} \tag{4.8}$$

where $\boldsymbol{\omega}^{B}_{A,B}$ is the angular rate vector describing the rate of rotation of the B-frame axes with respect to a stationary A-frame axes, resolved about the B-frame axes.

The star camera quaternion measurements are given as a time series with values $\mathbf{q} = [\mathbf{q}_1 .... \mathbf{q}_N]$ at epochs $\mathbf{t} = [t_1 .... t_N]$, with $\mathbf{q}_N$ being a four dimensional vector as in Equation (4.6). The derivative $\dot{\mathbf{q}}_{A\to B}$ can be numerically calculated by first interpolating $\mathbf{q}$ to the epochs $\mathbf{t} + \Delta t$ and $\mathbf{t} - \Delta t$ using cubic spline interpolation and with Δt being relatively small compared to the time difference $t_{n+1} - t_n$. In this work, a value of 1 millisecond is used for Δt. Then, the first time derivative of $\mathbf{q}$ can be calculated with the symmetric difference quotient, which is written in equation form as

$$\dot{\mathbf{q}} = \frac{\mathbf{q}(\mathbf{t} + \Delta t) - \mathbf{q}(\mathbf{t} - \Delta t)}{2\Delta t} \tag{4.9}$$

By first obtaining the quaternions $\mathbf{q}_{\text{Inertial}\to\text{SF}}$ from Equation (4.4), then substituting the results of Equation (4.9) in Equation (4.7) and rearranging with respect to $\mathbf{W}^{B}_{A,B}$, the corresponding satellite star camera angular rates can be derived.

4.2.2. Fiber optic gyroscopes

The inertial measurement unit provides angle measurements with respect to each individual gyroscope axes. The latter are in a tetrahedral configuration, which means that there is a redundancy in the design. Table 4.1 presents the directions of these axes in the IMU frame and Table 4.2 can be used to transform them to the SF.

Table 4.1: Directions of IMU gyro axes in IMU frame. Source: [Wen et al., 2019]

Satellite	Component	Gyro 1	Gyro 2	Gyro 3	Gyro 4
GRACE-FO C	x	0.942826211	-0.472597539	-0.470092696	0.000592072
	y	0.001810853	0.815825089	-0.817231401	-0.000382796
	z	0.33327985	0.333288147	0.333385204	-0.999999751
GRACE-FO D	x	0.942687237	-0.471344745	-0.471100307	0.000753399
	y	0.000111944	0.816437037	-0.816914065	0.000461058
	z	0.33367763	0.333563632	0.332740005	-0.99999961

Table 4.2: Transformation matrices from IMU Frame to Satellite Frame. Source: [Wen et al., 2019]

Satellite	Transformation Matrix		
GRACE-FO C	-0.501252164183920	0.865301254687325	-0.000080854668175
	0.865300283426991	0.501251737450002	0.001454374272271
	0.001299000425484	0.000659044684221	-0.999998939128437
GRACE-FO D	-0.501005885615109	0.865443870184570	0.000100692470726
	0.865443802410115	0.501005791604386	0.000470795904316
	0.000356999918493	0.000323015193725	-0.999999884106115

The derivation of satellite angular rates from the IMU measurements, can then be achieved by utilizing the above information in conjunction with the measurement equations of a redundant IMU [Jafari, 2015]. Specifically, assuming that such an IMU encloses n gyroscopes, the measurement equations of the system

can be expressed with the following relation

$$\begin{bmatrix} m_{g1} \\ m_{g2} \\ \vdots \\ m_{gi} \end{bmatrix} = \begin{bmatrix} S_x^1 & S_y^1 & S_z^1 \\ S_x^2 & S_y^2 & S_z^2 \\ \vdots & \vdots & \vdots \\ S_x^i & S_y^i & S_z^i \end{bmatrix} \begin{bmatrix} \omega_x \\ \omega_y \\ \omega_z \end{bmatrix} \tag{4.10}$$

where m_{gi} is the angular rate measured by the i^{th} gyroscope, $\omega_{x,y,z}$ are the satellite angular rates and $\mathbf{s}^i = [S_x^i \;\; S_y^i \;\; S_z^i]$ describes the orientation of the i^{th} gyro axis in the SF and is determined using Table 4.1 together with Table 4.2. The above equation can also be written in vector form as

$$\mathbf{m} = \mathbf{H}\boldsymbol{\omega} \tag{4.11}$$

In this case, $\mathbf{m}$ is called the measurement vector, $\mathbf{H}$ is the sensor geometry matrix or design matrix that describes the configuration of the redundant IMU system and $\boldsymbol{\omega}$ are the angular rates in the satellite body frame. For GRACE-FO, the IMU data product provides only measurements from three gyroscopes, so n=3, and since these represent angles, they need to be differentiated first in order to properly define the measurement vector of the form

$$\mathbf{m} = \begin{bmatrix} \omega_{g1} & \omega_{g2} & \omega_{g3} \end{bmatrix}^T \tag{4.12}$$

where ω_{gi} is the angular rate measured by the i^{th} gyro of the IMU. The first time derivative is calculated in the same way as for the quaternions (see Equation (4.9)). Finally, the angular rates in the satellite frame can be calculated by rearranging Equation (4.11) and solving for $\boldsymbol{\omega}$.

4.2.3. SuperSTAR Accelerometer

The derivation of accelerometer angular rates is simply the integration of the measured angular accelerations [Siemes, 2018]. This is achieved by firstly upsampling the latter using spline interpolation and then by applying the trapezoidal integration scheme on the upsampled accelerations. Given the time series of the measured accelerations around each axis of the accelerometer, with values $\boldsymbol{a}_i = [a_{i,1}....a_{i,N}]$ at epochs $\mathbf{t}_i = [t_{i,1}....t_{i,N}]$ for $i = x, y, z$, the corresponding upsampled values and epochs are denoted by $\mathbf{t}_i^{\text{up}}$ and $\boldsymbol{a}_i^{\text{up}}$. The increase in sampling rate is specified with the integer variable K, such that K-1 new epochs are inserted between $t_{i,n}$ and $t_{i,n+1}$. In this work, a value of K=10 is used. The angular rates can then be computed using the trapezoidal integration, shown by the following equation

$$\omega_{i,n}^{\text{up}} = \omega_{i,n-1}^{\text{up}} + \frac{(a_{i,n}^{\text{up}} + a_{i,n-1}^{\text{up}})(t_{i,n}^{\text{up}} - t_{i,n-1}^{\text{up}})}{2} \tag{4.13}$$

where $\omega_{i,n}^{\text{up}}$ is the angular rate around the i^{th} axis of the accelerometer at epoch n. Important to note, prior to the integration, the mean of the resulting upsampled time series $\mathbf{a}_i^{\text{up}}$ is subtracted in order to minimize the accumulation of rounding errors. Next, the integrated upsampled time series $\boldsymbol{\omega}_i^{\text{up}}$ is decimated to the original epochs to obtain $\boldsymbol{\omega}_i$. Last but not least, because the acceleration measurements are provided with respect to the accelerometer frame, $\boldsymbol{\omega}_i$ should be rotated to the satellite reference frame. This is accomplished by first applying a -90° rotation around the x axis and then a +90° rotation around the z axis of the accelerometer.

4.3. Inter-boresight angles

An important part for assessing the performance of the star cameras is evaluating the knowledge of their orientation with respect to each other. This can be achieved by the analysis of the differences between the IBAs determined by a preliminary knowledge of the cameras' orientation in the SF and by in-flight measurements. As the name suggests, the IBA refers to the angle of the boresight vectors between a pair of star cameras. Each camera has it own frame (denoted as SCF_i, for $i = 1,2,3$), whose origin is at the intersection of the boresight axis with the mounting plane of that camera. The positive z_{SCA_i} axis of SCF_i is extended out along the boresight axis and the positive x_{SCA_i} and y_{SCA_i} axes are found on the optical plane. In general, the accuracy of the cross-boresight axes (i.e. x_{SCA_i} and y_{SCA_i}) is higher than the boresight axis and controls the accuracy of the latter. Thus, it is convenient to analyse the IBAs to examine the relative performance of the star cameras. In fact, comparing the IBAs that are determined by a preliminary knowledge of the cameras' orientation in the SF

with the ones observed in-flight later on in the mission, could unveil possible systematic errors in their relative orientation. Such analysis, has been performed for the GOCE [Siemes et al., 2019] and the Swarm mission [Herceg et al., 2017], from which the IBAs were found to exhibit temperature-dependent variations.

Based on the calibration maneuvers that were performed on the GRACE-FO satellites in the beginning of the mission, the orientation of each star camera with respect to the SF was determined. In Equations (4.14) to (4.19) the quaternions that describe the rotation from the individual star camera to the satellite frame are given. These values are stored in the QSA1B data products released on the 22$^{\text{nd}}$ of May in 2018.

$$\mathbf{q}^{C}_{\text{SCF}_1\rightarrow\text{SF}} = \begin{bmatrix} -0.1846523033914243 \\ 0.687786333034212 \\ 0.676514247097443 \\ 0.18756854858364 \end{bmatrix} \tag{4.14}$$

$$\mathbf{q}^{D}_{\text{SCF}_1\rightarrow\text{SF}} = \begin{bmatrix} -0.1789388979356683 \\ 0.682734893544669 \\ 0.68280707751296 \\ 0.188754949181018 \end{bmatrix} \tag{4.15}$$

$$\mathbf{q}^{C}_{\text{SCF}_2\rightarrow\text{SF}} = \begin{bmatrix} 0.2482955018618801 \\ -0.0400731149707713 \\ 0.85161599836015 \\ 0.459884420858917 \end{bmatrix} \tag{4.16}$$

$$\mathbf{q}^{D}_{\text{SCF}_2\rightarrow\text{SF}} = \begin{bmatrix} 0.2364914939710544 \\ -0.0535740306800429 \\ 0.851794739502496 \\ 0.464378421410715 \end{bmatrix} \tag{4.17}$$

$$\mathbf{q}^{C}_{\text{SCF}_3\rightarrow\text{SF}} = \begin{bmatrix} -0.4627545612843981 \\ 0.85311986815175 \\ -0.0427367676938312 \\ -0.23710393346022 \end{bmatrix} \tag{4.18}$$

$$\mathbf{q}^{D}_{\text{SCF}_3\rightarrow\text{SF}} = \begin{bmatrix} -0.4504277250139701 \\ 0.8590253079524141 \\ -0.0480909983022378 \\ -0.238490336739864 \end{bmatrix} \tag{4.19}$$

The preliminary IBAs can be computed using the above quaternions together with the following steps. The quaternion representation of the boresight vector of the i^{th} star camera can be expressed in SCF_i as

$$\mathbf{b}_i^{\text{SCF}_i} = \begin{bmatrix} 0 & 0 & 0 & 1 \end{bmatrix}^T \tag{4.20}$$

This quaternion can be transformed to the SF using the below equation [Groves, 2008]

$$\mathbf{b}_i^{\text{SCF}} = \mathbf{q}^{*}_{\text{SCF}_i\rightarrow\text{SF}} \cdot \mathbf{b}_i^{\text{SCF}_i} \cdot \mathbf{q}_{\text{SCF}_i\rightarrow\text{SF}} = \begin{bmatrix} 0 & b_{i,x}^{\text{SCF}} & b_{i,y}^{\text{SCF}} & b_{i,z}^{\text{SCF}} \end{bmatrix}^T \tag{4.21}$$

where the superscript asterisk denotes the conjugate of the quaternion, i.e. $\mathrm{q}^{*}_{A\rightarrow B} = \mathrm{q}_{B\rightarrow A}$. Then by computing the dot product of the resulting boresight vectors in the SF, the preliminary IBA values can be determined

$$\text{IBA}_{\text{pre},ij} = \arccos(\mathbf{b}_i^{\text{SF}} \cdot \mathbf{b}_j^{\text{SF}}) \quad \text{for} \quad i,j = 1,2,3 \quad \text{and} \quad i \neq j \tag{4.22}$$

As far as the calculation of in-flight IBAs is concerned, the orientation of the boresight vector ($\mathbf{Z}_{\text{SCF}_i}$) of each star camera with respect to inertial space is obtained from the measured quaternions, which describe the rotation from the inertial to the individual SCF. Specifically, they are given from the rotation matrix representation of these quaternions:

$$\mathbf{q}_{\text{Inertial}\rightarrow\text{SCF}_i} \Longleftrightarrow \mathbf{R}_{\text{Inertial}\rightarrow\text{SCF}_i} = \begin{bmatrix} (\mathbf{x}_{\text{SCF}_i})^T \\ (\mathbf{y}_{\text{SCF}_i})^T \\ (\mathbf{z}_{\text{SCF}_i})^T \end{bmatrix} \tag{4.23}$$

Similarly as with the preliminary ones, the in-flight IBAs are calculated using the following equation

$$\text{IBA}_{\text{inflight},ij} = \arccos(\mathbf{z}_{\text{SCF}_i} \cdot \mathbf{z}_{\text{SCF}_j}) \quad \text{for} \quad i,j = 1,2,3 \quad \text{and} \quad i \neq j \tag{4.24}$$

4.4. Antenna offset correction

The K-band ranging system of GRACE-FO measures the range between the two KBR antenna PhCs of the two satellites. For the determination of the gravity field, however, the inter-satellite range observations, must be related to their CoMs. This is achieved by applying the AOC, which corrects not only for the offset of the PhC from the CoM, but also for any imperfect pointing between the satellites [Bandikova, 2015]. Specifically, the AOC for range, depicted in Figure 1.1, is defined as the projection of the CoM-to-PhC vector of both satellites on the line-of-sight, i.e. $AOC_r = AOC_C + AOC_D$. The AOC for range, range rate and range acceleration is directly related to the inter-satellite pointing and can be computed using the following equations:

$$AOC_r = \sum_{i=C,D} |\mathbf{r}_{\text{pc},i}| \cdot \cos(\theta_i) \cdot \sin(\phi_i) \tag{4.25}$$

$$AOC_{\dot{r}} = \sum_{i=C,D} -|\mathbf{r}_{\mathrm{pc},i}|\left(\dot{\theta}_i \sin(\theta_i)\cos(\phi_i) + \dot{\phi}_i \cos(\theta_i)\sin(\phi_i)\right) \tag{4.26}$$

$$\begin{aligned} AOC_{\ddot{r}} = \sum_{i=C,D} -|\mathbf{r}_{\mathrm{pc},i}|\big(&\dot{\theta}_i{}^2 \cos(\theta_i)\cos(\phi_i) + \ddot{\theta}_i \sin(\theta_i)\cos(\phi_i) - 2\dot{\theta}_i\dot{\phi}_i \sin(\theta_i)\sin(\phi_i) \\ &+\ddot{\phi}_i \cos(\theta_i)\sin(\phi_i) + \dot{\phi}_i{}^2 \cos(\theta_i)\cos(\phi_i)\big) \end{aligned} \tag{4.27}$$

where $|\mathbf{r}_{\mathrm{pc},i}|$ is the length of the CoM-to-PhC vector and θ and ϕ are the pitch and yaw angles respectively. The position of the vector in the SF was estimated during the calibration maneuvers at the beginning of the mission and can be retrieved from the VKB1B data product. Table 4.3 provides this vector for both GRACE-FO C and D, in terms of its magnitude and direction cosines.

Table 4.3: Vector position for the KBR antenna phase center, defined in the satellite frame.

	GRACE-C	**GRACE-D**
Magnitude	1.4444	1.44446
x-axis direction cosine	1	1
y-axis direction cosine	-0.00012	4e-05
z-axis direction cosine	0.00031	0.00016

It is clear that in case systematic errors exists in either the pointing angles or the PhC vector, the accuracy of the KBR inter-satellite ranging observations will directly be affected and in turn the accuracy of the recovered gravity field model [Bandikova, 2015].

5
Sensor Data fusion

In this chapter the various methods for combining data from the star cameras, the IMU and the steering mirrors will be discussed. First, in Section 5.1 the method that is used to optimally combine quaternions of star camera and steering mirror measurements is presented. Next, in Section 5.2 the different calibration procedures for the star camera, the IMU and the steering mirror data are given. In Section 5.3 and Section 5.4 follows with the description of the proposed angular rate and attitude reconstruction methods and finally in Section 5.2.4 an approach for correcting the star camera FoV errors is presented.

5.1. Optimal combination of quaternions

In Section 5.1.1 the optimal combination of star camera quaternions is presented and in Section 5.1.2 this approach is extended to include the steering mirror quaternions as well.

5.1.1. Star cameras

The proposed strategy to combine the GRACE-FO star camera quaternions is based on the approach presented by Siemes et al. [2019], which extends the method by Romans [2003] to include additional terms in the noise quaternion that can account for any offsets observed between the preliminary and the in-flight IBAs. In general, the advantage of using the method by Romans [2003] is that the anisotropic accuracies of the cross-boresight and roll axes of the star cameras can be taken into account and an optimal quaternion can be obtained using a least-squares adjustment. With the addition of parameters that model IBA offsets, the relative calibration of the star camera quaternions is possible. This has not been discussed explicitly for the GRACE-FO mission and since it has contributed to an improvement in the GOCE gravity gradients, it is expected to improve the reconstructed attitude of GRACE-FO as well.

The measured quaternion $\mathbf{q}^{\text{meas}}_{\text{Inertial}\rightarrow SCF_i}$ of the i^{th} star camera, that describes the rotation from the inertial to the i^{th} SCF, is connected to the true quaternion by

$$\mathbf{q}^{\text{meas}}_{\text{Inertial}\rightarrow SCF_i} = \mathbf{q}^{\text{true}}_{\text{Inertial}\rightarrow SCF_i}\,\mathbf{q}^{\text{noise}}_i \tag{5.1}$$

where $\mathbf{q}^{\text{noise}}_i$ is the noise quaternion of the i^{th} star camera that reflects a small rotation. In contrast to Bandikova and Flury [2014] and Romans [2003], it includes now the term $\mathbf{b}_i$ that models the offsets in the IBAs. In equation form it is defined as

$$\mathbf{q}^{\text{noise}}_i = \begin{bmatrix} 1 \\ \frac{1}{2}(\mathbf{e}_i + \mathbf{b}_i) \end{bmatrix} \tag{5.2}$$

where $\mathbf{e}_i$ is a vector that contains three small rotation angles in the SCF and $\mathbf{b}_i$ contains small, constant angles. The measured quaternions of Equation (5.1) can be rotated to a common frame using the QSA quaternions that describe the rotation from the individual camera to the SF. In equation form

$$\mathbf{q}^{\text{meas}}_{i,\text{Inertial}\rightarrow SF} = \mathbf{q}^{\text{meas}}_{\text{Inertial}\rightarrow SCF_i}\,\mathbf{q}_{SCF_i\rightarrow SF} \tag{5.3}$$

Theoretically, at any given moment each star camera measures the same attitude quaternions that describe the rotation from the inertial to the SF, however, due to measurements noise and systematic errors, small offsets exist between them. According to Romans [2003], the relative error between the i^{th} and the j^{th} star camera can be calculated with

$$\left(\mathbf{q}^{\text{meas}}_{i,\text{Inertial}\rightarrow SF}\right)^{-1}\left(\mathbf{q}^{\text{meas}}_{j,\text{Inertial}\rightarrow SF}\right) = \begin{bmatrix} 1 \\ \frac{1}{2}\mathbf{d}_{ij} \end{bmatrix} \tag{5.4}$$

The offset $\mathbf{d}_{ij}$ is defined for GRACE-FO as

$$\mathbf{d}_{ij} = \tilde{\mathbf{e}}_j + \tilde{\mathbf{b}}_j - \tilde{\mathbf{e}}_i - \tilde{\mathbf{b}}_i \tag{5.5}$$

where the tilde represents rotated vectors from the SCF to the common reference frame. For example, $\tilde{\mathbf{e}}_i = \mathbf{R}_{SCF_i \to SF}\mathbf{e}_i$, where $\mathbf{R}_{SCF_i \to SF}$ is the rotation matrix representation of the QSA quaternions. For conciseness, the variable $\boldsymbol{m}_{ij}$ is introduced, defined as

$$\mathbf{m}_{ij} = \tilde{\mathbf{b}}_j - \tilde{\mathbf{b}}_i - \mathbf{d}_{ij} \tag{5.6}$$

such that

$$\tilde{\mathbf{e}}_i = \tilde{\mathbf{e}}_j + \mathbf{m}_{ij} \tag{5.7}$$

As described by Romans [2003] the optimal solution can be found by minimizing the weighted residuals sum of squares of the elements of the noise quaternion, i.e.

$$S = \sum_{i=1}^{I} \mathbf{e}_i^T \mathbf{P}_i \mathbf{e}_i \tag{5.8}$$

where $I = 3$ since there are three star cameras on-board each GRACE-FO satellite and $\mathbf{P}_i$ is a 3×3 weight matrix defined in the star camera reference frame that specifies the accuracies of the boresight or roll (p_r) and cross-boresight (p_{cb}) axes

$$\mathbf{P}_i = \begin{bmatrix} p_{cb} & 0 & 0 \\ 0 & p_{cb} & 0 \\ 0 & 0 & p_r \end{bmatrix} \tag{5.9}$$

The latter can also be defined in the SF using the transformation

$$\tilde{\mathbf{P}}_i = \mathbf{R}_{SCF_i \to SF} \mathbf{P}_i \mathbf{R}_{SCF_i \to SF}^T \tag{5.10}$$

Assuming that the cross-boresight axes are 10 times more accurate than the boresight one, the corresponding values are chosen: $p_{cb} = 10^2$ and $p_r = 1$. Rotating all variables of Equation (5.8) to the SF and substituting Equation (5.7), the weighted residual sum of squares S can then be reformulated in terms of only one vector $\tilde{\mathbf{e}}$:

$$\begin{aligned} S &= \sum_{i=1}^{I} \tilde{\mathbf{e}}_i^T \tilde{\mathbf{P}}_i \tilde{\mathbf{e}}_i \\ &= \tilde{\mathbf{e}}_1^T \tilde{\mathbf{P}}_1 \tilde{\mathbf{e}}_1 \; + \; \sum_{i=2}^{I} \tilde{\mathbf{e}}_i^T \tilde{\mathbf{P}}_i \tilde{\mathbf{e}}_i \\ &= \tilde{\mathbf{e}}_1^T \tilde{\mathbf{P}}_1 \tilde{\mathbf{e}}_1 \; + \; \sum_{i=2}^{I} (\tilde{\mathbf{e}}_1 + \mathbf{m}_{i1})^T \tilde{\mathbf{P}}_i (\tilde{\mathbf{e}}_1 + \mathbf{m}_{i1}) \end{aligned} \tag{5.11}$$

As pointed out by Siemes et al. [2018], the residual sum of squares can be split into three components ($S_n = S_{ne} + S_{nc} + S_{nec}$) that depend either on the epoch-wise parameters $\tilde{\mathbf{e}}_1$ or on the constant parameters $\tilde{\mathbf{b}}_i$ or on both of them. Introducing the index n that indicates the epoch, the following components are defined

$$S_{ne} = \sum_{i=1}^{I} \tilde{\mathbf{e}}_{n1}^T \tilde{\mathbf{P}}_i \tilde{\mathbf{e}}_{n1} \tag{5.12}$$

that depends exclusively on the epoch-wise parameters, then

$$S_{nc} = \sum_{i=2}^{I} \mathbf{m}_{ni1}^T \tilde{\mathbf{P}}_i \mathbf{m}_{ni1} \tag{5.13}$$

depends only on the constant parameters and lastly

$$S_{nec} = 2 \sum_{i=2}^{I} \tilde{\mathbf{e}}_{n1}^T \tilde{\mathbf{P}}_i \mathbf{m}_{ni1} \tag{5.14}$$

depends on a cross-product of both. The minimisation of the weighted residual sum of squares $S = \sum_n S_n$ is equal to solving a generalised least squares adjustment with the observation equations for epoch n having the form

$$\mathbf{y}_n + \mathbf{e}_n = \mathbf{X}_e \boldsymbol{\beta}_{ne} + \mathbf{X}_{nc} \boldsymbol{\beta}_c \tag{5.15}$$

where the observation and residual vector (containing star camera attitude residuals expressed in the common reference frame) are defined respectively as

$$\boldsymbol{y}_n = \begin{bmatrix} \mathbf{0} & -\mathbf{d}_{n12} & -\mathbf{d}_{n13} \end{bmatrix}^T \tag{5.16}$$

$$\boldsymbol{e}_n = \begin{bmatrix} \tilde{\mathbf{e}}_{1n} & \tilde{\mathbf{e}}_{2n} & \tilde{\mathbf{e}}_{3n} \end{bmatrix}^T \tag{5.17}$$

where $\mathbf{0}$ indicates a vector of dimension 3×1. The parameter vectors are then written as

$$\boldsymbol{\beta}_{ne} = \tilde{\mathbf{e}}_{n1} \tag{5.18}$$

$$\boldsymbol{\beta}_c = \begin{bmatrix} \tilde{\mathbf{b}}_1 & \tilde{\mathbf{b}}_2 & \tilde{\mathbf{b}}_3 \end{bmatrix}^T \tag{5.19}$$

and the design matrices follow as

$$\mathbf{X}_e = \begin{bmatrix} \mathbf{I} \\ \mathbf{I} \\ \mathbf{I} \end{bmatrix} \tag{5.20}$$

$$\mathbf{X}_{nc} = \begin{bmatrix} \mathbf{0} & \mathbf{0} & \mathbf{0} \\ \mathbf{I} & -\mathbf{I} & \mathbf{0} \\ \mathbf{I} & \mathbf{0} & -\mathbf{I} \end{bmatrix} \tag{5.21}$$

where $\mathbf{I}$ indicates an identity matrix of dimension 3×3 and $\mathbf{0}$ a similar matrix but containing only zeros. The weight matrix for epoch n is equal to

$$\mathbf{P} = \begin{bmatrix} \tilde{\mathbf{P}}_1 & \mathbf{0} & \mathbf{0} \\ \mathbf{0} & \tilde{\mathbf{P}}_2 & \mathbf{0} \\ \mathbf{0} & \mathbf{0} & \tilde{\mathbf{P}}_3 \end{bmatrix} \tag{5.22}$$

Using the above equations each of the summands can be written as

$$S_{ne} = (\mathbf{X}_e\boldsymbol{\beta}_{ne})^T\mathbf{P}\mathbf{X}_e\boldsymbol{\beta}_{ne} \tag{5.23}$$

$$S_{nc} = (\mathbf{X}_{nc}\boldsymbol{\beta}_c - \mathbf{y}_n)^T\mathbf{P}(\mathbf{X}_{nc}\boldsymbol{\beta}_c - \mathbf{y}_n) \tag{5.24}$$

$$S_{nec} = 2(\mathbf{X}_e\boldsymbol{\beta}_{ne})^T\mathbf{P}(\mathbf{X}_{nc}\boldsymbol{\beta}_c - \mathbf{y}_n) \tag{5.25}$$

Due to the inclusion of the $\boldsymbol{\beta}_c$ parameters in the model, a more efficient technique should be used for the generalised least-squares adjustment compared to Romans [2003]. This involves the usage of the partitioned model [Teunissen, 2003], where the epoch-wise parameters are first eliminated from the observation equations and the constant parameters are solved for. The solution to the constant parameters is calculated with

$$\boldsymbol{\beta}_c = \Big(\sum_n \overline{\mathbf{X}}_{nc}^T\mathbf{P}\overline{\mathbf{X}}_{nc}\Big)^+\Big(\sum_n \overline{\mathbf{X}}_{nc}^T\mathbf{P}\mathbf{y}_n\Big) \tag{5.26}$$

where the plus sign indicates the Moore-Penrose inverse and the matrix $\overline{\mathbf{X}}_{nc}$ is defined as

$$\overline{\mathbf{X}}_{nc} = (\mathbf{I} - \mathbf{X}_e(\mathbf{X}_e^T\mathbf{P}\mathbf{X}_e)^{-1}\mathbf{X}_e^T\mathbf{P})\mathbf{X}_{nc} \tag{5.27}$$

The epoch-wise parameters can then be calculated with

$$\boldsymbol{\beta}_{ne} = (\mathbf{X}_e^T\mathbf{P}\mathbf{X}_e)^{-1}\mathbf{X}_e^T\mathbf{P}(\mathbf{y}_n - \mathbf{X}_{nc}\boldsymbol{\beta}_c) \tag{5.28}$$

After determining the parameters $\boldsymbol{\beta}_c$ and $\boldsymbol{\beta}_{ne}$, both of them are inserted into eq. (5.2) to calculate the noise quaternion, which is later inserted in Equation (5.1) to determine the generalised least-squares estimate for the true quaternion.

5.1.2. Star cameras and steering mirrors

Within this work, one of the proposed methods to incorporate steering mirror measurements to the attitude reconstruction process is by following and extending the procedure that was described in the previous section. The only difference is that now instead of 3 (star camera 1,2,3) there are 4 instruments (star camera 1,2,3 + steering mirrors) that can measure the same attitude quaternions that describe the rotation from the inertial to the SF.

The first step of this approach is to compute quaternions from the steering mirror pitch and yaw measured angles. In Section 4.1, the relation between pointing angles and quaternions was described, from which the following relation can be written

$$\begin{aligned}\mathbf{R}_{\text{SF}\rightarrow\text{Inertial}} &= \left(\mathbf{R}_{\text{Inertial}\rightarrow\text{LOSF}}\right)^T \cdot \mathbf{R}_{\text{SF}\rightarrow\text{LOSF}} \\ &= \mathbf{R}_{\text{LOSF}\rightarrow\text{Inertial}} \cdot \mathbf{R}_{\text{SF}\rightarrow\text{LOSF}} \\ &= \mathbf{R}_{\text{LOSF}\rightarrow\text{Inertial}} \cdot \mathbf{R}_x(\theta_x)\mathbf{R}_y(\theta_y)\mathbf{R}_z(\theta_z)\end{aligned} \tag{5.29}$$

At this point, it is clear that the above equation cannot be computed for the steering mirrors due to the absence of roll angles. There are two ways, however, to overcome this limitation. The first one is to utilize roll information from another instrument, such as the star cameras. For the second approach, at the likelihood of contaminating the resulting quaternions with star camera noise, the $R_x(\theta_x)$ matrix is simply disregarded from Equation (5.29). This is possible considering that the pointing angles are very small, thus the elementary rotation matrices commute and can act independent of each other [Muller, 2013]. Consequently, this means that the resulting matrix $\mathbf{R}_{\text{SF}\rightarrow\text{Inertial}}$ would be able to accurately describe only the rotations around the y and z axes of the satellite. The error that is introduced with the missing information is expected to be at a magnitude close to the noise of the steering mirrors.

The next step of this combination is to define the weight matrix of the steering mirror quaternions. This represents the variance of the noise in the corresponding components of the quaternions and can be expressed as

$$\tilde{\mathbf{P}}_4 = \begin{bmatrix} p_x & 0 & 0 \\ 0 & p_y & 0 \\ 0 & 0 & p_z \end{bmatrix} \tag{5.30}$$

where the subscript 4 denotes that the steering mirrors are the fourth instrument in the quaternion combination. As it will be shown in Section 7.1.3, the corresponding measured pitch and yaw angles exhibit a ten times ($\kappa = 10$) higher accuracy than the ones computed with star camera data and show a one-to-one relation with the y and z components of the derived quaternions. At the same time, the x component will not provide any additional meaningful information, because the steering mirrors do not capture the roll variations of the satellite. Consequently, it is logical to assume the following values for the variances of the noise in the steering mirror quaternions: $p_y = p_z = \kappa^2 \cdot p_{cb} = 10^2 \cdot 10^2 = 10^4$ and $p_x = 0$.

Afterwards, the observation, residual and parameter vectors and the design matrices of the generalised least squares adjustment, presented in Section 5.1.1, can be extended and defined respectively as

$$\boldsymbol{y}_n = \begin{bmatrix} \mathbf{0} & -\mathbf{d}_{n12} & -\mathbf{d}_{n13} & -\mathbf{d}_{n14} \end{bmatrix}^T \tag{5.31}$$

$$\boldsymbol{e}_n = \begin{bmatrix} \tilde{\mathbf{e}}_{1n} & \tilde{\mathbf{e}}_{2n} & \tilde{\mathbf{e}}_{3n} & \tilde{\mathbf{e}}_{4n} \end{bmatrix}^T \tag{5.32}$$

$$\boldsymbol{\beta}_{ne} = \tilde{\mathbf{e}}_{n1} \tag{5.33}$$

$$\boldsymbol{\beta}_c = \begin{bmatrix} \tilde{\mathbf{b}}_1 & \tilde{\mathbf{b}}_2 & \tilde{\mathbf{b}}_3 & \tilde{\mathbf{b}}_4 \end{bmatrix}^T \tag{5.34}$$

$$\mathbf{X}_e = \begin{bmatrix} \mathbf{I} \\ \mathbf{I} \\ \mathbf{I} \\ \mathbf{I} \end{bmatrix} \tag{5.35}$$

$$\mathbf{X}_{nc} = \begin{bmatrix} \mathbf{0} & \mathbf{0} & \mathbf{0} & \mathbf{0} \\ \mathbf{I} & -\mathbf{I} & \mathbf{0} & \mathbf{0} \\ \mathbf{I} & \mathbf{0} & -\mathbf{I} & \mathbf{0} \\ \mathbf{I} & \mathbf{0} & \mathbf{0} & -\mathbf{I} \end{bmatrix} \tag{5.36}$$

The weight matrix for epoch n is also altered to

$$\mathbf{P} = \begin{bmatrix} \tilde{\mathbf{P}}_1 & \mathbf{0} & \mathbf{0} & \mathbf{0} \\ \mathbf{0} & \tilde{\mathbf{P}}_2 & \mathbf{0} & \mathbf{0} \\ \mathbf{0} & \mathbf{0} & \tilde{\mathbf{P}}_3 & \mathbf{0} \\ \mathbf{0} & \mathbf{0} & \mathbf{0} & \tilde{\mathbf{P}}_4 \end{bmatrix} \tag{5.37}$$

Similarly to the star camera quaternion combination, the constant parameters $\boldsymbol{\beta}_c$ are firstly calculated using Equation (5.26), which has the effect of achieving a relative calibration of the instruments. Then, Equation (5.28) is used to determine the new epoch-wise parameters $\boldsymbol{\beta}_{ne}$ and finally substituting both of them in the noise quaternion, the generalised least-squares estimate for the true quaternion can be obtained. Once again, based on the above description, it becomes apparent how straightforward and simple it is to extend the approach presented by Siemes et al. [2019] in order to include additional instruments that provide quaternion measurements with respect to a common reference frame.

5.2. Sensor data calibrations

This section describes the calibration techniques used for the star camera (Section 5.2.1), the IMU (Section 5.2.2) and the steering mirror (Section 5.2.3) data. In Section 5.2.4, a method for correcting FoV errors in the star camera quaternions is also presented.

5.2.1. SCA data calibration

Due to imperfect knowledge of the star cameras' orientation in the SF, when rotating the corresponding measured quaternions to the latter, constant biases can be observed between them. As pointed out by Siemes et al. [2019], the relative misalignment between a set of cameras can be detected by investigating the differences between the IBAs determined by a preliminary knowledge of their orientation in the SF and by in-flight measurements. Since the presence of such systematics could lead to a suboptimal quaternion combination, it is essential to align all star cameras in a common reference frame. As described in Section 5.1.1, this can be achieved by including additional terms that can model these offsets. The $\boldsymbol{\beta}_c$ variable represents the calibration parameters for the star camera data.

5.2.2. IMU data calibration

As indicated by Bandikova [2015], the accuracy of IMU measurements is limited by the stability of scaling factors and bias at low frequencies. Therefore, the calibration and alignment of the IMU with the star camera data is another crucial part for achieving an accurate reconstructed attitude. The first step before calibrating IMU data, is the identification of all possible error sources in gyroscope measurements. Based on the literature the most common errors that are modeled include the following [Bar-itzhack & Harman, 2002; Pittelkau, 2005]

- Misalignment error ($\Delta\mathbf{G}^m$)
- Scale factors ($\Delta\mathbf{G}^k$)
- Bias ($\Delta\mathbf{G}^b$)

These errors are assumed to be small compared to the measurements themselves, thus it is reasonable to define a linear gyro error model. Due to the linearity the contribution of each error source can be computed independently and then the total error can be determined as the sum of all. With this in mind, the total gyro error is written as

$$\Delta\mathbf{G} = \Delta\mathbf{G}^m + \Delta\mathbf{G}^k + \Delta\mathbf{G}^b \tag{5.38}$$

and is related to the measurement equations of a redundant IMU with

$$\boldsymbol{\omega}_g - \mathbf{H}\cdot\boldsymbol{\omega}_b = \Delta\mathbf{G} \tag{5.39}$$

where $\boldsymbol{\omega}_g$ is a column vector that contains angular rates sensed by each gyro, $\boldsymbol{\omega}_b = [\boldsymbol{\omega}_{b,x} \;\; \boldsymbol{\omega}_{b,y} \;\; \boldsymbol{\omega}_{b,z}]^T$ is a column vector with the angular rates of the satellite body and $\mathbf{H}$ is the sensor geometry matrix (see Equation (4.11)), that describes the orientation of each gyro in the SF. Note that the variable $\boldsymbol{\omega}_g$ is the same as $\mathbf{m}$ in Equation (4.11). In the following paragraphs, the derivation of the above-mentioned error sources is given and is based on the calibration procedures presented by Bar-itzhack and Harman [2002] and Pittelkau [2005].

Misalignment

Due to imperfect knowledge of the gyros' sensitive axis direction or the IMU's orientation in the SF, it is essential to calibrate and account for such misalignment errors. These can be expressed as the difference between the actual measurement and the nominal one, i.e.

$$\begin{aligned}\Delta\mathbf{G}^m &= \boldsymbol{\omega}_{g,\text{actual}} - \boldsymbol{\omega}_{g,\text{nominal}} \\ &= (\mathbf{H} + \Delta\mathbf{H})\boldsymbol{\omega}_b - \mathbf{H}\boldsymbol{\omega}_b \\ &= \Delta\mathbf{H}\boldsymbol{\omega}_b\end{aligned} \tag{5.40}$$

where $\Delta\mathbf{H}$ is a matrix that denotes small angle rotations around the two mutual perpendicular axes, $\mathbf{u}_i$ and $\mathbf{w}_i$, to the sensitive gyro axis, $\mathbf{s}_i$. For the i^{th} gyro, the latter is represented as $\mathbf{s}_i = [S_x^i \; S_y^i \; S_z^i]$, where $S_{x,y,z}^i$ denote the x, y and z directions of the gyro axis in the SF. The vector $\mathbf{u}_i$ can then be defined as

$$\mathbf{u}_i = \begin{bmatrix} -S_y^i & S_x^i & 0 \end{bmatrix} \tag{5.41}$$

Next, the vector $\mathbf{w}_i$ is defined as the cross product of the above two, i.e. $\mathbf{w}_i = \mathbf{u}_i \times \mathbf{s}_i$. Two small angle rotations D_i and E_i can then be attributed respectively around the axes $\mathbf{u}_i$ and $\mathbf{w}_i$ and the $\Delta\mathbf{H}$ matrix can be constructed as follows

$$\Delta\mathbf{H} = \begin{bmatrix} D_1 & 0 & 0 \\ 0 & D_2 & 0 \\ 0 & 0 & D_3 \end{bmatrix} \cdot \begin{bmatrix} \mathbf{u}_1 \\ \mathbf{u}_2 \\ \mathbf{u}_3 \end{bmatrix} + \begin{bmatrix} E_1 & 0 & 0 \\ 0 & E_2 & 0 \\ 0 & 0 & E_3 \end{bmatrix} \cdot \begin{bmatrix} \mathbf{w}_1 \\ \mathbf{w}_2 \\ \mathbf{w}_3 \end{bmatrix} \tag{5.42}$$

Finally, by substituting Equation (5.42) in Equation (5.40) and rearranging, the misalignment error can be determined by

$$\begin{aligned}\Delta\mathbf{G}^m &= \left(\begin{bmatrix} D_1 & 0 & 0 \\ 0 & D_2 & 0 \\ 0 & 0 & D_3 \end{bmatrix} \cdot \begin{bmatrix} \mathbf{u}_1 \\ \mathbf{u}_2 \\ \mathbf{u}_3 \end{bmatrix} + \begin{bmatrix} E_1 & 0 & 0 \\ 0 & E_2 & 0 \\ 0 & 0 & E_3 \end{bmatrix} \cdot \begin{bmatrix} \mathbf{w}_1 \\ \mathbf{w}_2 \\ \mathbf{w}_3 \end{bmatrix} \right) \boldsymbol{\omega}_b \\ &= \begin{bmatrix} \mathbf{u}_1 \cdot \boldsymbol{\omega}_b & 0 & 0 \\ 0 & \mathbf{u}_2 \cdot \boldsymbol{\omega}_b & 0 \\ 0 & 0 & \mathbf{u}_3 \cdot \boldsymbol{\omega}_b \end{bmatrix} \cdot \begin{bmatrix} D_1 \\ D_2 \\ D_3 \end{bmatrix} + \begin{bmatrix} \mathbf{w}_1 \cdot \boldsymbol{\omega}_b & 0 & 0 \\ 0 & \mathbf{w}_2 \cdot \boldsymbol{\omega}_b & 0 \\ 0 & 0 & \mathbf{w}_3 \cdot \boldsymbol{\omega}_b \end{bmatrix} \cdot \begin{bmatrix} E_1 \\ E_2 \\ E_3 \end{bmatrix} \\ &= \text{diag}(\mathbf{u}_{1,2,3} \cdot \boldsymbol{\omega}_b) \cdot \boldsymbol{D} + \text{diag}(\mathbf{w}_{1,2,3} \cdot \boldsymbol{\omega}_b) \cdot \boldsymbol{E}\end{aligned} \tag{5.43}$$

Scale factors

Similarly to the misalignment errors, the $\Delta\mathbf{G}^k$ error due to scale factors is defined as the difference between the actual and the nominal gyro measurement as

$$\begin{aligned}\Delta\mathbf{G}^k &= \boldsymbol{\omega}_{g,\text{actual}} - \boldsymbol{\omega}_{g,\text{nominal}} \\ &= \begin{bmatrix} \omega_{g1} \cdot k_1 \\ \omega_{g2} \cdot k_2 \\ \omega_{g3} \cdot k_3 \end{bmatrix} - \begin{bmatrix} \omega_{g1} \\ \omega_{g2} \\ \omega_{g3} \end{bmatrix} \\ &= \left(\begin{bmatrix} k_1 & 0 & 0 \\ 0 & k_2 & 0 \\ 0 & 0 & k_3 \end{bmatrix} - \mathbf{I}_{3\times3} \right) \cdot \begin{bmatrix} \omega_{g1} \\ \omega_{g2} \\ \omega_{g3} \end{bmatrix}\end{aligned} \tag{5.44}$$

where k_i is close to zero and $\mathbf{I}_{3\times3}$ is a identity matrix with dimensions 3×3. Then, defining the variable Δk_i as the difference $k_i - 1$ for $i = 1,2,3$, Equation (5.44) can be modified to

$$\begin{aligned}\Delta\mathbf{G}^k &= \begin{bmatrix} \omega_{g1} \cdot \Delta k_1 \\ \omega_{g2} \cdot \Delta k_2 \\ \omega_{g3} \cdot \Delta k_3 \end{bmatrix} \\ &= \begin{bmatrix} \omega_{g1} & 0 & 0 \\ 0 & \omega_{g2} & 0 \\ 0 & 0 & \omega_{g3} \end{bmatrix} \cdot \begin{bmatrix} \Delta k_1 \\ \Delta k_2 \\ \Delta k_3 \end{bmatrix} \\ &= \text{diag}(\omega_{g1,g2,g3}) \cdot \Delta\boldsymbol{k}\end{aligned} \tag{5.45}$$

Bias

The bias error model is fairly simple and can be expressed by the following equation

$$\Delta\mathbf{G}^b = \mathbf{I}_{3\times3} \cdot \mathbf{b} \tag{5.46}$$

where $\mathbf{b}$ is a column vector containing the corresponding biases for each gyro, i.e.

$$\mathbf{b} = \begin{bmatrix} b_{g1} & b_{g2} & b_{g3} \end{bmatrix}^T \tag{5.47}$$

Total error

Taking the above definitions into account and substituting Equation (5.43), (5.45) and (5.46) into (5.39), the total error is related to gyro measurements by

$$\begin{aligned} \boldsymbol{\omega}_g - H \cdot \boldsymbol{\omega}_b &= \Delta\mathbf{G} \\ &= \Delta\mathbf{G}^m + \Delta\mathbf{G}^k + \Delta\mathbf{G}^b \\ &= \text{diag}(\mathbf{u}_{1,2,3} \cdot \boldsymbol{\omega}_b) \cdot \mathbf{D} + \text{diag}(\mathbf{w}_{1,2,3} \cdot \boldsymbol{\omega}_b) \cdot \mathbf{E} + \text{diag}(\omega_{g1,g2,g3}) \cdot \Delta\boldsymbol{k} + \mathbf{I}_{3\times3} \cdot \mathbf{b} \end{aligned} \tag{5.48}$$

The above relation can also be written in the form of a generalised least-squares adjustment, i.e.

$$\mathbf{y} = \mathbf{A}\mathbf{x} + \boldsymbol{\epsilon} \tag{5.49}$$

where the observation vector $\mathbf{y}$, parameter vector $\mathbf{x}$ and design matrix $\mathbf{A}$ are defined as follows:

$$\mathbf{y} = \boldsymbol{\omega}_g - H \cdot \boldsymbol{\omega}_b \tag{5.50}$$

$$\mathbf{x} = \begin{bmatrix} \mathbf{D} & \mathbf{E} & \Delta\boldsymbol{k} & \mathbf{b} \end{bmatrix}^T \tag{5.51}$$

$$\mathbf{A} = \begin{bmatrix} \text{diag}(\mathbf{u}_{1,2,3} \cdot \boldsymbol{\omega}_b) & \text{diag}(\mathbf{w}_{1,2,3} \cdot \boldsymbol{\omega}_b) & \text{diag}(\omega_{g1,g2,g3}) & \mathbf{I}_{3\times3} \end{bmatrix} \tag{5.52}$$

The unweighted least squares solution $\hat{\mathbf{x}}$ of the system can then be computed with

$$\hat{\mathbf{x}} = (\mathbf{A}^T\mathbf{A})^{-1}\mathbf{A}^T\mathbf{y} \tag{5.53}$$

A perfect IMU data calibration could be achieved given the true satellite angular rates, however, this is not possible and instead the angular rates derived from the optimally combined star camera quaternions are used.

5.2.3. LSM data calibration

Similarly to the star cameras, the laser ranging interferometer and in turn the steering mirrors could be affected by biases due to imperfections in the mounting of the instrument on the satellite. As described in Section 5.1.2, steering mirror quaternions can be included in the optimal quaternion process of Section 5.1.1 and new constant biases (i.e. $\boldsymbol{\beta}_c$) can be calculated. Once again, when these calibration parameters are applied on the steering mirrors and the three star cameras, the relative alignment of all instruments can be accomplished.

Additionally, as indicated by Kornfeld et al. [2019], the rotational alignment requirement of the laser ranging interferometer's triple mirror assembly with respect to the accelerometer is stricter compared to the star cameras, i.e. $\pm$ 0.25 mrad in contrast to $\pm$ 20 mrad in all three axes, respectively. Based on this, one could assume that the knowledge of the steering mirrors in the SF could be more accurate in comparison to the star cameras. Considering also that their measurements are ten times more accurate, it could beneficial to use them in the calibration process of these two instruments.

5.2.4. Quaternions correction

A key element for the attitude reconstruction process of GRACE-FO is the correction of FoV errors present in the star camera measurements. One way to accomplish this is by taking advantage of another set of quaternions that are not affected by such type of errors. For example, IMU-based quaternions can be used for GRACE-FO. In principle, these quaternions describe the same attitude as the ones from the star cameras, however, as it will be discussed in Section 7.5.1, due to an increased noise at low to mid frequencies they are not considered as the final reconstructed attitude. Instead, given the IMU-based and star camera quaternion residuals, a daily

average correction can be determined, that relates to FoV type of errors found in the star camera measurements. This relation is justified from the fact that stars in the FoV are nearly repeated from one orbit to the next and stay within the FoV for some time. Therefore, it is reasonable to expect that 1) the same type of errors are repeated across a time window at same locations along the orbit and 2) for the quaternion residuals to reveal these systematic errors, since the non-star-camera quaternions are not influenced by the latter. The advantage of averaging their residuals within a time period is the elimination of the noise present in the IMU-based quaternions.

With this in mind, the first step towards correcting FoV star camera errors is to compute the residuals between the star camera quaternions ($\mathbf{q}_n^{\mathrm{SCA}}$) and another set ($\mathbf{q}_n$) which is not or less influenced by such errors. In equation form this is written as

$$\mathbf{q}_n^{\mathrm{diff}} = \begin{bmatrix} 1 \\ \frac{1}{2}\mathbf{d}_n \end{bmatrix} = (\mathbf{q}_n^{\mathrm{SCA}})^* \mathbf{q}_n \tag{5.54}$$

where $\mathbf{d}$ is a vector that contains three small rotation angles and n indicates the epoch. Afterwards, based on the orbital position of the satellite, the corresponding argument of latitude can be determined as a function of time. The correction quaternions ($\mathbf{q}_n^{\mathrm{corr}}$) are then defined such that the value for all epochs n, that lay within a specified time interval of duration T and have the same argument of latitude, is equal to the average quaternion difference computed in Equation (5.54). Within this MSc project a T value of 1 day was used. Finally, the resulting quaternions are applied to the ones of the star cameras, as shown in Equation (5.55), to obtain the FoV error free quaternions.

$$\mathbf{q}_{\mathrm{corr},n}^{\mathrm{SCA}} = \mathbf{q}_n^{\mathrm{SCA}} \mathbf{q}_n^{\mathrm{corr}} \tag{5.55}$$

5.3. Angular rate reconstruction

Given a proper calibration of star camera, steering mirror and IMU data and a successful quaternion combination procedure, a combination at the level of angular rates can now be performed. The same approach as presented by Siemes [2018] is proposed for the GRACE-FO mission, but now the angular rates of the satellite are reconstructed from IMU and combined star camera measurements. The combination is performed in the frequency domain by taking into account the noise PSD of each instrument. Specifically, a lowpass and a highpass filter is constructed for the angular rates of the star cameras and the IMU, respectively. The lowpass filter is used for the former, because during the differentiation of the quaternions, the noise PSD of the star cameras tilts such that low-frequency noise is dampened and high-frequency is amplified. In contrast, the IMU measurements are known to have a far lower noise floor at high frequencies, but a rather amplified noise at low frequencies. Then, since the measurements of both instruments are concurrent, the lowpass and highpass filtered star camera and IMU angular rates can be added in the frequency domain to arrive at a more accurate result. The motivation behind the choice of this algorithm is the improved gravity gradients and gravity field models that were observed for the GOCE mission, when this method was used instead of a combination in the time domain by means of Kalman filtering [Stummer et al., 2012].

The first step for the GRACE-FO angular rate reconstruction is the derivation of IMU and combined star camera satellite angular rates. This can be achieved using the equations described in Section 4.2.1 and Section 4.2.2. Next, the process of constructing symmetric moving-average filters starts by defining the general shape of the noise PSD of the angular rates for both instruments. This can be achieved using equation

$$\boldsymbol{P}_S = \boldsymbol{f}^{a_S} \quad \text{and} \quad \boldsymbol{P}_G = c\boldsymbol{f}^{a_G} \tag{5.56}$$

where $\boldsymbol{f}$ is the frequency vector, $\boldsymbol{P}_S$ and $\boldsymbol{P}_G$ are the noise PSD of the star camera and IMU angular rates respectively, a_S and a_G are the slopes of these PSDs in the logarithmic domain and

$$c = (f^{\mathrm{cross}})^{a_S - a_G} \tag{5.57}$$

is a scale factor depending on the frequency f^{cross} that determines where $\boldsymbol{P}_S$ and $\boldsymbol{P}_G$ cross each other. The frequency vector $\boldsymbol{f}$ is equal in length to the length of the filters, denoted by N_F. In order to achieve a sufficient resolution in the spectral domain, N_F must be a large enough odd integer. Siemes [2018] recommended to use

$$N_F \approx \frac{10}{f^{\mathrm{cross}}} \tag{5.58}$$

The next step is to make the PSD curves symmetric around the mid-frequency and then compute the spectral weights, or otherwise called the Wiener weights, for the star camera angular rates. For the non-zero frequencies the weights are determined by

$$\boldsymbol{W}_S = \frac{\boldsymbol{P}_G}{\boldsymbol{P}_G + \boldsymbol{P}_S} \tag{5.59}$$

and for the zero frequency the weight is defined to be equal to 1. At that point, the filter coefficients $\boldsymbol{F}_S$ can be calculated by simply taking the inverse discrete Fourier transform of $\boldsymbol{W}_S$, i.e. $\boldsymbol{F}_S = \text{ifft}(\mathbf{W}_S)$. Finally the low-pass filter of the star camera angular rates is constructed by rearranging the previously calculated coefficients according to

$$\boldsymbol{F}_S = \begin{bmatrix} F_{S,K+1} & F_{S,K+2} & \cdots & F_{S,N_f} & F_{S,1} & F_{S,2} & \cdots & F_{S,K} \end{bmatrix} \tag{5.60}$$

where K is the index of the mid-frequency. Finally, a complementary highpass filter is constructed for the IMU by spectral inversion. This is accomplished by flipping the sign of each coefficient of the lowpass filter and then adding 1 to the coefficient at the center of symmetry.

The above mentioned procedure is run three times, so that three angular rate reconstruction filters are determined for each component of the angular rate vector with a different cut-off frequency depending on the noise characteristics of each one of them. Subsequently, the filters can be applied to the angular rate measurements of each instrument in the time domain as a convolution or in the frequency domain as an element-wise multiplication. In equation form, the corresponding reconstructed satellite angular rates $\boldsymbol{\omega}_{R,i}$, where $i \in \{x, y, z\}$ denotes the element of the vector, are

$$\boldsymbol{\omega}_{R,i} = \mathbf{F}_{S,i} * \boldsymbol{\omega}_{S,i} + \mathbf{F}_{G,i} * \boldsymbol{\omega}_{G,i} \tag{5.61}$$

and the asterisk indicates the filter operation.

In general, when applying a symmetric moving-average filter, transient effects are produced from the filter operations at the beginning and the end of the time series. However, an advantage of this angular rate reconstruction method is that such effects can be reduced by simply constructing filters with shorter length towards these areas. Specifically, for the first epoch of the filtered time series, a filter of length equal to 1 is created and applied to only the first value of the input time series. For the second epoch, a filter of length equal to 3 is created and applied to the first three values of the input time series, and so forth until half the length of the primary filter is reached. The same procedure is applied for the end of the filtered time series. Finally, since the transient effects cannot be avoided for the first and last few epochs, the IMU angular rates are extrapolated after fitting them to the sum of the filtered star camera and IMU angular rates.

5.4. Attitude reconstruction

The final step for acquiring an accurate attitude estimate for the GRACE-FO satellites is to improve the attitude quaternions provided by the star cameras by incorporating valuable information from a set of reconstructed angular rates. In Section 5.4.1 the proposed attitude reconstruction algorithm for GRACE-FO is described in detail. Next, Section 5.4.2 presents four possible scenarios, identified during this MSc project, for combining star camera, IMU and steering mirror data as part of the overall GRACE-FO attitude reconstruction process.

5.4.1. Algorithm

The goal of the attitude reconstruction is to obtain the best possible estimation of the satellites' inertial attitude, by combining available star camera quaternions and the reconstructed angular rates. This is essential for the GRACE-FO mission, because attitude errors can influence the measured distance between the CoMs of the satellites as well as the accelerations projected on the CoM-to-CoM line, which in turn will affect the estimated gravity field models. The same approach as described by Siemes [2018] is proposed for the GRACE-FO mission, for which attitude quaternions resulting from the reconstructed angular rates are fitted to the combined star camera quaternions. In other words, the reconstruct angular rates can be integrated to find how the attitude changes from a central epoch to adjacent epochs (i.e. before and after the central epoch). These changes can be expressed in the form of a rotation quaternion, which is expected to be smoother than the combined star cameras since it includes IMU angular rates, which are more accurate at high frequencies. However, due to the integration, small errors will accumulate resulting in an increased low frequency noise. The reconstructed angular rate quaternions can be fitted to the combined star camera quaternions by means of a generalised least squares adjustment, to minimize the errors across all frequencies. An important element of this adjustment is taking into account the covariances of the star camera quaternions and how the variance of the rotation quaternion changes grows when moving away from the central epoch. Once again, this algorithm in combination with the one described in Section 5.3 are chosen, because they provided the GOCE mission with improved attitude quaternions and gravity field models compared to the previous approach that was determining the inertial attitude by means of Kalman filtering [Stummer et al., 2012].

The derivation of this algorithms starts by defining the measured quaternion $\mathbf{q}_n^{\text{meas}}$ as the quaternion originating from the combined star cameras and the rotation quaternion $\mathbf{q}_{n\rightarrow n+k}^{\text{rot}}$ which results from the integration

of the reconstructed angular rates and describes the rotation from epoch t_n to t_{n+k}. With this in mind, the measured quaternion $\mathbf{q}_{n+k}^{\text{meas}}$ can be expressed as a rotated version of the true quaternion $\mathbf{q}_n^{\text{true}}$, i.e.

$$\mathbf{q}_{n+k}^{\text{meas}} = \mathbf{q}_{n+k}^{\text{noise}} \mathbf{q}_n^{\text{true}} \mathbf{q}_{n\rightarrow n+k}^{\text{rot}} \tag{5.62}$$

where $\mathbf{q}_{n+k}^{\text{noise}}$ is the noise quaternion that reflects the effect of both 1) the noise of the combined star camera attitude quaternions and 2) the noise of the rotation quaternion which results from the integration of the reconstructed angular rates. Moreover, $\mathbf{q}_{n+k}^{\text{noise}}$ represents small angle rotations, i.e.

$$\mathbf{q}_{n+k}^{\text{noise}} = \begin{bmatrix} 1 & \epsilon_{x,n+k}/2 & \epsilon_{y,n+k}/2 & \epsilon_{z,n+k}/2 \end{bmatrix}^T \tag{5.63}$$

As far as the rotation quaternion is concerned, it can be decomposed into a series of rotations such that

$$\mathbf{q}_{n\rightarrow n+k}^{\text{rot}} = \mathbf{q}_{n\rightarrow n+1}^{\text{rot}} \mathbf{q}_{n+1\rightarrow n+2}^{\text{rot}} \cdots \mathbf{q}_{n+k-1\rightarrow n+k}^{\text{rot}} \tag{5.64}$$

Then, the reconstructed angular rates are related to $\mathbf{q}_{n+i\rightarrow n+i+1}^{\text{rot}}$ according to the following relations:

$$\mathbf{q}_{n+i\rightarrow n+i+1}^{\text{rot}} = \begin{bmatrix} \cos(\phi/2) \\ \sin(\phi/2)\mathbf{e} \end{bmatrix} \quad \text{for} \quad i \in \{0, ..., k-1\} \tag{5.65}$$

where ϕ is the angle of rotation and $\mathbf{e}$ is the rotation axis and can be computed with

$$\phi = \frac{|\boldsymbol{\omega}_{n+i+1} + \boldsymbol{\omega}_{n+i}|}{2} \tag{5.66}$$

$$\mathbf{e} = \frac{\boldsymbol{\omega}_{n+i+1} + \boldsymbol{\omega}_{n+i}}{|\boldsymbol{\omega}_{n+i+1} + \boldsymbol{\omega}_{n+i}|} \tag{5.67}$$

Since the two unknown variables of Equation (5.62), i.e. $\mathbf{q}_n^{\text{true}}$ and $\mathbf{q}_{n+k}^{\text{noise}}$ would lead to a non-linear mixed model (Gauß-Helmert model), the problem is reformulated in a such a way that a linear generalised least squares can be used. This is accomplished by first defining the relative error of the quaternion of epoch n and $n+k$

$$\mathbf{q}_{n,n+k}^{\text{rel}} = \mathbf{q}_n^{\text{noise}} (\mathbf{q}_{n+k}^{\text{noise}})^* \tag{5.68}$$

Next, based on Equation (5.62) the noise quaternions at epoch n and $n+k$ are equal to

$$\mathbf{q}_{n+k}^{\text{noise}} = \mathbf{q}_{n+k}^{\text{meas}} \left(\mathbf{q}_n^{\text{true}} \mathbf{q}_{n\rightarrow n+k}^{\text{rot}}\right)^* \tag{5.69}$$

$$\mathbf{q}_n^{\text{noise}} = \mathbf{q}_n^{\text{meas}} (\mathbf{q}_n^{\text{true}} \mathbf{q}_{n\rightarrow n}^{\text{rot}})^* = \mathbf{q}_n^{\text{meas}} (\mathbf{q}_n^{\text{true}})^* \tag{5.70}$$

and can be substituted to Equation (5.68)

$$\begin{aligned} \mathbf{q}_{n,n+k}^{\text{rel}} =& \mathbf{q}_n^{\text{meas}} (\mathbf{q}_n^{\text{true}})^* \left(\mathbf{q}_{n+k}^{\text{meas}} \left(\mathbf{q}_n^{\text{true}} \mathbf{q}_{n\rightarrow n+k}^{\text{rot}}\right)^*\right)^* \\ =& \mathbf{q}_n^{\text{meas}} (\mathbf{q}_n^{\text{true}})^* \mathbf{q}_n^{\text{true}} \mathbf{q}_{n\rightarrow n+k}^{\text{rot}} (\mathbf{q}_{n+k}^{\text{meas}})^* \\ =& \mathbf{q}_n^{\text{meas}} \mathbf{q}_{n\rightarrow n+k}^{\text{rot}} (\mathbf{q}_{n+k}^{\text{meas}})^* \end{aligned} \tag{5.71}$$

From the above equation, it becomes apparent that despite the fact that the relative error of epoch n and $n+k$ quaternions is the product of two unknown noise quaternions, it can still be calculated. Since both of those noise quaternions represent small angles, the same can be assumed for $\mathbf{q}_{n,n+k}^{\text{rel}}$, i.e.

$$\mathbf{q}_{n,n+k}^{\text{rel}} = \begin{bmatrix} 1 & \delta_{x,n,n+k}/2 & \delta_{y,n,n+k}/2 & \delta_{z,n,n+k}/2 \end{bmatrix}^T \tag{5.72}$$

Taking small angle approximations into account and after rearranging Equation (5.68) to $\mathbf{q}_{n,n+k}^{\text{rel}} \mathbf{q}_{n+k}^{\text{noise}} = \mathbf{q}_n^{\text{noise}}$, the latter can also be expressed as

$$\mathbf{d}_{n,n+k} + \mathbf{e}_{n+k} = \mathbf{e}_n + \mathcal{O}(\epsilon^2) \tag{5.73}$$

where

$$\mathbf{d}_{n,n+k} = \begin{bmatrix} \delta_{x,n,n+k} \\ \delta_{y,n,n+k} \\ \delta_{z,n,n+k} \end{bmatrix}, \quad \mathbf{e}_n = \begin{bmatrix} \epsilon_{x,n} \\ \epsilon_{y,n} \\ \epsilon_{z,n} \end{bmatrix} \quad \text{and} \quad \mathbf{e}_{n+k} = \begin{bmatrix} \epsilon_{x,n+k} \\ \epsilon_{y,n+k} \\ \epsilon_{z,n+k} \end{bmatrix} \tag{5.74}$$

are small angles. At this point, Equation (5.73) can be written in the form of a generalised least-squares adjustment ($\mathbf{y}+\mathbf{u}=\mathbf{A}\mathbf{x}$) with $\mathbf{y}$ being the observation vector, $\mathbf{u}$ the residual vector, $\mathbf{A}$ the design matrix and $\mathbf{x}$ the parameter vector. In particular,

$$\underbrace{\begin{bmatrix}\mathbf{d}_{n,n-K}\\ \vdots\\ \mathbf{d}_{n,n-1}\\ \mathbf{0}\\ \mathbf{d}_{n,n+1}\\ \vdots\\ \mathbf{d}_{n,n+K}\end{bmatrix}}_{\mathbf{y}}+\underbrace{\begin{bmatrix}\mathbf{e}_{n-K}\\ \vdots\\ \mathbf{e}_{n-1}\\ \mathbf{e}_{n}\\ \mathbf{e}_{n+1}\\ \vdots\\ \mathbf{e}_{n+K}\end{bmatrix}}_{\mathbf{u}}=\underbrace{\begin{bmatrix}\mathbf{I}\\ \vdots\\ \mathbf{I}\\ \mathbf{I}\\ \mathbf{I}\\ \vdots\\ \mathbf{I}\end{bmatrix}}_{\mathbf{A}}\tilde{\mathbf{e}}_n \tag{5.75}$$

where $\tilde{\mathbf{e}}_n$ are the parameters. By inspection of Equation (5.75), it is obvious that the noise in the quaternion at the central epoch n relates to the noise in the quaternions of epoch $n-K$ and $n+K$ before and after that.

For an accurate estimation of $\tilde{\mathbf{e}}_n$, it is essential to construct a proper covariance matrix of $\mathbf{e}_{n+k}$ for $k=-K,...,K$. As stated before, the noise quaternion $\mathbf{q}^{\text{noise}}_{n+k}$ reflects both the noise of the combined star camera quaternions and of the rotation quaternions. From the algorithm, presented in Section 5.1.1, the covariance information of the combined attitude quaternions is provided. In practice, the latter is expected to exhibit some time correlation between epochs a few minutes apart and from one orbit to the next. This is due to the fact that stars in the FoV change slowly along the orbit and are nearly repeated from one orbit to the next. As far as the noise of $\mathbf{q}^{\text{rot}}_{n\rightarrow n+k}$ is concerned, it is also expected to show large time correlations because of the angular rates integration. Correlations are also expected between $\mathbf{q}^{\text{rot}}_{n\rightarrow n+k}$ and $\mathbf{q}^{\text{meas}}_{n+k}$, since the latter are used for the calculation of the former. With all this in mind, the covariance matrix for the generalised least-squares should be fully populated, however, this would lead to a significantly high computational effort. For this reason, time correlations are ignored, which reduces the matrix to a block-diagonal structure, with one 3×3 block per epoch [Siemes, 2018]. In equation form it can be written as

$$\mathbf{\Sigma}=\begin{bmatrix}\mathbf{\Sigma}_{n-K} & \mathbf{0} & \cdots & \mathbf{0}\\ \mathbf{0} & \mathbf{\Sigma}_{n-K+1} & \ddots & \vdots\\ \vdots & \ddots & \ddots & \mathbf{0}\\ \mathbf{0} & \cdots & \mathbf{0} & \mathbf{\Sigma}_{n+K}\end{bmatrix} \tag{5.76}$$

where each block is of dimension 3×3 and amounts to the sum of the covariance matrix of the combined star camera quaternions and the covariance matrix of the rotation quaternions. In equation form:

$$\mathbf{\Sigma}_{n+k}=\mathbf{\Sigma}^{\text{meas}}_{n+k}+\mathbf{\Sigma}^{\text{rot}}_{n+k}\quad\text{for}\quad k=-K,...,K \tag{5.77}$$

The covariance matrices $\mathbf{\Sigma}^{\text{meas}}_{n+k}$ is the product of the posteriori variance factor σ_0^2 and the cofactor matrices $\boldsymbol{Q}_1,...,\boldsymbol{Q}_{123}$, both of which are by-products of the star camera quaternion combination algorithm, i.e.

$$\mathbf{\Sigma}^{\text{meas}}_{SCA_1,n+k}=\sigma_0^2\boldsymbol{Q}_1,\ \cdots,\mathbf{\Sigma}^{\text{meas}}_{SCA_{123},n+k}=\sigma_0^2\boldsymbol{Q}_{123} \tag{5.78}$$

where the subscript 123 denotes that all three star camera quaternions were available and used for the combination. Additionally, the variance factor can be calculated as

$$\sigma_0^2=\frac{\Omega}{R} \tag{5.79}$$

where Ω is the square-sum of residuals of the combined star camera quaternions and R is the redundancy. It is calculated from the flags of the individual star camera quaternions ($\boldsymbol{f}_{SCA_1}$, $\boldsymbol{f}_{SCA_2}$ and $\boldsymbol{f}_{SCA_3}$), which indicate whether data are valid or invalid at a certain epoch, and the flags of the combined quaternions ($\boldsymbol{f}$), i.e.

$$R=3\sum_{n=1}^{N}(f_n-f_{SCA_1,n}-f_{SCA_2,n}-f_{SCA_3,n}) \tag{5.80}$$

Next, the covariance matrix $\mathbf{\Sigma}^{\text{rot}}_{n+k}$ is modelled as the diagonal matrix

$$\mathbf{\Sigma}^{\text{rot}}_{n+k}=\begin{bmatrix}\sigma_x^2 & 0 & 0\\ 0 & \sigma_y^2 & 0\\ 0 & 0 & \sigma_z^2\end{bmatrix} \tag{5.81}$$

where σ_x^2, σ_y^2 and σ_z^2 are empirically determined quadratic functions of the time difference $|t_{n+k} - t_n|$. They are calculated from the residuals between the combined star camera quaternions and the quaternions originating from rotating an initial quaternion based on the reconstructed angular rates.

With all this in mind, the $\tilde{\mathbf{e}}_n$ parameters of the noise quaternion can now be estimated. Finally, the reconstructed attitude quaternion for epoch n is obtained with $\mathbf{q}_n^{\text{rec}} = (\mathbf{q}_n^{\text{noise}})^* \mathbf{q}_n^{\text{meas}}$.

5.4.2. Scenarios

Given the optimal quaternion combination, angular rate and attitude reconstruction algorithms as well as the various data calibrations techniques, four different scenarios have been identified that could provide the final attitude estimate for the GRACE-FO satellites. Initially, the attitude reconstruction was performed based on the first, or otherwise called nominal, scenario depicted in Figure 5.1. The process starts by calibrating the star camera data and calculating the constant biases based on star camera and steering mirror quaternions. Next follows the optimal combination of the star camera quaternions from which the corresponding angular rates can be determined. The latter are used to calibrate the IMU data and, then, together with the IMU angular rates obtain the reconstructed angular rates. Finally, these are used in combination with the optimally combined star camera quaternions to reconstruct the attitude.

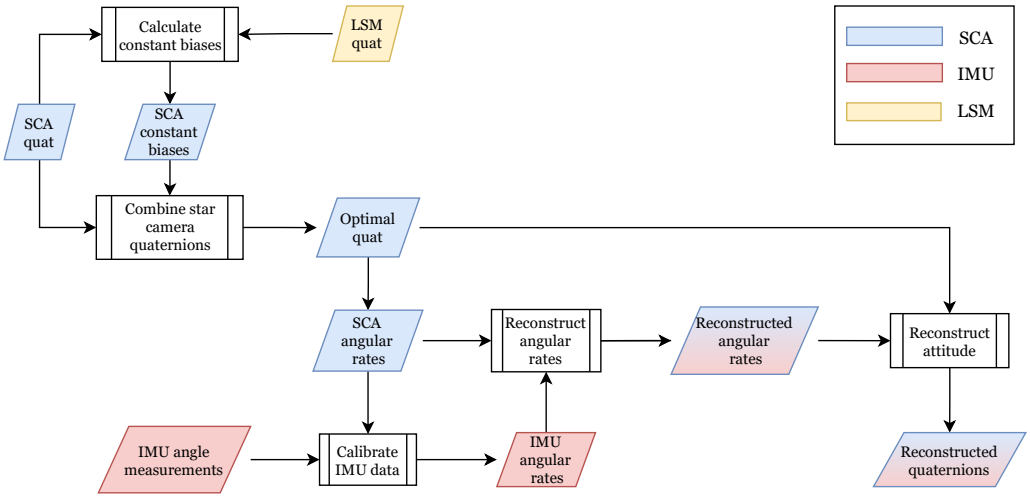

Figure 5.1: Flowchart of the 1st (nominal) scenario for the attitude reconstruction of the GRACE-FO satellites.

Although, the approach described above provided a far more accurate attitude estimate than what could be achieved from the combined star cameras, a major systematic error was still prominent in the reconstructed quaternions. As it will be demonstrated in Section 7.5, this error is associated to FoV errors present in the star camera measurements. In order to account for these errors, the following three scenarios were identified. For the first one, shown in Figure 5.2, the steering mirror quaternions, that are not affected by such type of errors, are optimally combined with the individual star camera quaternions based on the method presented in Section 5.1.2. During the combination the proper quaternion weighting scheme is applied so that the higher accuracy of the LSM measurements is taken into account. Afterwards, the optimal quaternions are used to calibrate the IMU data and, together with a new set of reconstructed angular rates, reconstruct the final attitude.

For the last two scenarios, depicted respectively in Figure 5.3 and Figure 5.4, the same procedure is followed as with the nominal case, but now correction quaternions are derived from IMU and steering mirror data and applied at the level of the nominal reconstructed quaternions. This set of correction quaternions represent daily average corrections and are computed according to the method presented in Section 5.2.4. For the case of the IMU, a set of IMU-based quaternions are used for this purpose, which are derived using the optimally combined star camera quaternions, the IMU angular rates and a larger time window during the quaternion fitting in the attitude reconstruction algorithm. For the correction based on steering mirror data, derived steering mirror quaternions are used.

It should be mentioned that one main difference between the options with the LSM and the one with the IMU, is that the former do not correct for any star camera FoV errors in the x-component of the quaternions. This is because the steering mirrors cannot measure the roll variations of the satellites. Still, the corresponding correction applied by the IMU-based quaternions does not have any contribution to the AOC, as seen from

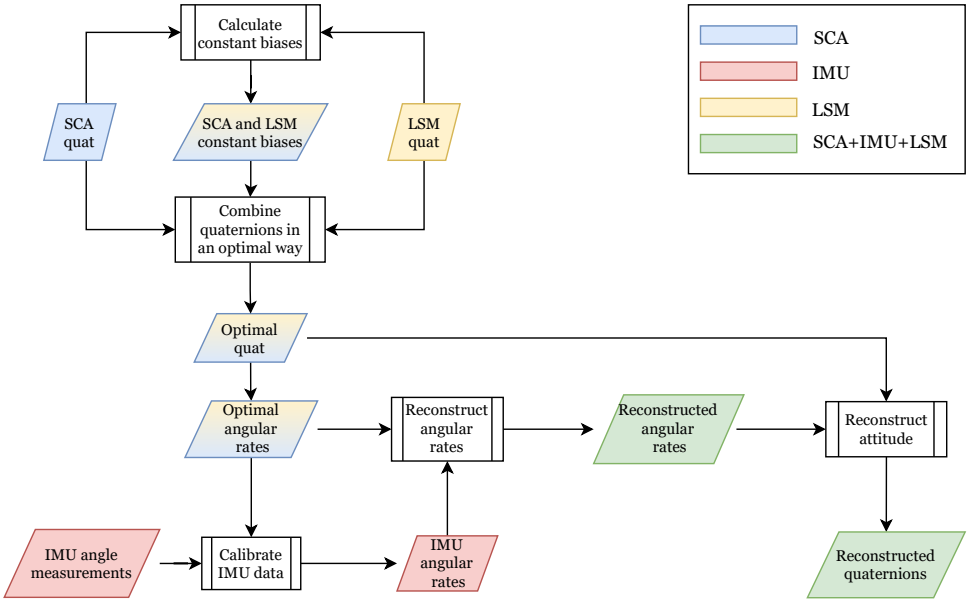

Figure 5.2: Flowchart of the 2nd scenario for the attitude reconstruction of the GRACE-FO satellites.

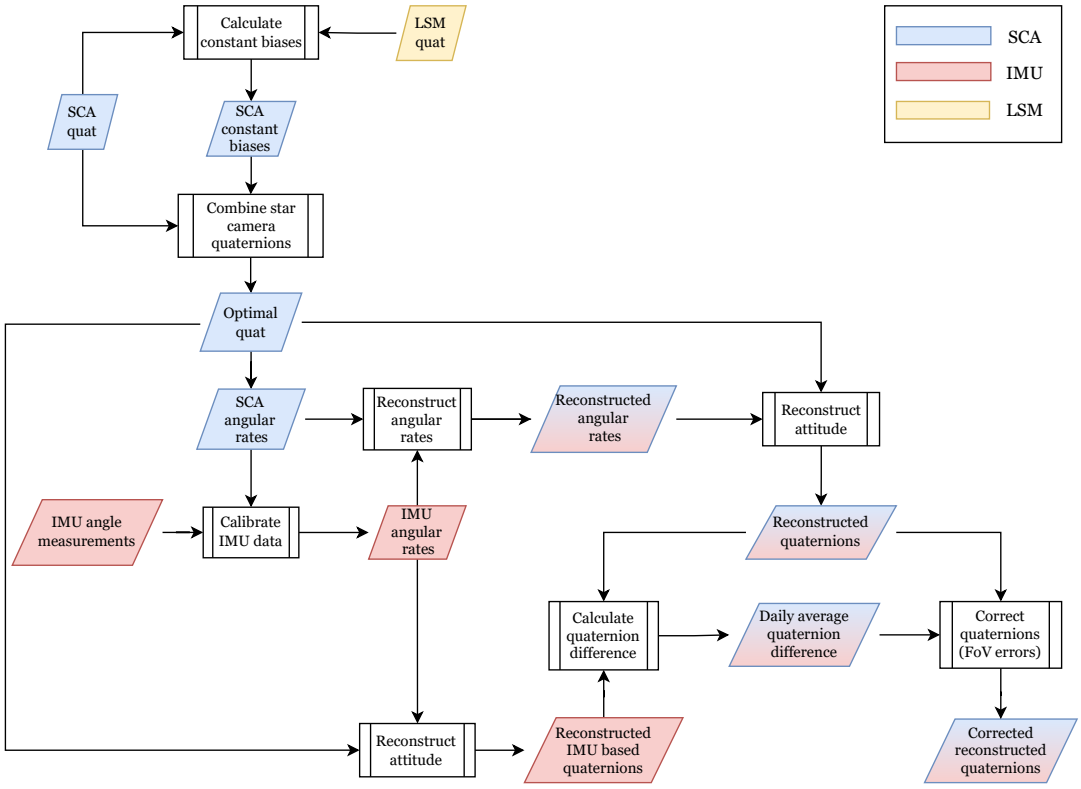

Figure 5.3: Flowchart of the 3rd scenario for the attitude reconstruction of the GRACE-FO satellites.

Equation (4.25). The performance of each of the four proposed attitude reconstruction scenarios is further evaluated in Section 7.5.

Lastly, for the last two scenarios, a different variation was also tested for which the daily average quaternion correction was applied at the level of the individual star camera measurements and, then, the nominal attitude reconstruction procedure was followed. The results obtained in this way, however, were degraded and worse than the nominal case. The reason behind this is the anisotropic accuracy in the pure star camera measurements and the limitation of the method presented in Section 5.2.4. The high noise around the boresight

axis of a star camera contaminates the other axes when quaternions are rotated from the SCF to the SF. This causes an increased noise floor, which in turn prevents for any distinct daily average quaternion correction to be computed, because the latter has now a large percentage of noise within it.

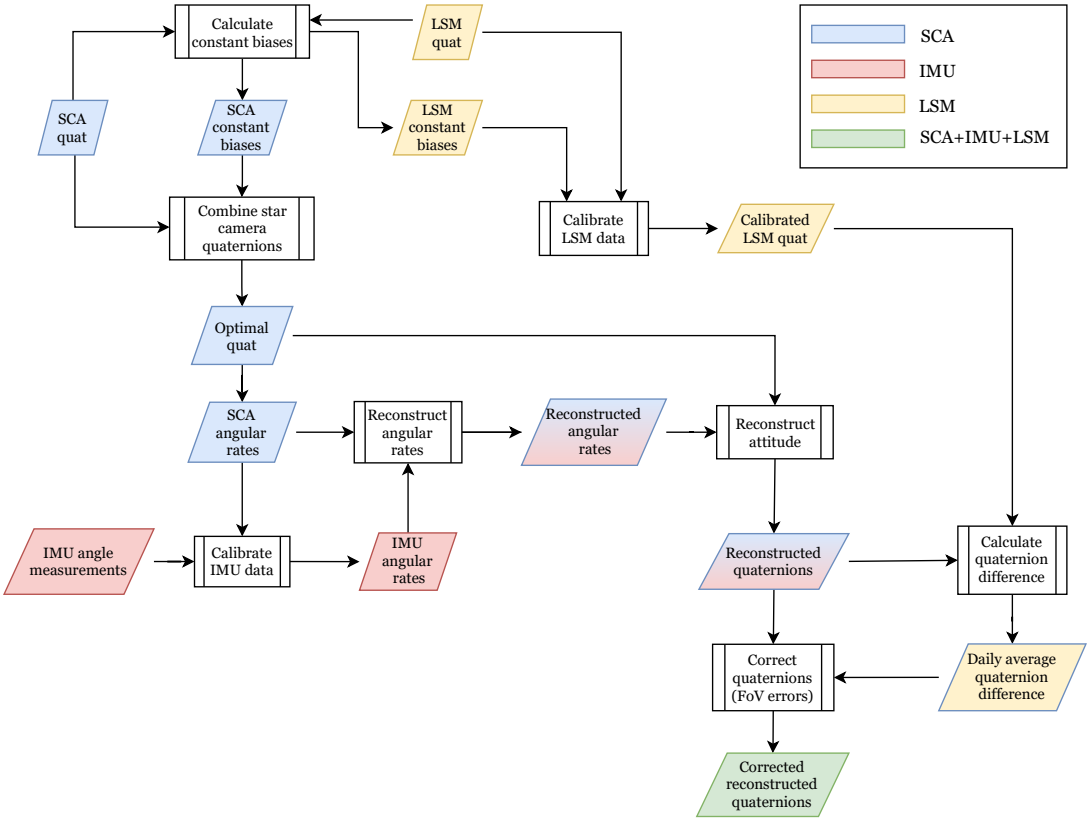

Figure 5.4: Flowchart of the 4th scenario for the attitude reconstruction of the GRACE-FO satellites.

6

Verification and Validation

This chapter is dedicated to the different steps undertaken to verify and validate the various processing and sensor data fusion algorithms implemented and used during this thesis work. A key element for the attitude reconstruction process is the derivation of the satellites' angular rates from star camera and IMU measurements. The verification of these algorithms is described in Section 6.1. Next, in Section 6.2 the derivation of inter-satellite pointing angles is validated. Lastly, in Section 6.3 and Section 6.4 the optimal quaternion combination and the angular rate and attitude reconstruction algorithms are verified for the GRACE-FO mission. In Table 6.1, an overview of the above-mentioned algorithms is presented with the corresponding section in the report where they have been described and verified.

Table 6.1: Overview of the various processing and sensor data fusion algorithms verified within this chapter.

Algorithm	**Described in**	**Verified in**
Star camera angular rates	Section 4.2.1	Section 6.1
IMU angular rates	Section 4.2.2	Section 6.1
Inter-satellite pointing angles	Section 4.1	Section 6.2
Optimal combination of quaternions	Section 5.1	Section 6.3
Angular rate reconstruction	Section 5.3	Section 6.4
Attitude reconstruction	Section 5.4.1	Section 6.4

6.1. Satellite angular rates

Several methods have been utilized to verify the derivation of the angular rates from each instrument. A first simple check is to examine the magnitude and sign of the latter around each axes of the SF. In general, the x axis of the SF points to the other satellite, the z axis points in nadir direction and the y axis completes a right-hand system. Therefore, for both satellites the angular rate around the y axis is expected to have a mean absolute value of about 1.108 mrad/s and for the other two axes to be centered around 0. The mean value of 1.108 mrad/s corresponds to the rotation rate of the satellite around the Earth over the course of one orbit, which can be calculated as follows

$$\omega_y = \frac{2\pi}{T} = \frac{2\pi}{94.5 * 60} \approx 1.108 \text{ mrad/s} \tag{6.1}$$

where T is the orbital period of the satellite, which is equal to approximately 94.5 minutes. According to the right-hand rule, for the trailing satellite that has its x axis pointing in the flight direction, the sign of ω_y will be negative [Groves, 2008]. While for the leading satellite, for which the body frame is an 180 degrees rotated around the z axis version of the other, ω_y will be positive. Based on the orbital positions of the satellites, it is known that during this period GRACE-FO C is the leading satellite and GRACE-FO D is trailing behind. In Figure 6.3 and Figure 6.2, long time series of the combined star camera and IMU derived angular rates around the y axis are depicted for both satellites. Indeed, the results indicate that GRACE-FO C is in front while GRACE-FO D is pursuing and the calculated magnitudes match with the expected values for both satellites. It should be noted that the displayed combined star camera angular rates are lowpass filtered in order to remove the high frequency noise in their measurements and clearly show the similarities with the IMU.

With this in mind, the rest of the verification process of angular rates will be focused only on one satellite, i.e. GRACE-FO C, since no other differences exist between the two. Additionally, in all of the figures, the results from the official attitude data product (denoted as SCA1B) of GRACE-FO are included, to provide another way of verifying the calculations of the angular rates. In Figure 6.3 and Figure 6.4, the derived angular rates around the x and z axis of the satellite are shown, respectively. Once again, the behavior of the results is according to what is expected, since both ω_x and ω_z are centered around 0.

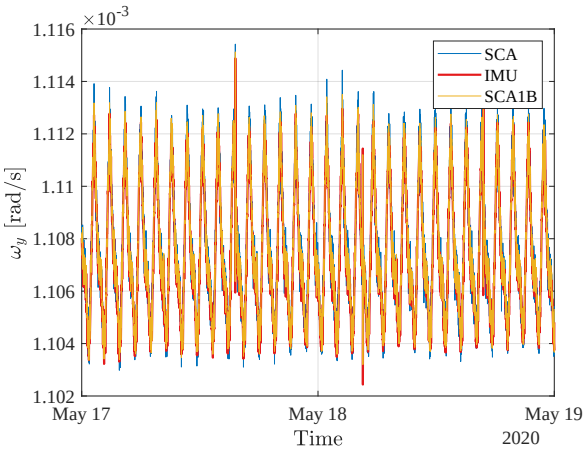

Figure 6.1: Long time series of the derived combined star camera, IMU and SCA1B angular rates around the *y* axis of the satellite frame for GRACE-FO C.

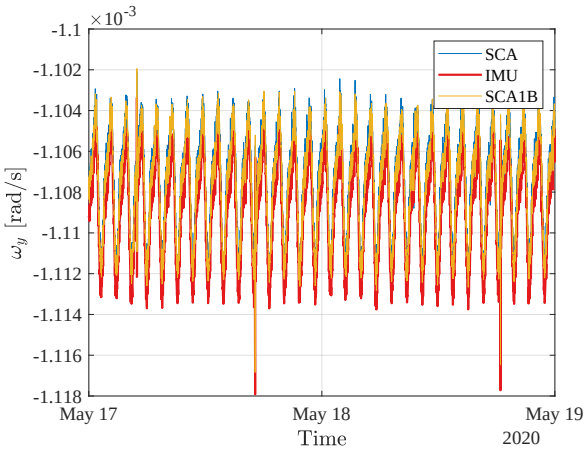

Figure 6.2: Long time series of the derived combined star camera, IMU and SCA1B angular rates around the *y* axis of the satellite frame for GRACE-FO D.

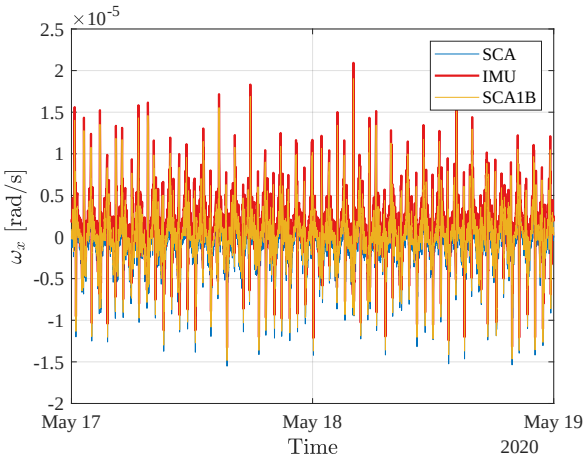

Figure 6.3: Long time series of the derived combined star camera, IMU and SCA1B angular rates around the *x* axis of the satellite frame for GRACE-FO C.

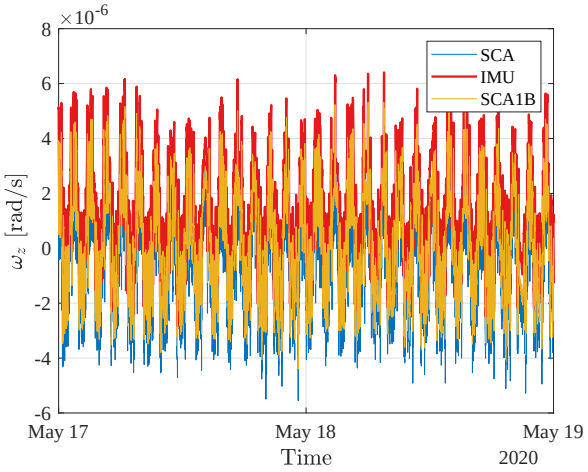

Figure 6.4: Long time series of the derived combined star camera, IMU and SCA1B angular rates around the *z* axis of the satellite frame for GRACE-FO C.

To increase the confidence of the calculations, a closer examination is performed for a smaller time window, for example over the course of one or two satellite orbits. Although, each sensor has a different measurement principle, it is expected that all of them detect the same variations in attitude and thus the angular rates shall exhibit similar behavior over time. The agreement between the sensors becomes more apparent in the presence of a satellite attitude maneuver, when the variations of the angular rates are much larger. In Figure 6.5 the angular rates around each axis of the SF are presented for the combined star cameras, the IMU and SCA1B during the 20th of October in 2020, when GRACE-FO C underwent a series of center-of-mass calibration maneuvers. During this operation, a satellite performs small periodic rotations around only one axis at a time, while the oscillations about the other two axes are kept to a minimum [Wegener et al., 2020]. According to Landerer, Flechter, et al. [2020], among several manuevers, the following three were commanded for GRACE-FO C on the 20th of October: a roll maneuver that started at 11:09:00 and ended at 11:12:00, a pitch manuever that started at 14:18:00 and ended at 14:21:00 and a yaw manuever that started at 21:57:00 and ended at 22:00:00. In fact, the angular rates of Figure 6.5 demonstrate these rapid fluctuations at those time intervals. Especially the IMU, that is more accurate at high frequencies, can clearly distinguish these oscillations. Furthermore, it is evident that even though the instruments have different noise and error characteristics as well as angular rate derivation algorithms, their output match very well during and around the maneuvers.

Equivalently to the comparisons performed above, the derived angular rates of each instrument are analysed in the frequency domain. This approach provides another perspective on the similarities of their signals. After evaluating the amplitude spectral density (ASD) of each signal, an inspection is performed in the fre-

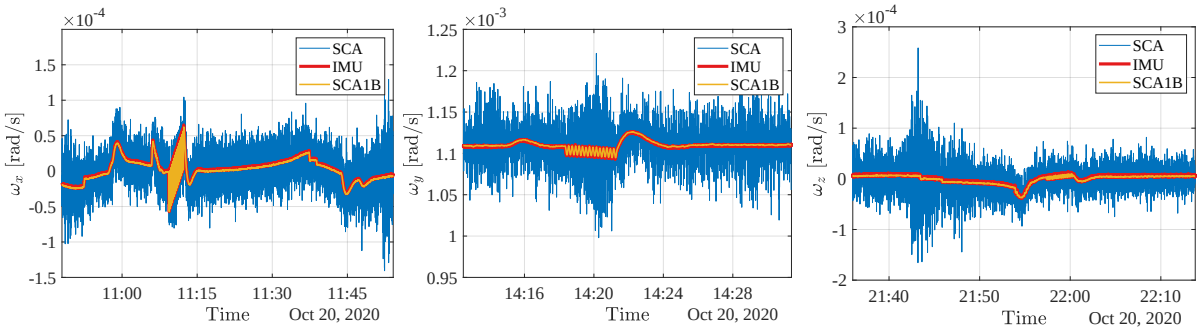

(a) x axis. (b) y axis. (c) z axis.

Figure 6.5: The roll, pitch and yaw angular rates derived from the combined star camera, IMU and SCA1B measurements during the center-of-mass calibration maneuvers on 20$^{\text{th}}$ of October 2020 for GRACE-FO C.

quency spectrum to check their agreement. As already mentioned, all sensors are expected to measure the same attitude variations and this should be noticeable both in the time and in the frequency domain. In Figure 6.6 the ASD of the angular rates for the combined star cameras, the IMU and the SCA1B data product for GRACE-FO C are illustrated. They have been determined over the period of May 17$^{\text{th}}$-21$^{\text{st}}$ 2020 and the black vertical dotted line represents the frequency of one cycle per revolution (1 cpr $\approx \frac{1}{94.5*60} \approx 1.76e-4$ Hz). As expected both instruments agree quite well at 1 cpr and from low frequencies up until 4-7 mHz. In addition, the star cameras exhibit a high frequency noise above 10 mHz. This is as expected since at the level of angles and at high frequencies, they have a flat noise spectrum, which after the differentiation of quaternions translates to noise that increases proportional to the frequency. Likewise, the differentiation of IMU angle measurements, which have a $1/f$ noise type of behavior, leads to a flat plateau at the level of angular rates.

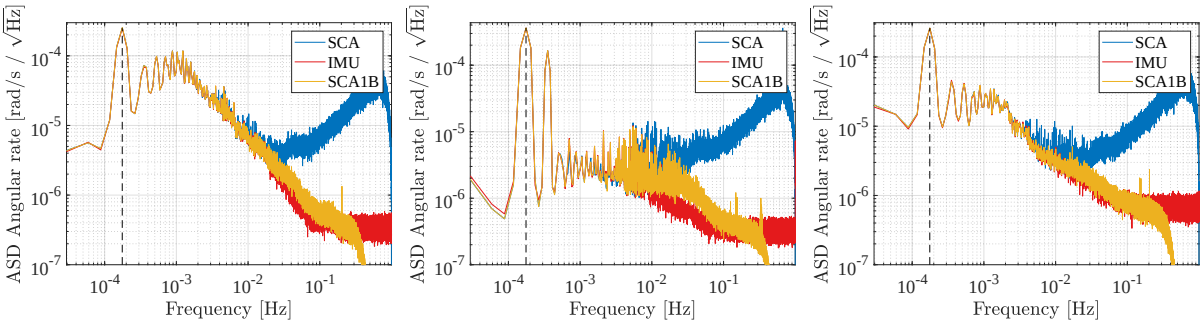

(a) x-component. (b) y-component. (c) z-component.

Figure 6.6: One-sided amplitude spectral density of the combined star camera, IMU, and SCA1B angular rates, evaluated over the period May 17$^{\text{th}}$ to 21$^{\text{st}}$ in 2020 for GRACE-FO C.

6.2. Inter-satellite pointing angles

Regarding the derivation of inter-satellite pointing angles from star camera quaternions, it can simply be validated by comparing the results of the calculations with the pitch and yaw angles measured directly by the laser ranging interferometer's steering mirrors. As it can be seen from Figure 6.7 and Figure 6.8, despite the different noise characteristics of the two instruments, the pointing angles derived from the star camera quaternions match very well the behavior of the steering mirror measured angles. Therefore, the derivation process, described in Section 4.1, was implemented correctly. It should be noted that prior to the comparison, the star camera data is transformed to the reference frame of the steering mirrors.

6.3. Optimal combination of quaternions

The algorithm for the optimal combination of star camera quaternions presented in Section 5.1.1 has been obtained from Siemes et al. [2018], who have already verified its implementation for the GOCE mission. To ensure that the algorithm is adopted correctly with GRACE-FO input parameters as well, the angular rates

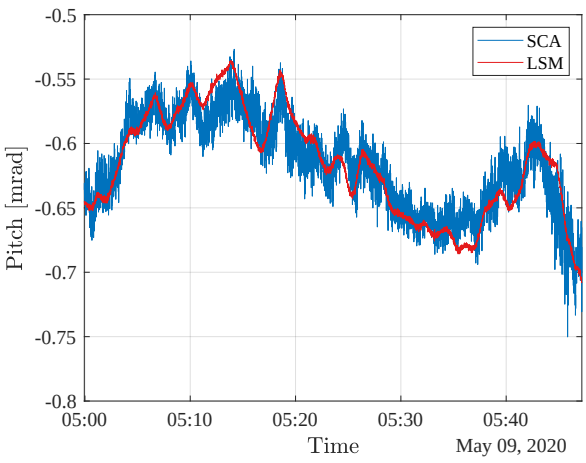

Figure 6.7: Time series of the measured steering mirror pitch pointing angles and the ones derived from combined star camera quaternions for GRACE-FO C.

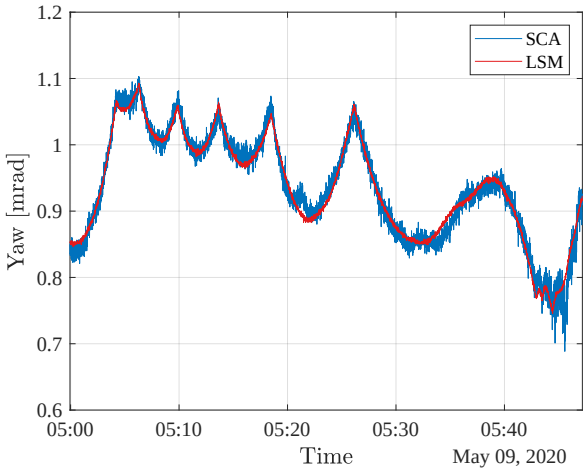

Figure 6.8: Time series of the measured steering mirror yaw pointing angles and the ones derived from combined star camera quaternions for GRACE-FO C.

resulting from the optimal quaternions are compared to those from the other sensors and from the official data product in the time and frequency domain. This comparison has already been illustrated with Figures 6.1 to 6.6. Additionally, in Section 7.1.1, the residuals from the combination have been analysed and displayed a behavior that is in agreement with the expectation from the star camera performance specifications.

6.4. Angular rate & attitude reconstruction

As with the optimal combination of quaternions, the angular rate and attitude reconstruction algorithms have already been verified and validated for the GOCE mission. Nevertheless, to ensure that they are used correctly within this MSc thesis, an additional verification is necessary to be performed locally. This is achieved by using star camera and gradiometer GOCE data as inputs to these algorithms and then comparing their results to the required output that has been provided by Christian Siemes, TU Delft [personal communication]. In Figure 6.9, the one-sided ASD of the desired and the actual angular rates produced with the angular rate reconstruction method, are depicted. From their differences it is clear that the same results can be achieved locally as with the ones already obtained for GOCE.

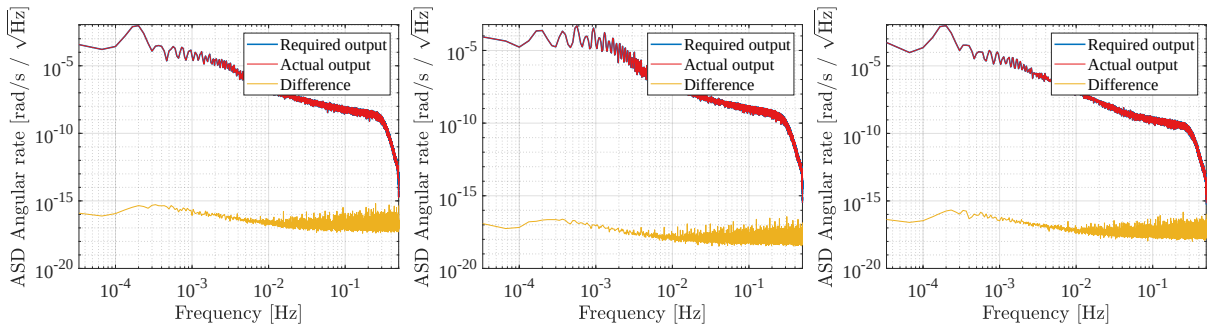

(a) x-component. (b) y-component. (c) z-component.

Figure 6.9: One-sided amplitude spectral density of the required and the actual output of the angular rate reconstruction algorithm using GOCE data.

In the same manner, the quaternions computed locally with the attitude reconstruction algorithm are compared to the required ones. In Figure 6.10, the quaternion residuals between the two previously-mentioned datasets are plotted, from which it is clear that equivalent results can be obtained.

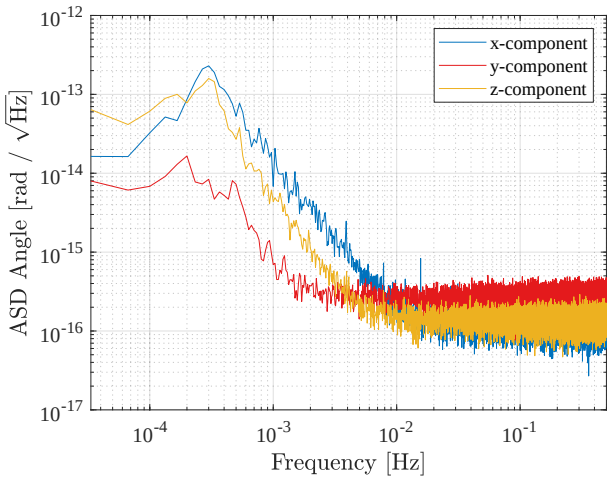

Figure 6.10: One-sided amplitude spectral density of the quaternion residuals between the required and the actual output of the attitude reconstruction algorithm using GOCE data.

7
Results

In this part of the report, the results from the various processing algorithms and the sensor data fusion approaches will be discussed. In Section 7.1, the error and noise assessment of each of the four instruments is presented and then in Section 7.2 the results of the sensors data calibrations is given. Next, in Section 7.3, the outcome of the optimal combination of quaternions is examined, while in Section 7.4 and Section 7.5 follow respectively the results from the angular rate and attitude reconstruction process. Finally, in Section 7.6 the impact of the proposed attitude reconstruction method on the GRACE-FO mission is investigated and a reflection is provided for future gravity missions. It should be mentioned that the analyses performed in this work have been limited to only one month of data. More specifically, the month of May in 2020 was chosen, for which all instruments could provide nominal measurements.

7.1. Sensor error & noise assessment

This section is devoted to assessing the errors and the noise in the star camera (Section 7.1.1), gyroscope (Section 7.1.2), steering mirror (Section 7.1.3) and accelerometer (Section 7.1.4) measurements.

7.1.1. Star cameras

As already mentioned in Section 2.3.1, the star camera measurement accuracy is limited by several factors, such as optical, centroiding and FoV errors, but also due to the camera construction geometry, the measurements are characterized by anisotropic noise. This means that the accuracy about the cross-boresight axes (x_{SCF} and y_{SCF}) of the camera is usually around 6 to 16 times better than the one about the boresight or roll (z_{SCF}) axis [Liebe, 2002]. Based on the μASC specifications, the nominal measurement accuracy about the former axes is expected to be around 2 arcseconds, which is equal to approximately 9.7 μrad [Jørgensen et al., 2012]. Thus, the corresponding accuracy about the boresight axis could fluctuate between 58 and 155 μrad.

Although, the in-flight measurement accuracy of the star cameras might not be possible to obtain precisely, its noise component can be approximated with the variable $\boldsymbol{e}_i$ (see Equation (5.2)), which is estimated during the optimal combination of quaternions. The vector $\boldsymbol{e}_i$ is composed of three small angles that correspond to the error and noise about the x, y and z components of the i^{th} star camera quaternions resolved in the i^{th} SCF. At lower frequencies, this vector is expected to mainly describe systematic errors, e.g. FoV errors, while at higher frequencies the random noise in the measurements. Upon inspection, it was found that above 0.1 Hz the PSD of $\boldsymbol{e}_i$ exhibits a flat plateau that indicates the white noise in the data. Therefore, the noise floor is calculated as the root mean squared (RMS) PSD level in the frequency band above 0.1 Hz. It should be noted that the $\boldsymbol{e}_i$ estimated during the combination of star camera and steering mirror quaternions have been used for this characterization. In Table 7.1 the monthly RMS values of the estimated random noise in the star camera quaternions is presented and in Figure 7.1 the daily RMS values are shown.

Table 7.1: The monthly RMS values of the random noise in the x, y and z component of the star camera quaternions, estimated over the month of May in 2020.

	GRACE-FO C			**GRACE-FO D**		
	SCA1	**SCA2**	**SCA3**	**SCA1**	**SCA2**	**SCA3**
$e_{i,x}$ [μrad]	11.09	15.7	12.4	8.7	10.4	10.1
$e_{i,y}$ [μrad]	10.4	16.2	13.2	8.2	11.5	12.5
$e_{i,z}$ [μrad]	112.8	204.5	137.7	105.8	129.6	130.6

In general, the star cameras on-board GRACE-FO D are performing better compared to GRACE-FO C, still for both satellites the estimated noise floors are close to the specifications. Additionally, star camera 1 measurements are the least noisy compared to the ones of the other cameras and especially for GRACE-FO D they

perform 12% better than specified. As it will be soon in the next paragraphs, a possible explanation for this behavior could be the number of stars in the FoV of that camera. The most degraded performance among all cameras can be seen for the second one of GRACE-FO C. As it will be demonstrated later on, this behavior could be explained from the unexpectedly decreased availability of that camera over the month of May. Based on the values of Table 7.1, the noise level ratio between the boresight and the roll about the boresight pointing for SCA1, SCA2 and SCA3 is computed to be 11, 13 and 11 respectively for GRACE-FO C and 12 for all cameras of GRACE-FO D. Last but not least, by inspection of Figure 7.1 it becomes apparent that despite the fact that the star cameras have a presumed identical performance, in-flight they display a small variability over the duration of one month. For example, the sensitivity of the star camera measurement accuracy to the moonlight intrusions can be seen with a decrease in performance, during the 9-10$^{\text{th}}$ of May.

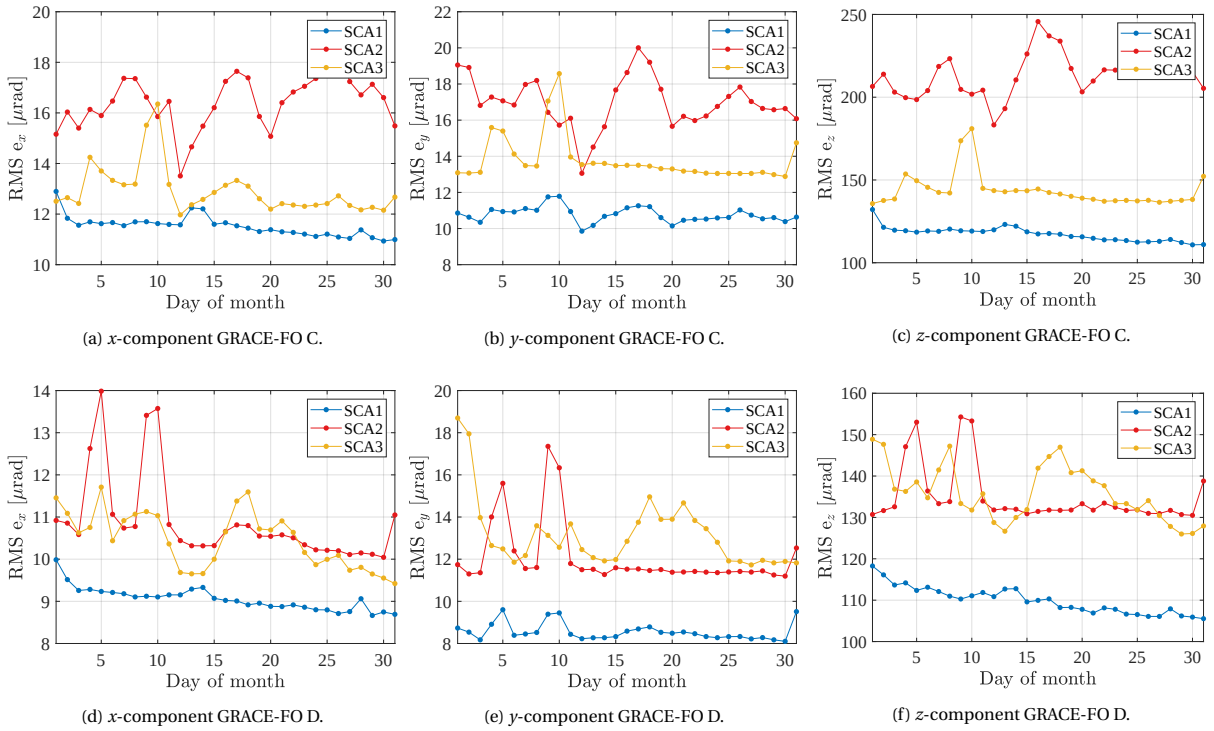

(a) x-component GRACE-FO C. (b) y-component GRACE-FO C. (c) z-component GRACE-FO C.

(d) x-component GRACE-FO D. (e) y-component GRACE-FO D. (f) z-component GRACE-FO D.

Figure 7.1: Daily RMS values of the random noise in the x, y and z component of the star camera quaternions, estimated over the month of May in 2020.

Another important factor that can influence the measurement accuracy of the star cameras, is the number of stars in their FoV. In other words, the higher the number of identified bright stars in the digital image, the better the estimated satellite attitude of a star camera. Equally important, since the distribution of stars in the sky is not uniform, it is crucial where a camera is pointing. Depending on the latter, a camera could end up being blinded by the Sun or the Moon. In Figure 7.2, the number of stars in the star camera FoV of all six cameras is shown in an argument of latitude versus time plot. The white-covered areas represent instances where the camera is blinded either by the Sun or the Moon. Specifically, the long diagonal white band that can be seen in star camera 2 of GRACE-FO C and camera 3 of GRACE-FO D indicates sunlight intrusion. On the other hand, the smaller white spots, some of which are better visualized for SCA3 and SCA2 of GRACE-FO C and D, respectively, represent blinding from the Moon.

Based on the layout of the GRACE-FO satellites, it is known that star camera 1, 2 and 3 point respectively, more or less, to the negative z, the positive y and the negative y axis of the SF. And since while in orbit, one satellite is a rotated version of the other one around the latter's z-axis, star camera 1, 2 and 3 of GRACE-FO C and star camera 1, 3 and 2 for GRACE-FO D respectively point to a similar part of the sky with a small delay. Thus, comparable patterns can be seen in the geographic plots. A closer inspection on Figure 7.2c and Figure 7.2f, and in particular the upper limit of the long diagonal white band reveals a higher number of invalid data for SCA2 of GRACE-FO C despite the two cameras having a similar inertial orientation. The exact reason for this phenomenon has not been found yet, however, one of the hypotheses is that due to the relative orientation with the Sun, more stray light from the Sun might reach the camera's FoV. At the same time, this behavior could justify the overall decrease in the performance of that camera that was observed in Table 7.1. Finally, the

comparison of the SCA1 plots of both satellites to the ones of the other cameras, could explain their increased measurement accuracy, because of their higher amount of valid data and the higher average number of stars detected.

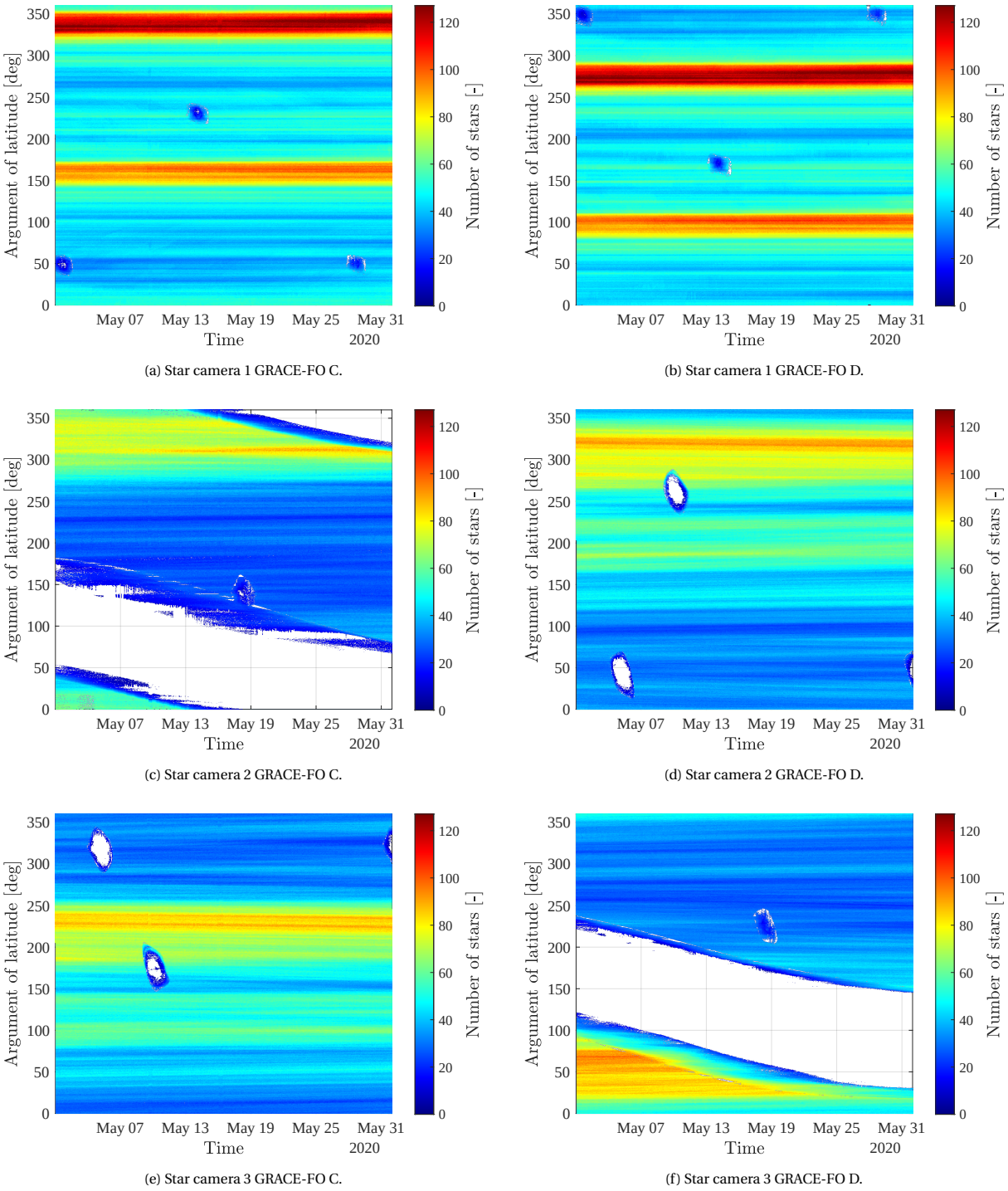

(a) Star camera 1 GRACE-FO C.

(b) Star camera 1 GRACE-FO D.

(c) Star camera 2 GRACE-FO C.

(d) Star camera 2 GRACE-FO D.

(e) Star camera 3 GRACE-FO C.

(f) Star camera 3 GRACE-FO D.

Figure 7.2: Number of stars in the FoV of the GRACE-FO C and D star cameras for the month of May in 2020.

Additionally, as indicated by Harvey [2016] star cameras are prone to FoV errors. This is explained from the fact that their derived attitude estimate depends on the stars in their FoV, thus errors would repeat when the same stars are viewed at the same lens locations. In fact, when examining Figure 7.2, it is clear that over the period of several days the stars viewed from the cameras on-board the GRACE-FO satellites do not change considerably at same locations along the orbit. Instead of calculating a residual inter-camera quaternion, as performed by Harvey [2016], a comparison between the star camera and the steering mirror derived quater-

nions is made to identify these errors. This is possible, because the measurement principle of the steering mirror does not depend on the identification of stars using a digital camera. As an example, Figure 7.3 depicts the *y*-component of the quaternion difference between all three cameras and the steering mirrors of GRACE-FO D, as a function of argument of latitude and time. Note that their differences have been lowpass filtered so that the white noise of the quaternions in the high frequencies is removed. As expected, distinct differences are observed that repeat for several days along constant arguments of latitude. Similar behavior is exhibited for GRACE-FO C as well.

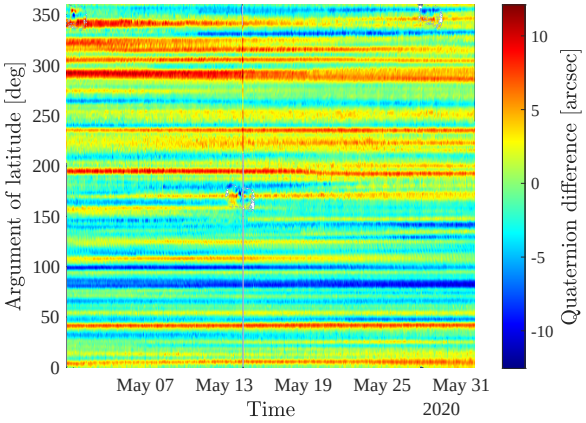

(a) Star camera 1.

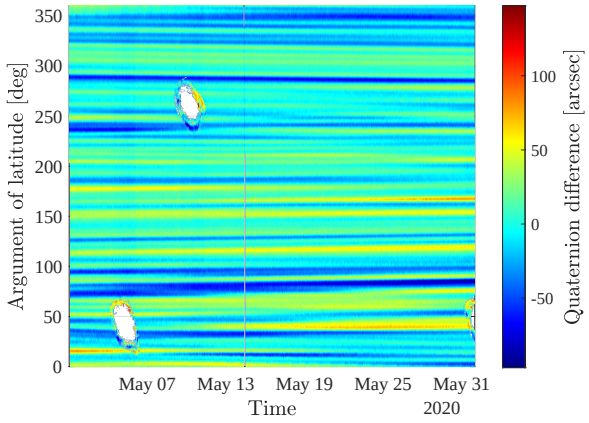

(b) Star camera 2.

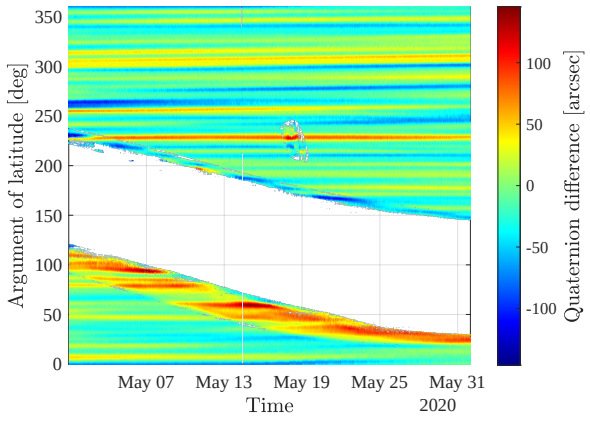

(c) Star camera 3.

Figure 7.3: The *y*-component of the star camera and steering mirror quaternion residuals as a function of time and argument of latitude, for GRACE-FO D.

Last but not least, it should be mentioned that thermo-elastic effects in the support structure of the satellite can influence the performance of the star cameras and possibly cause systematic effects and biases. Due to the lessons learned from GRACE and the Swarm satellites many improvements have been incorporated to GRACE-FO that minimize the exposure of the cameras to extreme temperatures [Kornfeld et al., 2019]. A dedicated analysis on long time scales would be of interest to understand how temperature variations can affect the GRACE-FO star camera performance. However, due to time constraints of this thesis such analysis could not be performed, but is recommended for further research.

7.1.2. IMU

Based on the Astrix 120 specifications, the inertial measurement unit has only one main noise contributor, which is the angle random walk (ARW) [Airbus Defense and Space, 2020]. Besides that, the IMU measurements are prone to systematic errors such as constant biases, scale factors and misalignment errors. The ARW has a magnitude of about $0.0016\,^\circ/\sqrt{\text{hr}}$ which corresponds to an equivalent

$$\text{ARW} = 0.0016\frac{^\circ}{\sqrt{\text{hr}}} = 0.0016\cdot\frac{\pi}{180}\cdot\frac{1}{60}\frac{\text{rad}}{\sqrt{\text{s}}} \approx 4.65\cdot10^{-7}\frac{\text{rad}\sqrt{\text{s}}}{\text{s}} \approx 0.465\frac{\frac{\mu\text{rad}}{\text{s}}}{\sqrt{\text{Hz}}} \tag{7.1}$$

In Figure 7.4, the one-sided ASD of the derived angular rates from each gyroscope of the IMU are shown. The purple line represents a white noise signal that corresponds to the angle random walk of the specifications. It can be clearly observed that for both satellites the IMU measurements are dominated at high frequencies, starting from around 60 mHz and onwards, by the designated noise. In fact, the measurements of the angular rates of all gyros exhibit around an 11% lower noise floor than specified. The systematic errors mentioned above have an effect on the very low frequencies, close to the DC frequency and cannot be seen in this figure. However, by comparing lowpass filtered IMU angular rates to the ones calculated from star camera quaternions, constant biases can be observed in the order of a few μrad. Finally, in Figure 7.4 several narrow spikes can be seen at frequencies above 1 Hz. These are artifacts in the measurements and amount to systematic errors that could be related to the operation of another instrument or process inside the satellite, such as the AOCS.

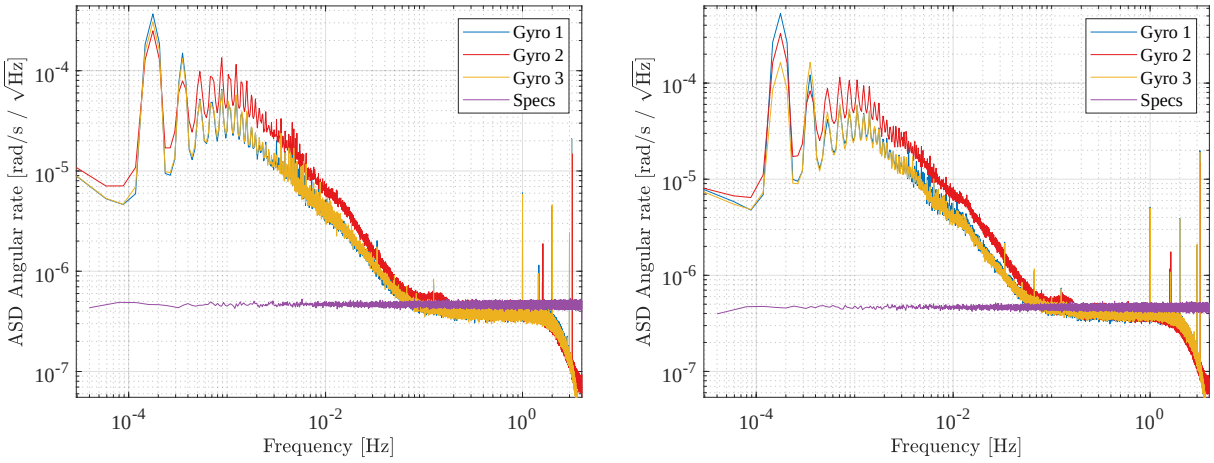

(a) GRACE-FO C.

(b) GRACE-FO D.

Figure 7.4: Comparison of the angular rates derived from measurements of each gyroscope with the angle random walk specification of the IMU, in an ASD plot.

7.1.3. LSM

As far as the steering mirrors is concerned, Wegener et al. [2020] have mentioned that the resolution of the measured pitch and yaw angles is limited at high frequencies by quantization noise of about 1 μrad/$\sqrt{\text{Hz}}$, which translates to an equivalent of 0.2 arcseconds/$\sqrt{\text{Hz}}$. In the meantime, Goswami et al. [2021] pointed out that the white noise in the measurements is due to the broadband noise of the Position Sensing System (PSS) sensor, which is approximately 3 times larger than the quantization noise. In Figure 7.5, the one-sided ASD of the measured pointing angles is shown for both satellites. As it can be observed, at frequencies above 60 mHz, the measurements are limited by noise. In particular, the pitch and yaw angles have respectively a noise floor equal to 1.3 and 1.8 μrad/$\sqrt{\text{Hz}}$ or 0.27 and 0.37 arcseconds/$\sqrt{\text{Hz}}$.

Based on the above computed values, it is clear that the steering mirror measurements have about a 10 times better accuracy than those of the star cameras. This information can be valuable during the optimal quaternion combination of these two different datasets. To be able to achieve the latter, however, the corresponding steering mirror quaternions, that describe the rotation from the inertial to the SF, should be obtained. As introduced in Section 5.1.2, the fact that the steering mirrors do not capture the roll variations of the satellite imposes a limitation on the derivation of the aforementioned quaternions. Nevertheless, this obstacle can be addressed either by substituting the roll angles derived from star camera measurements or by disregarding them from the derivation. In Figure 7.6, the importance of roll data is illustrated. The residuals between the steering mirror and the optimally combined star camera quaternions are depicted when roll is excluded and when it is included in Equation (5.29). As it can be observed, roll does not seem to have any significant effect at the level of quaternions for the y and z components. This can be explained from the fact that the pointing angles have a magnitude in the order of a few hundred of arcseconds, so considering small angle approximations and disregarding it from Equation (5.29) does not affect how well the y and z axes of $\mathbf{R}_{\text{SF}\rightarrow\text{Inertial}}$ can be resolved. For the same reason, when the roll angles from star camera data are included, the y and z components of the derived quaternions are not influenced by star camera noise. Interestingly enough, when roll is not taken into account the x component of the quaternion residuals will be almost identical to the roll pointing

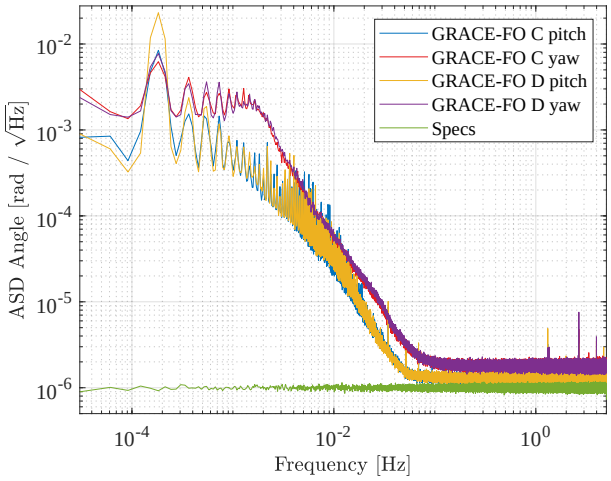

Figure 7.5: Comparison of the measured steering mirror pitch and yaw pointing angles' ASD with the specified quantization error.

angles derived from star camera data. It should be mentioned, however, that at the level of angular rates, roll information will have a more significant impact because all components of a quaternion are used to calculate the latter, as seen by Equation (B.11) and Equation (B.12). With this in mind, it can be said that the measured pitch and yaw steering mirror angles can be used, without the need of another sensor, to derive the y and z components of a quaternion that describes the rotation of the corresponding satellite axes to inertial space.

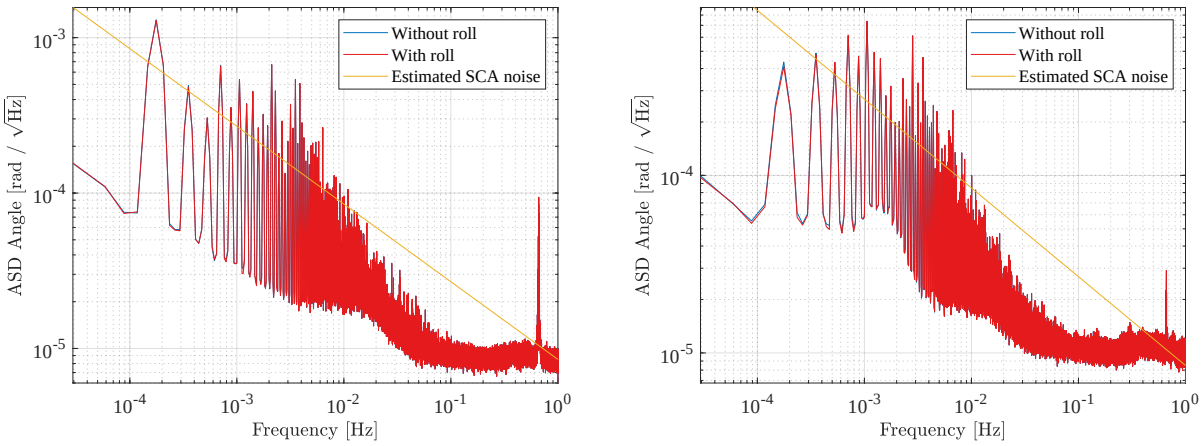

(a) y-component.

(b) z-component.

Figure 7.6: Comparison of the y and z components of the steering mirror and combined star camera quaternion residuals when the roll angles are included and when they are excluded during the derivation process of steering mirror quaternions.

Furthermore, in Figure 7.6, the ~2 arcsec high frequency noise of the star cameras can be seen at frequencies above 0.1 Hz as the flat plateau. Meanwhile, the spikes that begin from low frequencies and continue up until 10 mHz correspond mostly to the star camera FoV errors that were demonstrated earlier in Figure 7.3. By a closer inspection at those frequencies, however, it is clear that the flat noise spectrum of the high frequencies does not continue at the lower ones and a type of $1/f^n$ behavior is observed. This indicates that one of those instruments could be limited at those frequencies due to some random noise. According to Goswami et al. [2021] and to her personal communication with John Leif Jørgensen, the noise floor of star camera measured angles can be estimated with

$$\tilde{\theta}_{SCA}(f) = \frac{8.5}{\sqrt{f}} \; \frac{\mu\text{rad}}{\sqrt{\text{Hz}}} \tag{7.2}$$

which can explain the behavior noted above (depicted as the yellow line in Figure 7.6) and most probably denote that at those low frequencies the steering mirrors are more accurate. Finally, the quaternion differences revealed a misalignment between the two sensors with the presence of two constant biases. For this reason, prior to any data combination, it is essential to calibration them and bring them in the same reference frame.

7.1.4. Accelerometer

It is already known from McCullough et al. [2019] that the GRACE-FO accelerometers are affected by large spurious accelerations which produce phantom accelerations and exhibit an improper response at thruster firings. For this reason, it is necessary to remove these artifacts, before any comparison or combination is done with the other sensors, and reintroduce the proper thruster response to the accelerometer data. These calibration steps have already been implemented for the linear accelerations, but not for the angular ones. Thus, a thrust response model was developed, similar to the one for the linear accelerations, for which the attitude thruster firings are assumed to impact a constant acceleration over the duration of the firing. This constant value was determined from a series of long thruster firings that were performed on the 6$^{\text{th}}$ of February in 2019 for the calibration of the linear accelerations.

After removing the spurious accelerations and reintroducing the more accurate thruster responses, the angular rates of the accelerometer are derived using Equation (4.13). A comparison is then performed with the star cameras and the IMU in terms of their ASDs, shown in Figure 7.7. As expected the integration of the measured angular accelerations tilts the ASD of the accelerometer angular rates such that low-frequency noise is amplified and high-frequency noise is dampened.

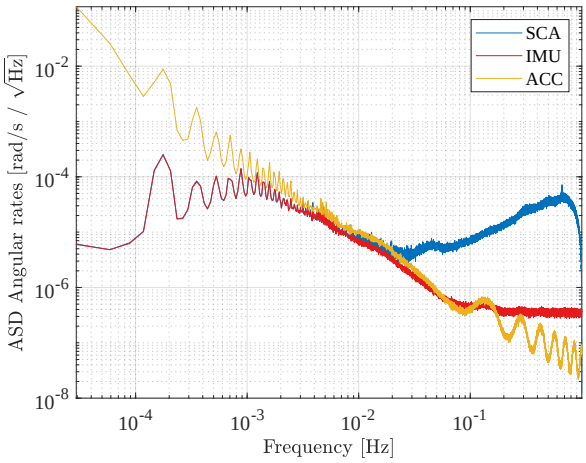

(a) x-component.

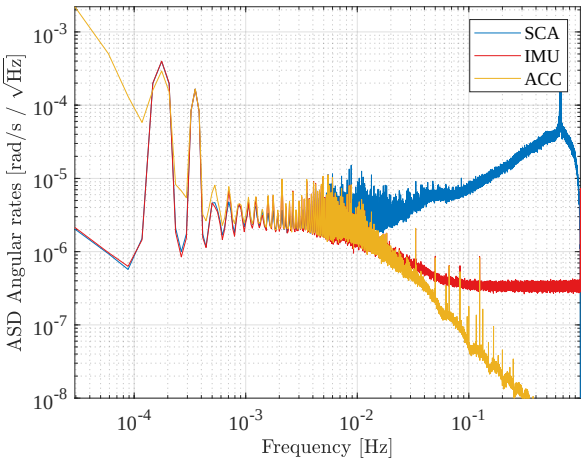

(b) y-component.

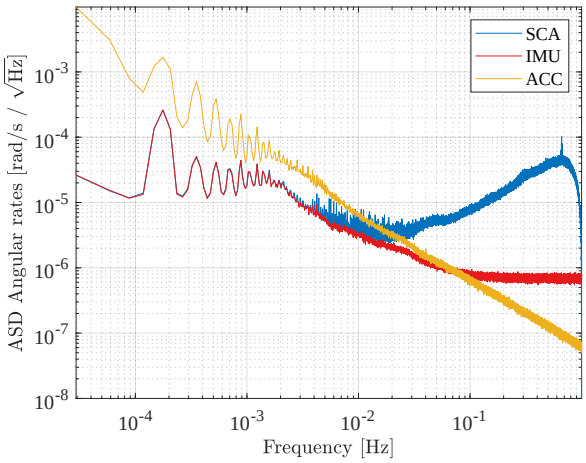

(c) z-component.

Figure 7.7: Comparison of the derived star camera, IMU and accelerometer angular rates' ASD for GRACE-FO C.

At first sight, the spectral densities indicate that the accelerometer could be useful in a data sensor fusion approach for high frequencies. By further inspecting the graphs, however, a rather large disagreement can be seen between the sensors between 1 and 10 mHz, most notably for the angular rates around the z and x axis of the SF. These differences do not only prevent a proper calibration of the data, but also suggest that additional error and noise sources remain in the angular acceleration data that are not accounted for. Due to time constraints, a definite explanation of this behavior was not found and it was decided to not use the

accelerometer any further for the attitude reconstruction. Further research is advised on the processing of accelerometer data, especially on the part of modelling the thruster responses.

7.2. Sensor data calibrations

This section is dedicated to the data calibration results of the star cameras, the gyroscopes and the steering mirrors. In Section 7.2.1, the estimated constant biases of the star cameras and the steering mirrors are presented and their effect on the IBAs is discussed. Next, in Section 7.2.2, the IMU calibration parameters are provided.

7.2.1. SCA & LSM data calibration

An important part of the star camera quaternions calibration process is the alignment of all cameras in the same reference frame. For GRACE-FO the QSA1B quaternions exist, which were estimated at the beginning of the mission and describe the rotation of the individual star camera quaternions to the SF. However, these calibration parameters could contain errors that do not lead to a perfect alignment of the cameras with each other in the SF. Comparing the IBAs observed by the star cameras in-flight with the ones determined by the preliminary knowledge of the cameras' orientation in the SF (i.e. the QSA1B quaternions), could reveal whether the initial knowledge of their relative orientation is affected by any systematic errors. Using Equation (4.14) to (4.19) and (4.22) the preliminary IBA values are calculated and presented in Table 7.2.

Table 7.2: IBAs computed based on the preliminary knowledge of the star cameras' orientation in the satellite frame.

	IBA$_{12}$	**IBA$_{13}$**	**IBA$_{23}$**
GRACE-FO C	80.9563°	80.1966°	100.062°
GRACE-FO D	79.7436°	79.7527°	98.6532°

Then, based on the values of the above table and Equation (4.24), the IBA differences are derived and visualized in Figure 7.8 for the month of May in 2020, before any correction is applied to the star camera data. It is clear that for both satellites, all IBA differences exhibit offsets. For IBA$_{12}$, IBA$_{13}$ and IBA$_{23}$ of GRACE-FO C these amount to approximately 40, 49 and 54 arcseconds respectively and for GRACE-FO D to 73, 45 and 69 arcseconds.

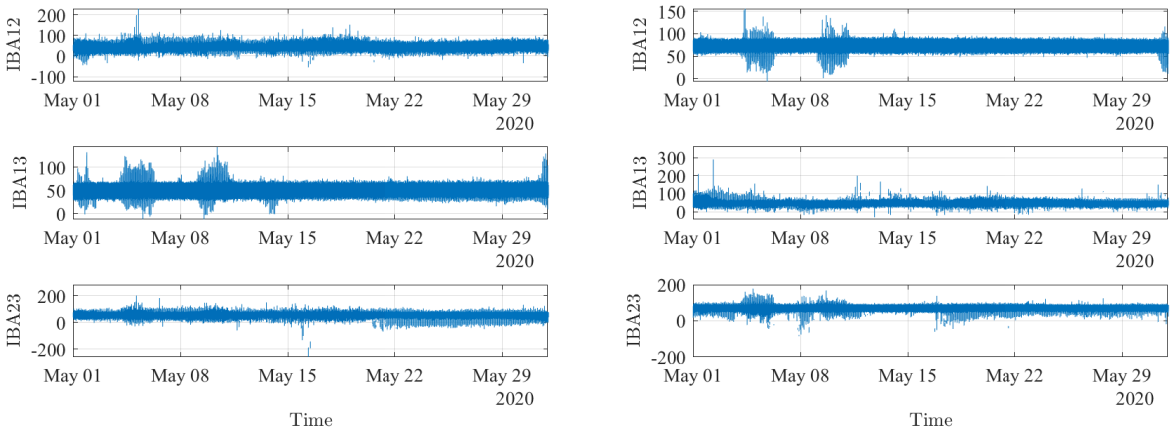

(a) GRACE-FO C.

(b) GRACE-FO D.

Figure 7.8: Differences between the preliminary IBAs and the ones observed in-flight during May in 2020, before applying the $\tilde{\mathbf{b}}_i$ corrections. Units of the y-axis are in arcseconds.

According to the method presented in Section 5.1.1, constant biases are estimated that can minimize the observed offsets and in fact, after applying this correction, the mean value of all IBA differences goes practically to zero. In Table 7.3, the offsets observed before and after the corrections are provided.

Given these corrections, the star camera quaternions can now be rotated in a common reference frame and their optimal combination can be performed. Nevertheless, it should be noted that this new frame does not guarantee perfect alignment with the true satellite axes. This is due to the fact that the individual star camera

Table 7.3: Mean value of the difference between the preliminary and the in-flight IBAs, before and after the two corrections. The presented values are in units of arcseconds.

	GRACE-FO C			GRACE-FO D		
	Before correction	**After correction (SCA only)**	**After correction (SCA+LSM)**	**Before correction**	**After correction (SCA only)**	**After correction (SCA+LSM)**
IBA$_{12}$	40.561	0.712	-1.140	73.434	-0.042	-1.653
IBA$_{13}$	49.365	0.015	-1.004	45.227	0.220	-1.419
IBA$_{23}$	54.881	0.487	-0.359	69.818	-0.035	0.519

biases are co-estimated relative to each other and any rotation that is mutual to all of them is undetermined. As a result, small offsets could still remain between the calibrated and the true body frame, which can translate to undesired inter-satellite pitch and yaw pointing biases and in turn affect the AOC [Bandikova, 2015; Horwath et al., 2011]. One way to mitigate the error arising from the common rotation of the cameras is to extract and use attitude information from another source, such as the LSM quaternions. According to Kornfeld et al. [2019], the ground rotation alignment requirements of the laser ranging interferometer's triple mirror assembly with respect to the accelerometer are stricter compared to the ones of the star cameras. Based on this, one could assume that the knowledge of the steering mirrors in the SF could be more accurate in comparison to the star cameras. Therefore, it was decided to extend the calibration procedure so that the quaternions of the former sensor can be included as well. The constant biases, that are determined in this way, correspond for GRACE-FO C to (units are in arcseconds)

$$\tilde{\mathbf{b}}_{1,C} = \begin{bmatrix} -130.29 \\ -244.92 \\ 106.43 \end{bmatrix}, \quad \tilde{\mathbf{b}}_{2,C} = \begin{bmatrix} -119.23 \\ -172.79 \\ 77.39 \end{bmatrix}, \quad \tilde{\mathbf{b}}_{3,C} = \begin{bmatrix} -176.34 \\ -219.48 \\ 97.60 \end{bmatrix} \quad \tilde{\mathbf{b}}_{LSM,C} = \begin{bmatrix} - \\ -114.58 \\ -104.95 \end{bmatrix} \tag{7.3}$$

and for GRACE-FO D to

$$\tilde{\mathbf{b}}_{1,D} = \begin{bmatrix} -0.367 \\ -35.34 \\ 23.57 \end{bmatrix}, \quad \tilde{\mathbf{b}}_{2,D} = \begin{bmatrix} 45.50 \\ 37.50 \\ 19.95 \end{bmatrix}, \quad \tilde{\mathbf{b}}_{3,D} = \begin{bmatrix} -15.28 \\ 41.23 \\ 56.84 \end{bmatrix} \quad \tilde{\mathbf{b}}_{LSM,D} = \begin{bmatrix} - \\ 140.95 \\ -131.40 \end{bmatrix} \tag{7.4}$$

According to this approach, the new offsets in the IBA differences, shown in Table 7.3, are also close to zero except for IBA$_{12}$ and IBA$_{13}$, which still exhibit offsets of around 1 arcsecond. Once again, due to the lack of a ground truth this method does not necessarily entail that the instruments are now more accurately aligned with the true satellite axes. However, based on the assumption that the orientation of the steering mirrors can be determined better due to the stringent alignment requirements, it was decided to use the latter for the calibration of the two instruments. Due to time constraints it was not possible, but it would be of great value to investigate the in-flight stability of their orientations with respect to the SF at long timescales.

7.2.2. IMU data calibration

As mentioned in Section 5.2.2, star camera measurements are used to calibrate the IMU data. To perform an accurate calibration, it is essential to only use data that are not affected by the main noise contributors of the two sensors. This is achieved with an inspection in the frequency domain of the angular rates, derived at the individual gyro frame, and the identification of the frequency, above which the ASDs of the two instruments do not match anymore. Afterwards, lowpass filtering is applied to the observation equations and the design matrix of Equation (5.49). The cut-off frequency chosen for the calibration of the IMU data is 7 mHz. In fact, this value agrees well with the frequency where the noise PSDs of the two instruments based on their specifications cross each other.

Table 7.4 provides the estimated IMU calibration parameters for both satellites. The order of magnitude of these values is representative for a typical calibration of IMU data [Pittelkau, 2005]. By applying these parameters during the derivation of IMU angular rates, any systematic errors in the measurements are now minimized and the IMU is aligned with the star cameras. Both instruments are ready to be used now for the angular rate reconstruction.

Table 7.4: Estimated calibration parameters for the IMU data.

	GRACE-FO C			GRACE-FO D		
Parameter	**Gyro 1**	**Gyro 2**	**Gyro 3**	**Gyro 1**	**Gyro 2**	**Gyro 3**
D_i (misalignment) [arcsec]	707.7	1389.0	1205.7	155.8	516.0	292.4
E_i (misalignment) [arcsec]	-691.9	466.2	1415.2	2988.6	3429.5	-548.9
Δk_i (scale factor) [-]	-6.76e-3	-4.83e-3	9.71e-4	-1.04e-2	-1.25e-2	2.18e-3
b_i (bias) [arcsec/s]	1.49	-1.24	1.00	-1.44	0.32	-0.35

7.3. Optimal combination of quaternions

With a successful calibration of star camera and steering mirror data, an optimal combination of quaternions can now be achieved. As described in Section 5.1, two combination cases are performed within this MSc thesis, namely one that considers only star camera measurements (case 1) and a second one that also includes steering mirror data (case 2). Their performance is firstly evaluated in terms of computed angular rates and then in terms of quaternions. Since the results between the two satellites are similar, the discussion in the section focusses on just GRACE-FO D.

In Figure 7.9, the ASDs of the satellite angular rates derived from these two cases, the official attitude solution and the IMU data for GRACE-FO D are shown. As illustrated from the figure, all angular rate components of case 1 (blue lines) exhibit high-frequency noise proportional to the frequency, indicated by the dashed black line. This originates from the differentiation of the combined star sensor quaternions, which showcase a white

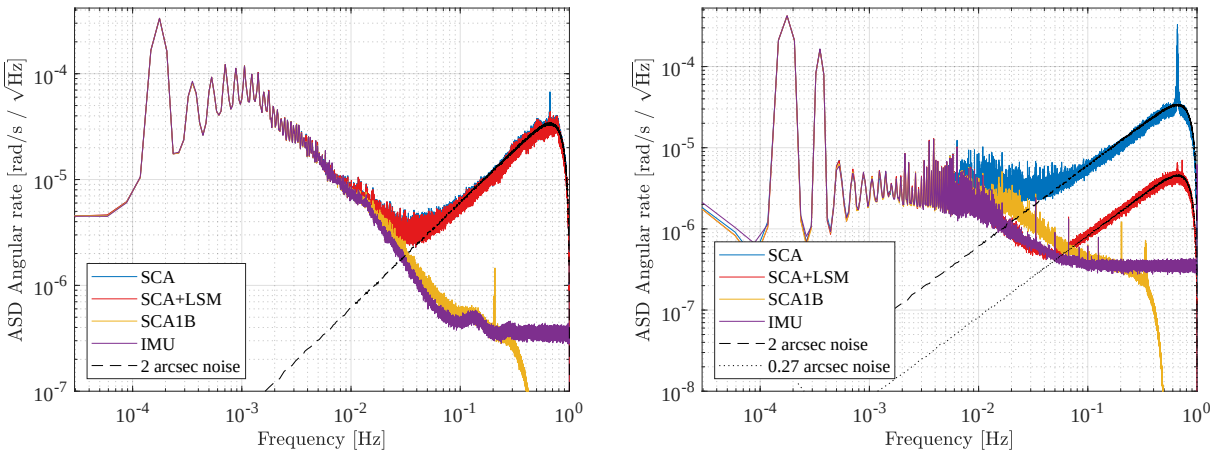

(a) *x*-component.

(b) *y*-component.

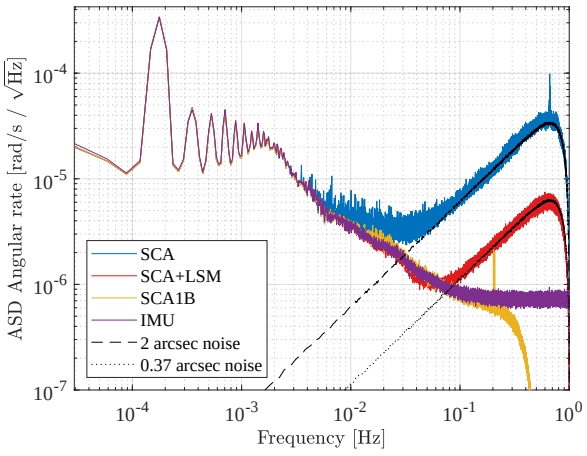

(c) *z*-component.

Figure 7.9: Comparison of the angular rates' ASD derived from the two optimally combined quaternion cases, the official data product and the IMU for GRACE-FO D.

noise with a standard deviation of 2 arcseconds. In other words, the optimal quaternions manage to effectively take into account the anisotropic accuracy in all cameras and provide a more accurate satellite attitude than what could be achieved with just one camera (cf. Table 7.1). When steering mirror quaternions are also considered in the combination (red lines) the same behavior is displayed, but now it occurs at a higher frequency due to their higher accuracy, which was demonstrated in Section 7.1.3. Needless to say, since no information is contained in the x component of the steering mirror quaternions, the corresponding component of the angular rates is the same for both combination cases. Additionally, from Figure 7.9b and 7.9c, it becomes apparent that not only the IMU (purple line), but also case 2 can already provide improved results compared to the official attitude quaternion product, labeled hereafter SCA1B (yellow line), at the frequency range between 10 and 60 mHz. At higher frequencies, the even lower noise of IMU data can be exploited with the angular rate and attitude reconstruction algorithms as it will be shown in the next sections. Lastly, it should be noted that the drop in the yellow curves, observed above 0.2 Hz, indicates the lowpass filter that has been applied to the data as a means to reduce the sample rate to 1 Hz.

To further analyse the derived optimal quaternions, a comparison is performed in the frequency domain between the quaternions of the two cases and those of the SCA1B data product. In Figure 7.10, the x, y and z components of the quaternion residuals are depicted in an ASD plot. From these sub-figures, it is clear that the y and z components of case 2 quaternions are not only closer to SCA1B above 20 mHz, but also they exhibit far smaller differences at multiples of the orbital frequency compared to case 1. Additionally, the same increase of

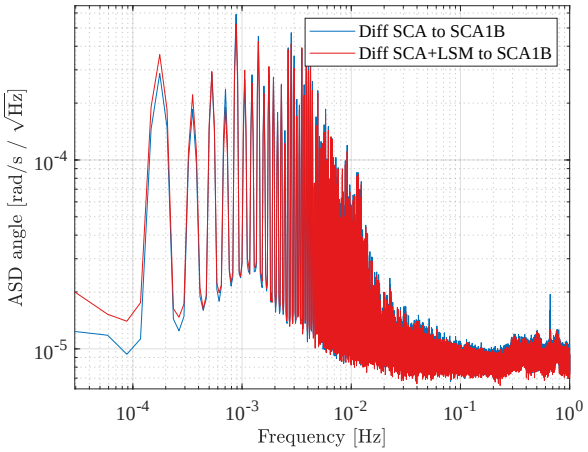

(a) x-component.

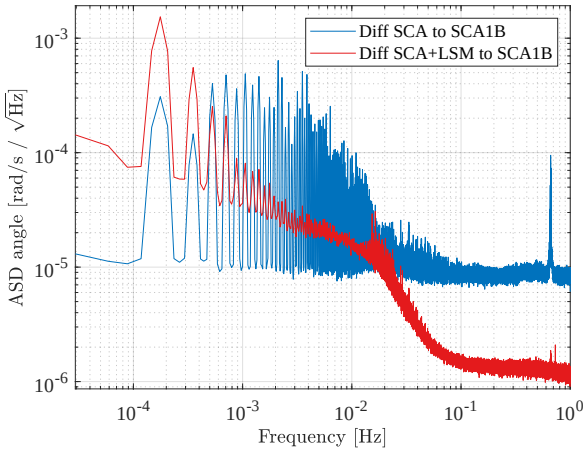

(b) y-component.

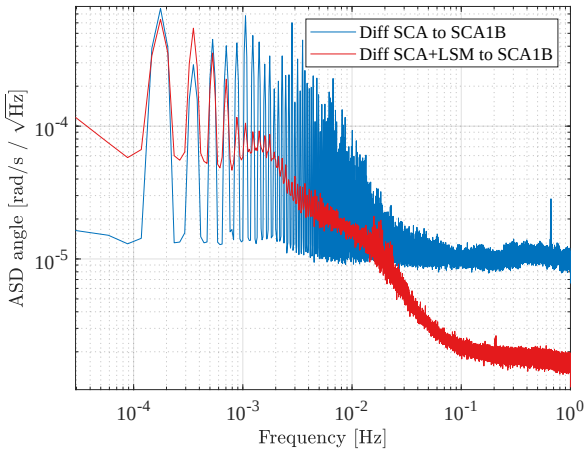

(c) z-component.

Figure 7.10: Comparison of the quaternion residuals' ASD between the SCA1B and the two optimally combined quaternion cases, for GRACE-FO D.

the ASD towards lower frequencies is observed as it was noted in Figure 7.6. This behavior denotes that these components of the case 2 quaternions are predominately based on steering mirror data. Therefore, the larger differences in case 1 are expected to arise from FoV errors in the star camera measurements. To understand

the nature of this discrepancy, the calculated quaternion residuals are examined in a geographic plot.

Figure 7.11a visualizes the *y* component of the quaternion differences between case 1 and SCA1B in an argument of latitude versus time plot. Using this representation, it is evident that between the two sets of quaternions horizontal stripes that span at constant arguments of latitude exist as well as a type of daily averaging. In fact, it is known from Harvey and Sakumura [2019] that within the star camera error model of the Kalman filter setup, a daily constant term, that describes the deviation of a camera's attitude from a nominal set value, was included as well as a term to account for FoV-dependent errors. At the same time, when inspecting the quaternion differences between case 1 and the steering mirrors, shown in Figure 7.11b, similar features can be observed as the ones in Figure 7.11a. As explained in Section 7.1.1, the steering mirrors cannot be affected by FoV errors, therefore, it can be concluded that latter are the main reason for the discrepancies between the two quaternion combination cases. Having said that, it is obvious that incorporating steering mirror measurements in the attitude reconstruction process of GRACE-FO would be of much benefit for the final attitude solution.

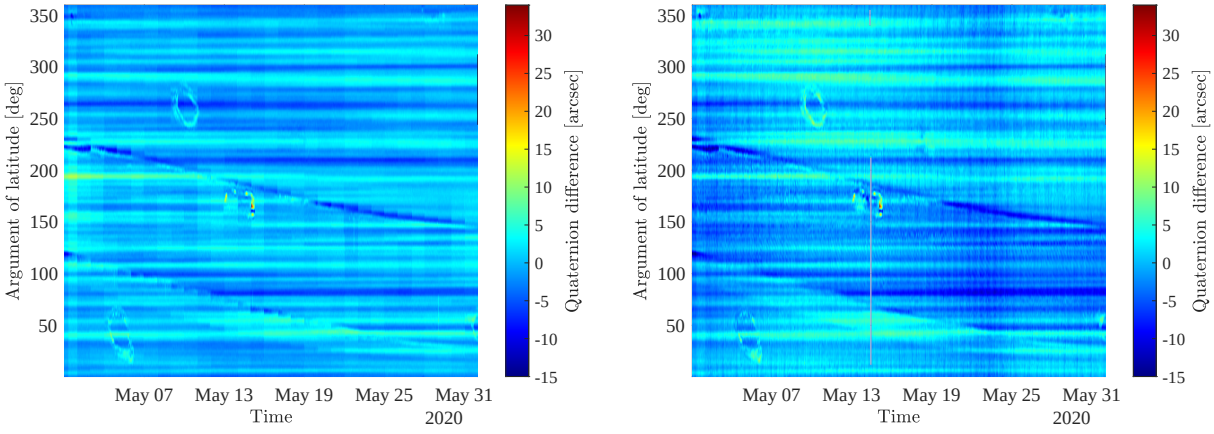

(a) Difference between SCA1B and optimally combined star camera quaternions.

(b) Difference between steering mirror and optimally combined star camera quaternions.

Figure 7.11: Argument of latitude versus time plot of the *y*-component of the quaternion differences between (a) the SCA1B and the optimally combined case 1 quaternions and (b) the steering mirror and the optimally combined case 1 quaternions, for GRACE-FO D.

7.4. Angular rate reconstruction

Within this research, the angular rate reconstruction algorithm is applied for two different cases. For the first one, which is also called the nominal case, the angular rates are reconstructed from IMU and combined star camera data. For the second case, steering mirror and star camera data are optimally combined at the quaternion level before their derived angular rates are reconstructed with the IMU ones. What differentiates these two cases, is the crossing frequency for the *y* and *z* component of the angular rates, which is around 10 times higher for the second case due to the higher accuracy of the steering mirrors. In general, these crossing frequencies can be determined purely from the noise characteristics of each instrument as the point where the two noise curves cross each other in a PSD plot. Table 7.5 presents the values of the frequencies that were used for both satellites within this MSc thesis.

Table 7.5: Crossing frequencies for the two angular rate reconstruction (ARR) cases.

	ARR 1: IMU + SCA	**ARR 2:** IMU + (SCA+LSM)
Component	**Frequency** [mHz]	
x	7.0	7.0
y	5.7	45.0
z	6.0	65.0

In Figure 7.12, the reconstructed angular rate results of case 1 (blue line) and case 2 (red line) are compared to the official attitude product (yellow line) in an ASD plot. From the previously-mentione lines, it can be clearly seen that, already at the level of angular rates, the proposed approach performs better than SCA1B at frequencies between 10 mHz and 0.3 Hz. This is because the latter takes the noise characteristics of each

sensor into account explicitly, so the resulting angular rates at low frequencies consist solely from star camera data while at the higher frequencies from only IMU data. On the contrary, it appears that at high frequencies the Kalman filter approach fails to fully exploit the lower noise of the IMU angular rates and the star camera noise degrades the final solution.

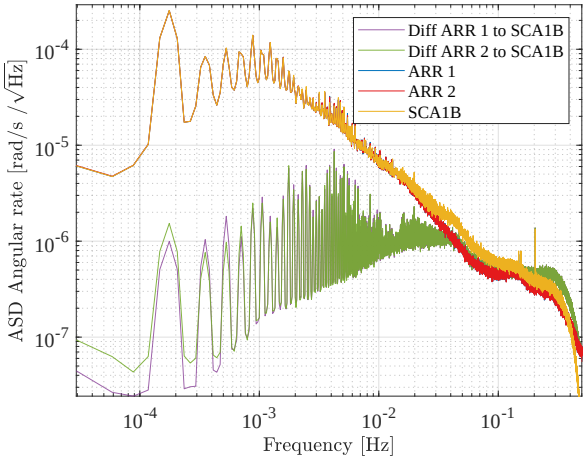

(a) x-component GRACE-FO C.

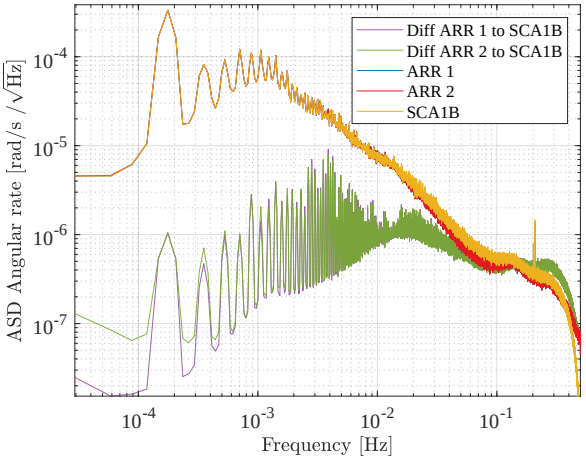

(b) x-component GRACE-FO D.

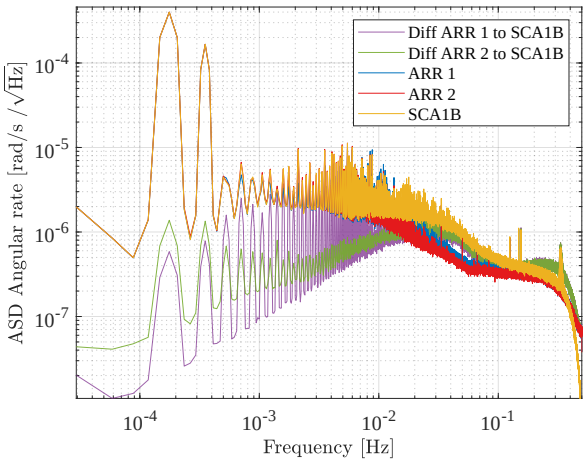

(c) y-component GRACE-FO C.

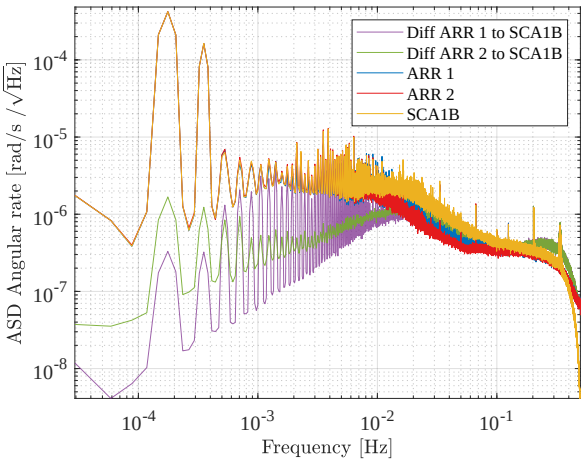

(d) y-component GRACE-FO D.

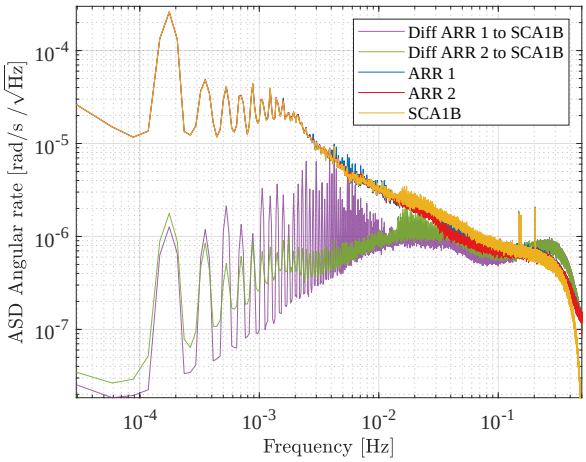

(e) z-component GRACE-FO C.

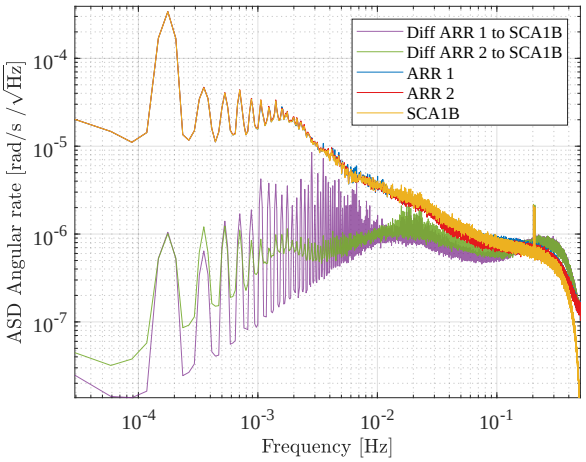

(f) z-component GRACE-FO D.

Figure 7.12: Comparison of the angular rates' ASD derived from the SCA1B data product and from the two angular rate reconstruction (ARR) cases, for GRACE-FO C and D.

Among all components of the angular rates, the *y* component displays the best improvement with respect to SCA1B, with a lower noise content starting already from around 6 mHz and extending up until 0.3 Hz. Specifically, for case 2, which takes into account steering mirror information, the red ASD curve is even slightly lower than the blue one. After 0.3 Hz the effects of the different down-sampling techniques become apparent as the drop of the ASD curves. As far as the *x* component is concerned, the differences to SCA1B are more visible compared to the *z* one. Still, both of them exhibit lower noise at frequencies between 20 to 200 mHz.

At a closer examination of the results between the two satellites, it is evident that for GRACE-FO D the official solution is somewhat closer to the reconstructed angular rates for both cases. This could be explained from the less noisy star camera measurements of this satellite compared to the other one, as seen in Section 7.1.1. Therefore, under these conditions the Kalman filter manages to combine star camera and IMU data in a more optimal way. The proposed reconstructed angular rates, however, do not face such an issue, since at higher frequencies only IMU measurements are used and the resulting angular rates are not impacted by the more noisy star cameras. With this in mind, it could be stated that at the level of angular rates the proposed approach can perform better, compared to a Kalman filter method, in case of noisy star camera measurements.

On the other hand, systematic errors in the star cameras, such as FoV errors, still remain in the reconstructed angular rates of the first case. Their presence can be recognized from the large spikes in the differences to the official solution (purple line) at frequencies between 0.8 and 10 mHz. For case 2 (green line), however, these spikes are much smaller, due to the higher weight on steering mirror measurements, which are not affected by such type of errors.

7.5. Attitude reconstruction

After the successful reconstruction of IMU and star camera angular rates, the latter can now be used with the optimally combined quaternions to reconstruct the inertial attitude of the satellites. As introduced in Section 5.4.2, within this MSc thesis four different scenarios were identified to obtain the latter. The first, or otherwise called nominal, scenario utilizes only star camera and IMU data to reconstruct the satellite's attitude. However, due to star camera errors remaining in the final quaternions, the formation of the three additional scenarios was prompted. With this in mind, first and foremost, in Section 7.5.1, the performance of the nominal case is evaluated at the level of pointing angles with respect to steering mirror measurements and the Kalman filter approach. Next, the supplementary attitude reconstruction scenarios are introduced and assessed with respect to the latter. Finally, the best scenario is chosen and an analysis is performed on the contribution of each sensor to the final attitude (Section 7.5.2). Since the results between the satellites are similar, the analyses in this section are presented for just GRACE-FO C, unless specified otherwise.

7.5.1. Attitude solution performance

A simple means to assess the performance of the reconstructed attitude solution is to compare it with the measurements of the steering mirrors at the level of pointing angles. This comparison serves also as an independent verification for the algorithm. Figure 7.13 depicts the ASD of the pitch and yaw pointing angles derived from the reconstructed quaternions of the nominal scenario (labelled "ATTR", red line) and the official data product (yellow line) as well as the ones measured directly by the steering mirrors (blue line) for GRACE-FO C. At first sight, it can be seen that for both angles the proposed attitude reconstruction method provides results as good as the ones obtained from the SCA1B product and with improvements, especially for pitch, at frequencies starting from around 10 mHz up until higher ones. As expected, it exhibits (not shown here) a far better performance than what can be achieved from the quaternions resulting from the star sensor combination (cf. Section 7.3), which are limited to around 9.6 μrad/$\sqrt{\text{Hz}}$ above 10 mHz. In other words, the reconstructed quaternions succeed in exploiting the low noise of star camera measurements at lower frequencies and the low noise of the reconstructed angular rates at higher frequencies. For this reason, an equivalent behavior in the results is observed with the ones of Section 7.4, but now at the level of angles (or quaternions). Furthermore, for pitch angles, the nominal ATTR appears to have very similar performance as the steering mirror measurements until 40 mHz, a frequency after which broadband noise of the PSS sensor is a limiting factor for this instrument. In fact, between 20 and 40 mHz the blue line seem to have an even slightly lower ASD curve compared to the red one.

Nevertheless, when inspecting the differences of the ATTR and the SCA1B products with the steering mirror data (purple and green line respectively), a greater discrepancy, in the form of larger spikes, is detected for the proposed attitude reconstruction method. The significantly larger spikes of the purple line are visible starting from the frequency of the 3$^{\text{rd}}$ orbital harmonic and continue up until around 10 mHz. At higher frequencies,

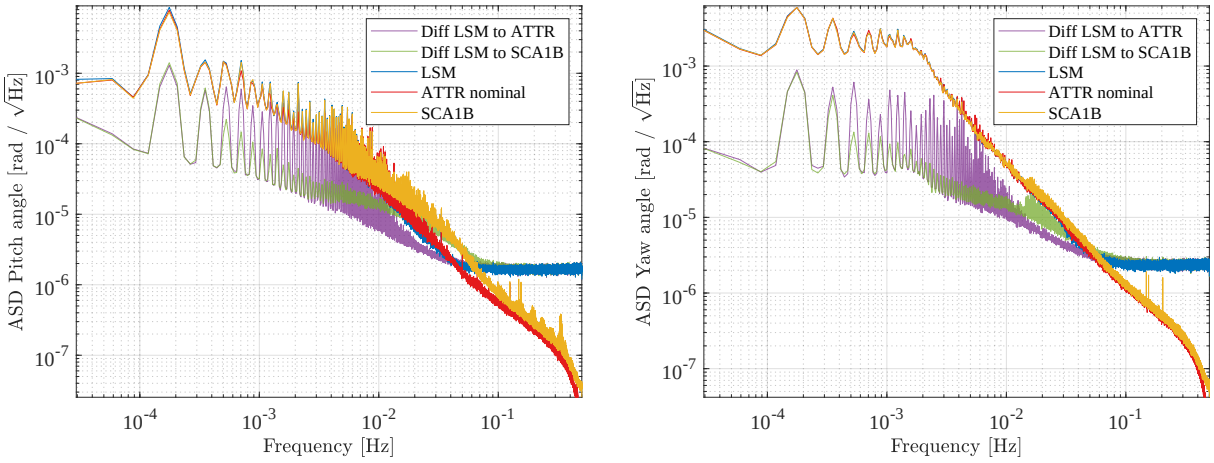

(a) Pitch angles.

(b) Yaw angles.

Figure 7.13: Comparison of the pitch and yaw pointing angles' ASD derived from the nominally reconstructed and the SCA1B quaternions and measured from the steering mirrors, for GRACE-FO C.

however, and more notably for the yaw angles between 15 and 30 mHz, SCA1B appears to be more noisy (green curve has larger spikes). By examination of the previous differences in an argument of latitude versus time plot, almost identical features can be recognized as the ones discussed in Section 7.3. Therefore, it is clear that star camera FoV errors continue to prevail in the nominally reconstructed attitude solution. At the higher frequencies, however, the latter relies almost entirely on IMU measurements, which are smoother, in comparison to SCA1B that possibly gives a bit more weight on star camera data.

Based on this finding, the three additional attitude reconstruction scenarios were identified and proposed so that the above-mentioned systematic effects can be addressed. Already from Section 7.3 and Section 7.4 it has been illustrated that the optimal combination of star camera and steering mirror quaternions is feasible and can correct FoV errors. Consequently, for the second scenario, the attitude is reconstructed based on the combined star camera and steering mirror quaternions and the second set of reconstructed angular rates of Section 7.4. For both last scenarios, a different approach is employed, for which the FoV errors are eliminated by applying quaternion corrections to the nominally reconstructed solution, according to the method in Section 5.2.4. For one case, this correction originates from reconstructed IMU-based quaternions and for the other from pure steering mirror quaternions. As mentioned in Section 5.4.2, the former are generated by using the IMU angular rates and a larger time window during the quaternion fitting in the attitude reconstruction algorithm. A time window two times as large as the one used for the nominal case is chosen. Even larger ones were tested, but produced identical results.

Figure 7.14 illustrates the ASD of the three small angles computed from the difference of the nominal reconstructed with the SCA1B, the steering mirror and the IMU-based quaternions (blue, red and yellow line respectively). By comparing the red and yellow lines to the blue one, it is clear that they exhibit similar spikes at the frequency range 0.1 to 10 mHz. This denotes that both the steering mirror and the IMU can explain more or less the same differences observed with respect to the SCA1B product. The only noticeable peculiarity is the rather large discrepancy of the x and z components of the IMU-based quaternions, at the 2^{nd} orbital harmonic. This behavior could indicate un-modeled errors in the IMU measurements that repeat twice per orbit. According to Wen et al. [2019], the IMU noise model in the Kalman filter setup, takes into account once- and twice-per-revolution effects, however, their origin is not discussed. Due to time constraints of this thesis, the origin is not addressed in this research either, but is recommended for future work.

In general, the IMU-based quaternions could be selected as the final attitude solution of the GRACE-FO satellites, since they express the same attitude as the nominal reconstructed case and are not affected by FoV errors. However, compared to pure star camera measurements, they are limited below 10 mHz, as it can be observed in Figure 7.14 with the increase of the yellow ASD curve towards lower frequencies. This behavior is due to small errors accumulating during the integration of the IMU angular rates and to the angle random walk, which is propagated from a flat noise spectrum at the level of angular rates to noise with $1/f$-behavior at the attitude level. Consequently, in order to remove this undesired noise, the technique described in Section 5.2.4 is proposed, for which a daily average correction is computed based of the quaternion differences with respect to the nominal solution.

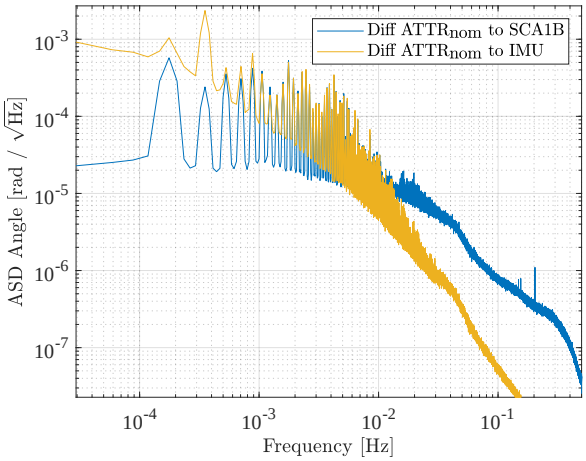

(a) x-component.

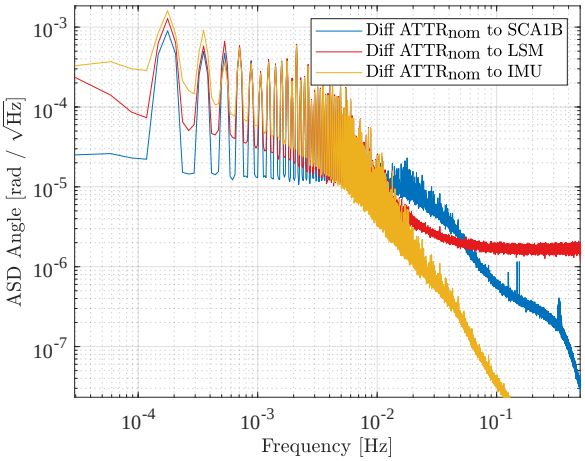

(b) y-component.

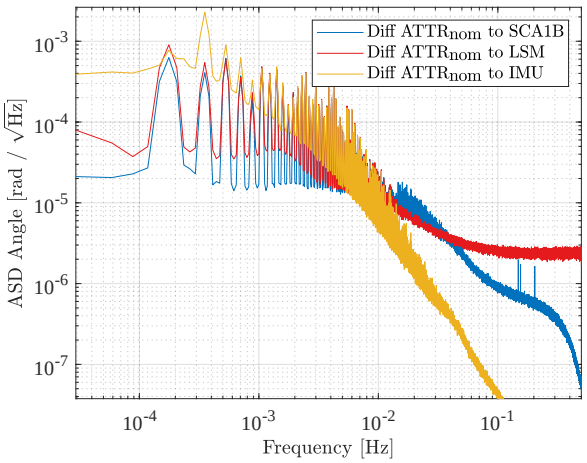

(c) z-component.

Figure 7.14: Comparison of the quaternion residuals' ASD between the nominal reconstructed scenario and the SCA1B, the steering mirrors and the IMU, for GRACE-FO C.

Given the above-mentioned attitude reconstruction scenarios, a comparison at the level of quaternions is performed relative to the Kalman filter approach, shown in Figure 7.15. From the figure it is clear that for all new scenarios the amplitude of the spikes is decreased considerably compared to the nominal case with the exception of the x component for the cases that use steering mirror data. Since this sensor does not provide any roll information, it is reasonable to expect similar results as the nominal case for this component. The only major distinction between the various scenarios is the slope of the red ASD curve at lower frequencies (between 0.1 and 10 mHz). As already discussed in Section 7.3, this indicates that the SCA1B quaternions, which do not incorporate steering mirror measurements, are most probably limited at those frequencies due to star camera random noise. Needless to say, any remaining differences that are observed in Figure 7.15 could originate from either the proposed or the Kalman filter method.

Among the three suggested scenarios, it is clear that the one that optimally combines steering mirror data at the level of quaternions is the best one since it not only corrects for FoV errors as good as the other scenarios, but it can also properly incorporate the steering mirror data that are more accurate at frequencies below 65 mHz. The only disadvantage of that case is that the x-component of the final attitude quaternions is not corrected. This can easily be addressed, however, by only applying a correction from the x-component of the IMU-based quaternions. This requires that possible errors in the IMU data that repeat twice per revolution are modelled and removed first. Nevertheless, as it has been described in Section 4.4, since the roll information of the satellite is not important for the AOC, the correction of this component will not have any effect either. Given the above reasons, it is claimed that scenario 2 can deliver the best attitude solution so far out of the three options and provide a more complete solution in the end.

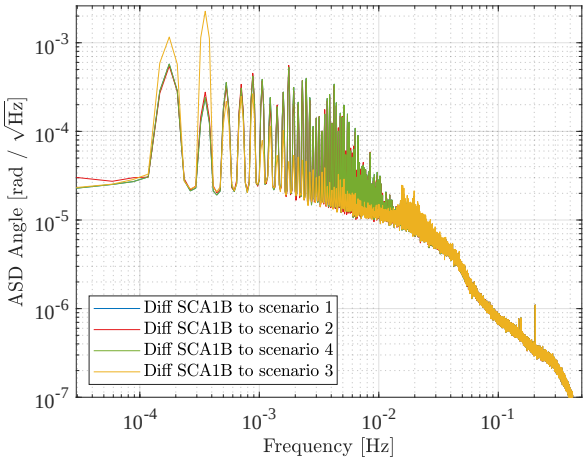

(a) x-component.

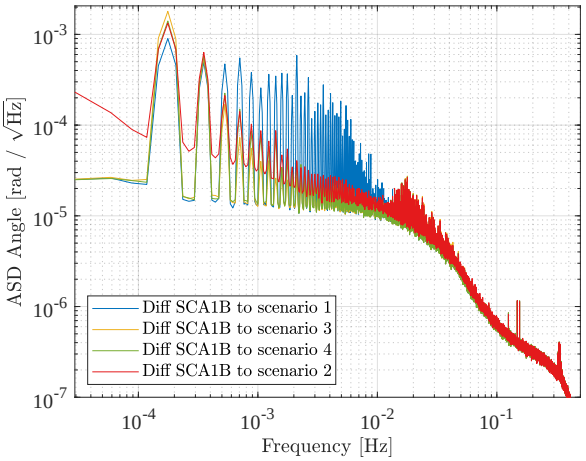

(b) y-component.

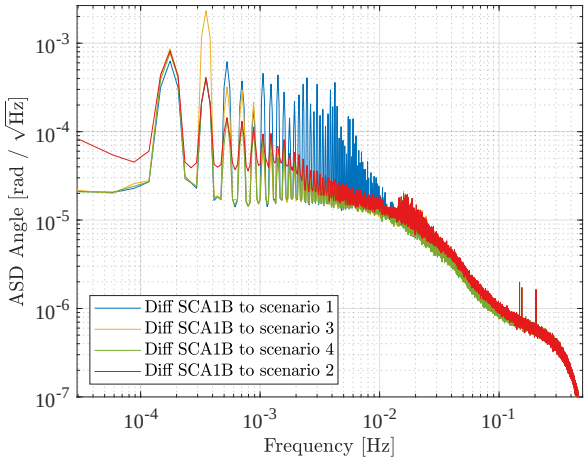

(c) z-component.

Figure 7.15: Comparison of the quaternion residuals' ASD between the SCA1B and the four different attitude reconstruction scenarios, for GRACE-FO C.

7.5.2. Sensor contribution

To understand better the performance of the proposed attitude reconstruction approach, a comparison can be performed with respect to the measurements of each individual sensor and determine in this way the contribution of each one to the final attitude solution. In Figure 7.16, the differences between the measured IMU angular rates and the ones derived from the reconstructed attitude and the Kalman filter method are demonstrated. The differences to the combined star camera data, which are affected by FoV errors, are also included in the same figure. In the following paragraphs, the results of the proposed approach are first discussed, and then those of the official solution.

First of all, from the slope of red ASD curve, the noise of the star camera quaternions that is proportional to the frequency can be observed at high frequencies. At the same time, the blue ASD curve exhibits a flat behavior at low frequencies, which indicates that the reconstructed attitude solution is mainly based on star camera or steering mirror data at those frequencies. Specifically, for the y and z components, the angular rates are derived predominately from IMU measurements above 45 and 65 mHz respectively. While for the x component, the transition appears to occur at an even lower frequency, such as 7 mHz. In fact, these values coincide with the crossing frequencies defined in the angular rate reconstruction process (see Table 7.5). Once again, since the reconstructed attitude method does not correct for any star camera FoV errors around the satellite's roll axis, these become apparent in Figure 7.16a, as the large spikes (blue curve). For the other two components, however, the differences exhibit a more or less flat noise spectrum, which in fact indicates the noise floor of the IMU measurements. Lastly, it should be noted that above 0.2 Hz the effects of downsampling the signals from 8 to 1 Hz measurements become visible as the increase of the blue ASD curve.

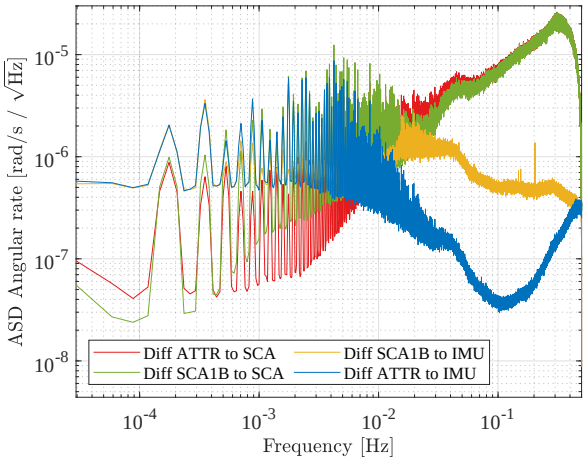

(a) *x*-component.

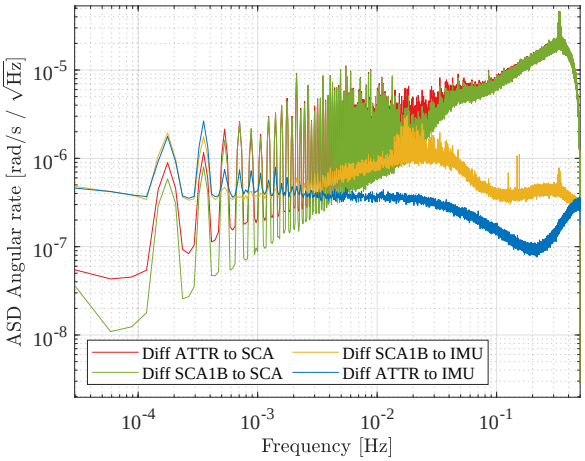

(b) *y*-component.

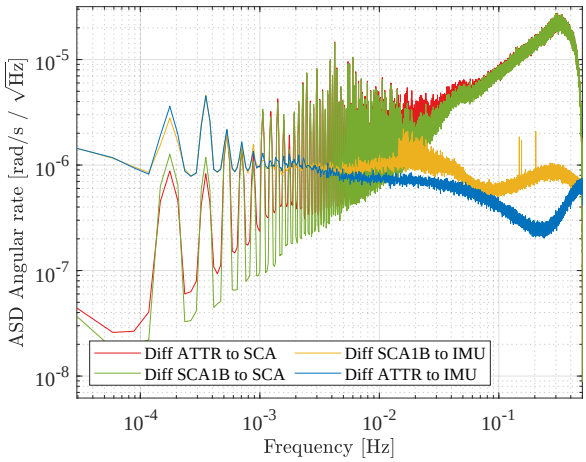

(c) *z*-component.

Figure 7.16: ASD of the differences between the proposed attitude and the Kalman filter approach angular rates to the ones obtained from the combined star cameras and IMU, for GRACE-FO C.

To get a better idea on the contribution of the star camera and the steering mirror data at frequencies below 45-65 mHz, Figure 7.17 can be used that depicts the ASD of the quaternion residuals between the combined star cameras, that are affected by FoV errors, and the proposed approach (blue line), the steering mirror (yellow line) and the SCA1B data product (red line). From the blue and the yellow lines, it becomes evident that the *y* and *z* component of the reconstructed quaternions are based predominately on steering mirror data, since they show very similar spectral characteristics, while the *x* component is derived from star camera data.

On the contrary, when examining the corresponding differences of the Kalman filter approach, it appears that it incorporates data from both star cameras and IMU across the whole frequency spectrum. For example, in Figure 7.16, at higher frequencies the yellow ASD curve has a far larger magnitude than the blue one and is more noisy between 15 and 40 mHz. This indicates that at those frequencies the solution is probably contaminated by star camera noise. Therefore, it is clear that the proposed attitude reconstruction method can exploit better the strengths of each instrument and provide a more accurate solution.

7.6. Mission impact

This section is dedicated to the mission impact of the proposed attitude reconstruction method. In Section 7.6.1, the impact on GRACE-FO is discussed in terms of the AOC and in Section 7.6.2 a recommendation is provided for NGGM based on the findings of the previous sections.

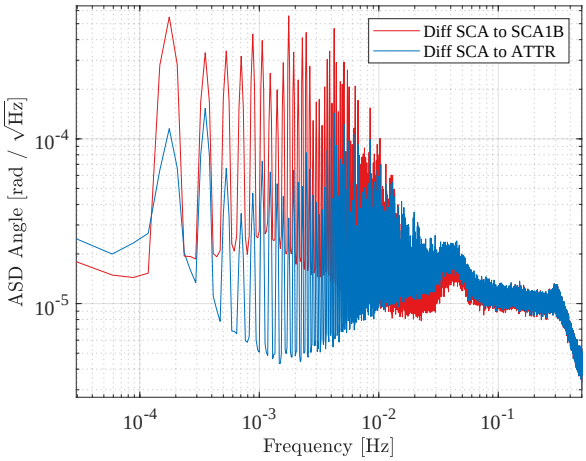

(a) x-component.

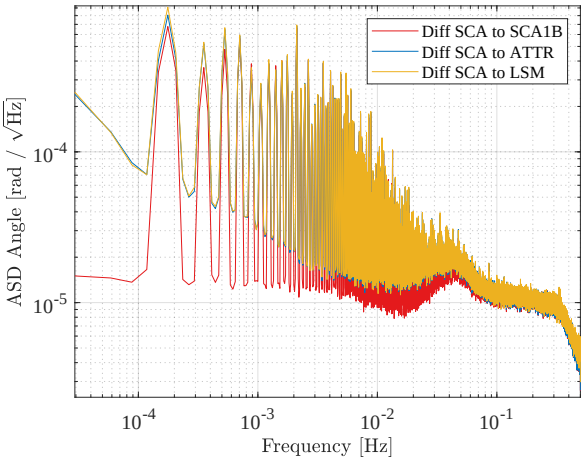

(b) y-component.

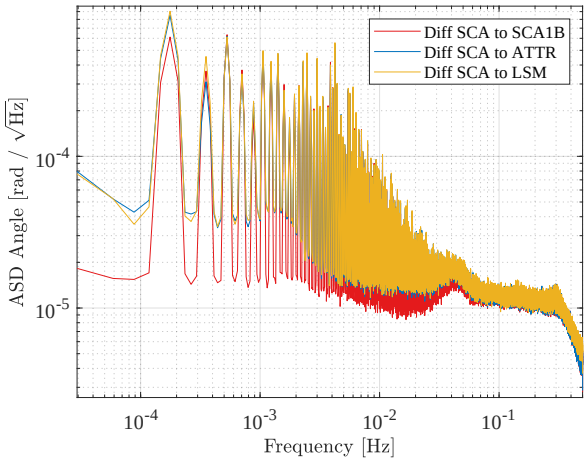

(c) z-component.

Figure 7.17: Comparison of the quaternion residuals' ASD between the combined star cameras and the steering mirrors, the proposed attitude reconstruction and the Kalman filter approach, for GRACE-FO C.

7.6.1. GRACE-FO

The accurate estimation of the twin satellites' attitude is essential for precisely correcting the GRACE-FO K-band ranging observations so that the inter-satellite range measurements can be related to their CoMs. This in turn has a direct impact on the estimated gravity field. Moreover, as indicated in Section 4.4, the AOC depends on 1) the phase center vector in the individual SF and 2) the pitch and yaw pointing angles which are also influenced by the orientation of the latter vector (as shown by Equation (4.2)). Already from Section 7.5, the improvements of the proposed attitude reconstruction approach have been illustrated in terms of these angles. Because a comparison and analysis at the level of the recovered gravity field is outside the scope of this thesis, the proposed and the official attitude solutions are analysed at the level of the AOC for range, range rate and range acceleration.

Before the discussion of the latter, it is important to mention another main disagreement between the two attitude approaches, that was not discussed so far in Section 7.5. This concerns the different pointing biases, i.e. the mean value of the pointing angle variations, observed for each method. In Figure 7.18 and Figure 7.19, the biases for the pitch and yaw angles and for both satellites are shown over the period of two orbits. From these figures, it is clear that each method exhibits a different pointing bias for each angle. In other words, this behavior indicates that although they can identify the same variations in attitude, they disagree on the mean orientation of the satellite with respect to inertial space. Irrespective of the attitude reconstruction method, the biases could be explained from an error that is common to all sensors and cannot be estimated during their relative calibration. Therefore, the disagreement between the two methods could be the different approaches used to calibrate the orientation of the sensors relative to each other.

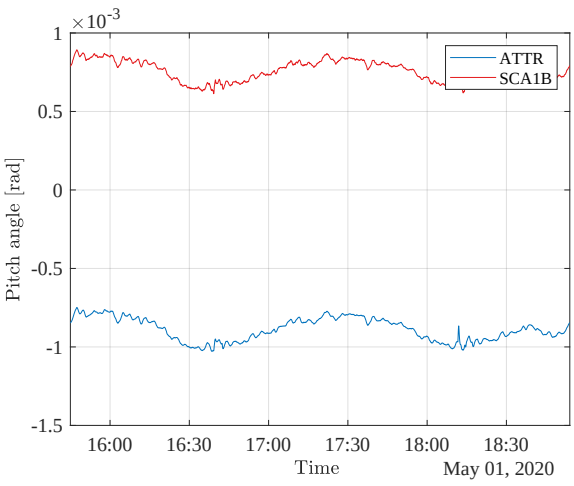

(a) GRACE-FO C.

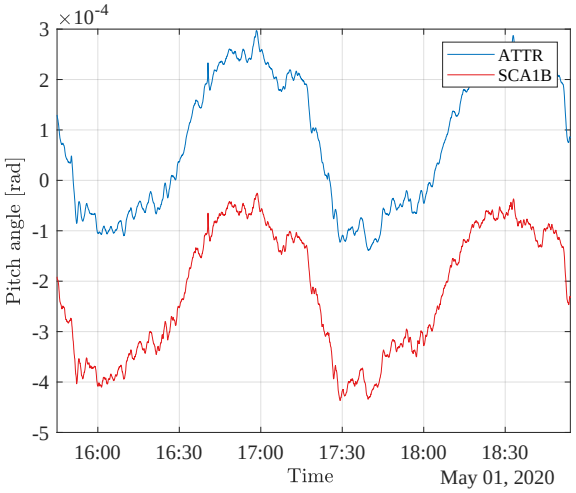

(b) GRACE-FO D.

Figure 7.18: Time series of the pitch pointing angles derived from the proposed attitude reconstruction and the Kalman filter approach.

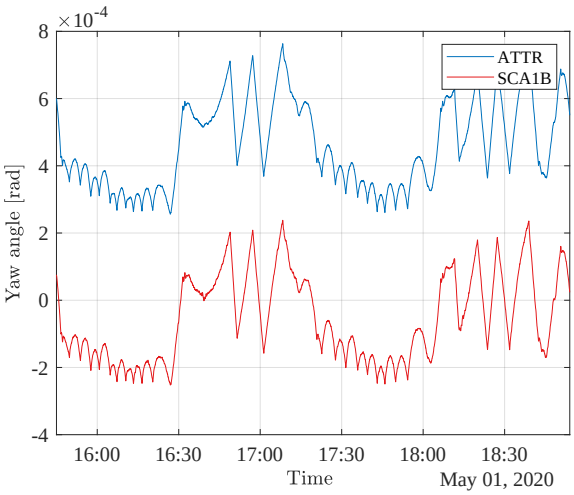

(a) GRACE-FO C.

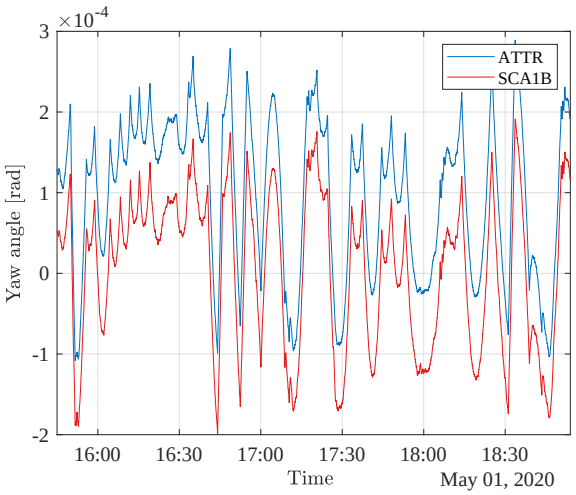

(b) GRACE-FO D.

Figure 7.19: Time series of the yaw pointing angles derived from the proposed attitude reconstruction and the Kalman filter approach.

Furthermore, as indicated by Bandikova [2015] and Horwath et al. [2011], these biases can affect significantly the AOC and in turn the recovered gravity field. To demonstrate this effect, in Figure 7.20, the time series of the derived corrections for range from both approaches are presented. Due to the larger, on average, pointing biases of the proposed method, the respective correction exhibits larger variations than the Kalman filter solution. Similar behavior can be observed for the correction for range rate and acceleration. In general, a small value for pitch and yaw could denote that the AOCS is capable of keeping more or less the two satellites aligned to each other, however, it does not necessarily mean that lower magnitudes in the computed pointing biases are closer to the truth. Given the analysis performed so far and due to the lack of reference, it is not viable to designate which method provides a more accurate mean orientation of the satellites with respect to inertial space.

Therefore, to make a fair comparison, the proposed attitude solution is rotated to the same reference frame as the official one by applying three small constant angles to the quaternions of the former. In Figure 7.21, the ASD of the AOC for range, range rate and range acceleration of the rotated reconstructed and the Kalman filter solution are illustrated. Once again, clearly the proposed approach shows a considerable improvement for all corrections at frequencies higher than 10 mHz. However, at a closer inspection of Figure 7.21b, it becomes evident that the improvements on the AOC are far lower than the KBR system noise. The same effect was also observed when the Kalman filter was rotated to the reference frame of the proposed solution (not shown here). Thus, at the level of gravity field, no significant change is anticipated.

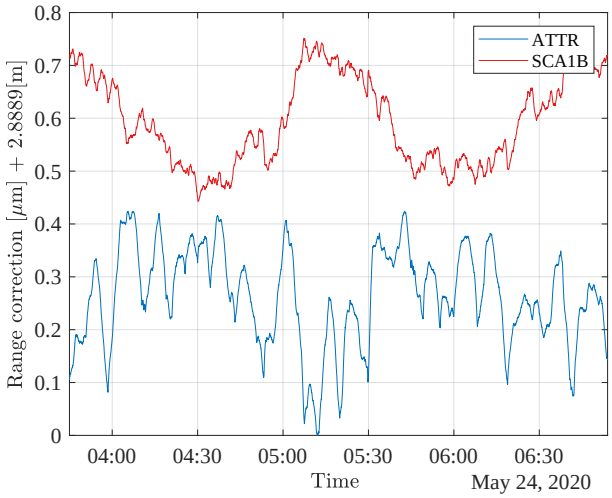

Figure 7.20: Time series of the antenna offset correction for range computed from the proposed attitude reconstruction and the Kalman filter approach.

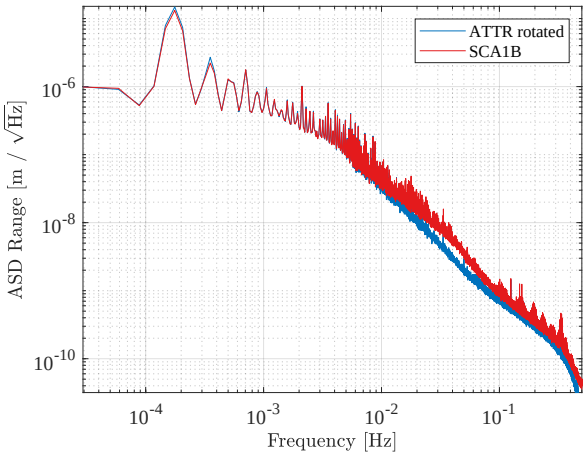

(a) Range.

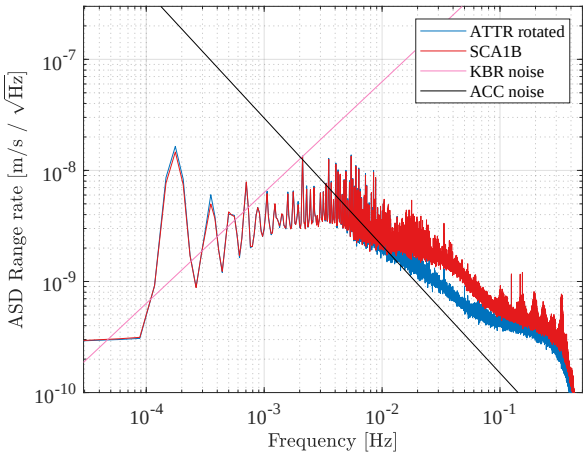

(b) Range rate.

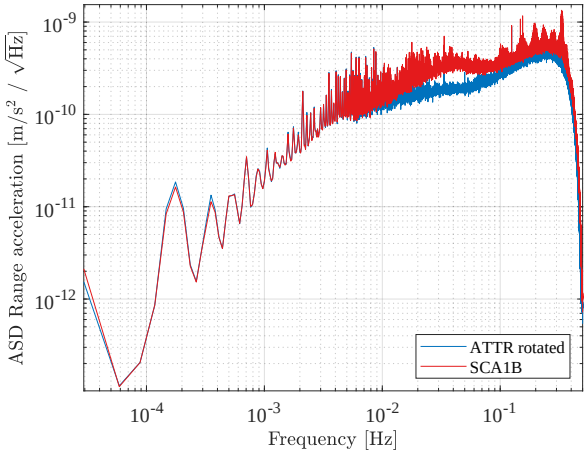

(c) Range acceleration.

Figure 7.21: Comparison of the antenna offset correction for (a) range, (b) range rate and (c) range acceleration derived from the proposed attitude reconstruction with the ones based on the Kalman filter approach.

7.6.2. NGGM

Although, the new reconstructed attitude dataset is not expected to show any significant changes at the level of gravity field estimates for GRACE-FO, the results of the analyses in this thesis work can be valuable for the design of future gravity missions. Given the outcome on the performance of the instruments on-board the GRACE-FO satellites as well as the performance of the proposed data fusion methods, a reflection can be made on their impact to the design of the NGGM proposed by ESA.

According to Haagmans et al. [2020], the NGGM design concept will be similar to that of GRACE and GRACE-FO, i.e. twin satellites flying in the same orbit, but now the primary payload for measuring the inter-satellite distance would be the laser ranging interferometer. Additionally, for redundancy purposes two accelerometers will be added to each satellite, either both of them placed symmetrically around the satellite CoM, or a main one placed in the latter and the other one at a small distance to the center. In case, one fails from the first configuration or the main one fails from the second configuration, the measured accelerations need to be corrected for gravity gradient, centrifugal and Euler acceleration effects in order to retrieve the non-gravitational accelerations of the satellite. To achieve this, the accurate estimation of the satellite's angular rates is required. Considering this failure case, an investigation is performed to examine how accurately the correction can be obtained given the estimated noise in the star camera, the IMU and the steering mirror measurements and the proposed angular rate reconstruction method. This analysis is motivated by the fact that a degraded accelerometer performance could potentially occur for NGGM, and in fact, it has already been observed for GRACE-FO D, for which the reasons behind it have not yet been fully understood either [Landerer, Flechtner, et al., 2020].

With the above in mind, for an accelerometer mounted at a distance from the CoM, the measured acceleration is equal to [Siemes et al., 2019]

$$\mathbf{a} = -(\mathbf{V} - \boldsymbol{\Omega}^2 - \dot{\boldsymbol{\Omega}})\mathbf{r} + \mathbf{d} \tag{7.5}$$

where $\mathbf{V}$ is the gravity gradient tensor, $\mathbf{d}$ is the non-gravitational accelerations acting on the satellite, $\mathbf{r}$ is the vector from the satellite's CoM to the center of the accelerometer and $\dot{\boldsymbol{\Omega}}$ is the first time derivative of $\boldsymbol{\Omega}$, which is the angular rate tensor defined as

$$\boldsymbol{\Omega} = \begin{bmatrix} 0 & -\omega_z & \omega_y \\ \omega_z & 0 & -\omega_x \\ -\omega_y & \omega_x & 0 \end{bmatrix} \tag{7.6}$$

where $\omega_{x,y,z}$ denote the angular rates around each axis of the satellite frame. The desired correction for centrifugal and Euler accelerations are calculated as follows

$$\mathbf{a}_{\text{corr}} = \mathbf{a}_{\text{centrifugal}} + \mathbf{a}_{\text{euler}} \quad \text{with} \quad \begin{aligned} \mathbf{a}_{\text{centrifugal}} &= \boldsymbol{\Omega}^2\mathbf{r} \\ \mathbf{a}_{\text{euler}} &= \dot{\boldsymbol{\Omega}}\mathbf{r} \end{aligned} \tag{7.7}$$

For this analysis, three different cases are considered depending on the position of the accelerometer with respect to the satellite axes. For the first one, it is assumed to be placed in the along-track direction, for the second one in the cross-track direction and for the last one in the radial direction. For all cases, however, the accelerometer is placed at a distance of 10 cm from the CoM. Given the noise characteristics of the star cameras, the steering mirrors and the IMU as well as the proposed angular rate reconstruction method, the corresponding noise in the acceleration correction is computed with Equation (7.7). Together with the estimated double time derivative of inter-satellite distance and accelerometer measurement noise for the NGGM (see Fig. 14 in [Massotti et al., 2021]), Figure 7.22 is created, that illustrates the noise curves of all the previous components in an ASD plot. Note that the acceleration correction shown in this figure refers to the one in the along-track direction, i.e. $\mathbf{a}_{\text{corr},x}$, since this component is of interest for deriving gravity field estimates.

It is clear that for case 2 and 3 at frequencies above 1 mHz, the noise in the laser interferometer is not anymore the limiting factor for estimating the gravity field, but instead the centrifugal and Euler acceleration correction. On the contrary, when the accelerometer is placed in the along-track direction, then the Euler acceleration is zero in that direction and $\mathbf{a}_{\text{corr},x}$ is far below the noise of the interferometer. This information should be taken into account during the design of the NGGM, so that either the accelerometers are placed in the most favorable position or the satellites are equipped with the correct attitude sensors to meet the science objectives of the mission.

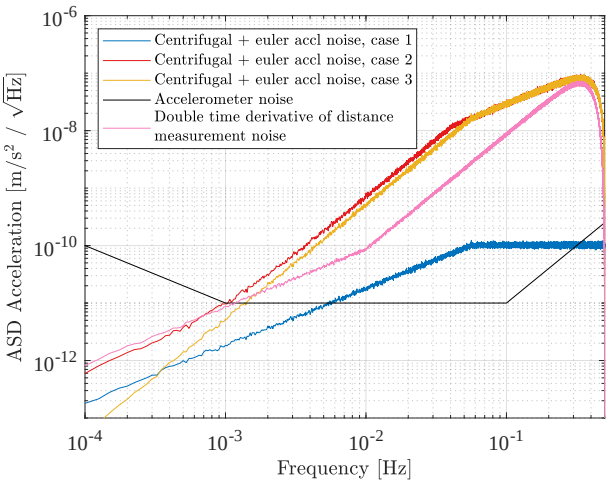

Figure 7.22: Comparison of the noise in the accelerometer and the laser ranging measurements with the noise in the centrifugal and Euler accelerations in the along-track direction computed based on reconstructed angular rates.

8

Conclusions and Recommendations

In this part of the report, the answers to the research questions and detailed conclusions, that follow from the results described in the last chapter, are presented (Section 8.1) as well as the relevant recommendations for future work (Section 8.2).

8.1. Conclusions

The objective of this MSc thesis, as stated in Section 3.4, was to answer the following research question:

to what extent can a new attitude sensor data fusion method improve the current attitude solution by accurately incorporating the noise and error characteristics of the GRACE-FO star trackers, fiber-optic gyroscopes, accelerometers and laser ranging interferometer's steering mirrors?

To achieve this, appropriate sub-questions were formulated. In the following paragraphs, these questions are addressed first and in the end an answer is given to the main research question.

1. **What properties describe the noise and error characteristics of the GRACE-FO star cameras, fiber-optic gyroscopes, accelerometer and laser ranging interferometer's steering mirror measurements?**
   In general, the noise and error characteristics of each instrument was determined by analysing relevant time series, ASD and argument of latitude versus time plots. The analyses were performed over the duration of May 2020, for which all instruments could provide nominal data.

   Star cameras: Based on the noise components estimated during the optimal combination of star camera and steering mirror quaternions, monthly RMS values of the random noise in the star camera measurements were calculated. Overall, all cameras perform close to the specified 2 arcseconds accuracy, with the ones on GRACE-FO D exhibiting a slightly better performance than GRACE-FO C. The exception is for star camera 2 of the latter satellite, which shows the worst performance of them all (i.e. ~3.3 arcseconds around the cross-boresight axes). This behavior is attributed to its unexpected blinding from the Sun at locations where camera 3 of GRACE-FO D, that views similar part of the sky, kept on providing nominal attitude data. In contrast, camera 1 of both satellites has the best accuracy, since over the period of one month it is least affected by Sun and Moon intrusions and has on average the largest number of stars in its FoV. The noise level ratio between the boresight and the roll about the boresight pointing for star camera 1, 2 and 3 is 11, 13 and 11 respectively for GRACE-FO C and 12 for all cameras of GRACE-FO D. Furthermore, the analysis of the differences between the IBAs determined by a preliminary knowledge of the cameras' orientation in the SF and by in-flight measurements revealed constant offsets. These indicate that the alignment of the cameras in the SF was not determined perfectly. For camera pairs 1-2, 1-3 and 2-3 of GRACE-FO C, the offsets amount approximately to 40, 49 and 54 arcseconds respectively, and for GRACE-FO D to 73, 45 and 69 arcseconds. Last but not least, by comparing star camera and steering mirror data, as expected, it was found that the former is subjected to FoV errors.

   Fiber-optic gyroscopes: For both satellites, the measurements of the gyroscopes exhibit a slightly better performance than the specified angle random walk. This improvement is equivalent to around a 11% lower noise floor. Moreover, the analysis of low-pass filtered star camera and IMU angular rates revealed small constant biases of a few μrad, indicating a misalignment between the two instruments.

   Accelerometer: McCullough et al. [2019] has already mentioned that the accelerometer data of GRACE-FO are affected by large spurious accelerations that produce the phantom accelerations and an improper response at thruster firings. After removing both of the latter, more accurate thruster responses were reintroduced based on a simple model that assumes a constant acceleration over the duration of the firing. Then, the comparison of the derived angular rates ASD to the ones from the star cameras and the IMU demonstrated an unexpectedly large disagreement at frequencies between 1 and 10 mHz. This

discrepancy is specifically visible for the z and x component of the angular rates and does not allow for a proper calibration and fusion of the data. Due to time constraints, a definite explanation for this behavior was not found. Therefore, the accelerometer was not used further in the attitude reconstruction process.

LRI steering mirrors: For both satellites, the pitch and yaw measurements have respectively a noise floor equal to 0.27 and 0.37 arcseconds/$\sqrt{\text{Hz}}$. These values correspond to the broadband noise of the position sensing system sensor and they are around 10 times better than the accuracy of the star cameras.

2. **What methods can be used to fuse the measurements of the star cameras, the fiber-optic gyroscopes and the laser ranging interferometer's steering mirrors?**
First and foremost, the individual star camera quaternions are optimally combined based on the approach discussed in Section 5.1 that takes into account the anisotropic accuracy of the measurements. Within this combination, a set of constant biases are also estimated that correct for the offsets in the IBA differences identified during the star camera error assessment. In a similar manner, it was found that steering mirror derived quaternions can also be combined with the star camera ones. During the combination a 10 times higher weight is specified for the y and z components of the steering mirror quaternions and a zero weight for the x one, since no information about the satellite's roll is captured by that instrument. In the next step, the IMU measurements are calibrated based on a linear gyro error model, using the angular rates derived from the optimal quaternions.

   Then, the optimally combined quaternions and calibrated IMU data are fused at the level of angular rates according to the method described in Section 5.3. With the use of a lowpass and a highpass filter the reconstructed angular rates are composed at low frequencies of purely star camera and steering mirror data and at high frequencies of purely IMU data. The crossing frequencies that defined the above filters were determined as the points where the estimated noise floors of the instruments intersect in an ASD plot. For both satellites, the same crossing frequencies were chosen and correspond to 7.0, 45 and 65 mHz, respectively, for the x, y and z components of the angular rates. At the same time, to reduce the transient effects of the filter operations, at the beginning and at the end of the time series, filters with shorter length were constructed and applied to these areas.

   Finally, to reconstruct the attitude of the satellites, the method presented in Section 5.4.1 is employed, for which a generalized least squares adjustment is used to fit a set of attitude quaternions, which result from the integration of the smooth reconstructed angular rates, to the optimally combined quaternions. According to this technique, the first, or otherwise called nominal, scenario was identified, for which reconstructed quaternions were obtained by using only star camera and IMU data. The comparison of the pointing angles derived from the nominal scenario with the ones measured by the steering mirrors, verified the attitude reconstruction approach, but also indicated that star camera FoV errors were still contaminating the attitude solution. To model these errors three additional scenarios were investigated.

   For the second scenario, the steering mirror quaternions are first optimally combined with the star camera ones and then the angular rates derived from the combined quaternions are merged with IMU data. The final attitude is reconstructed based on the previously-mentioned combined quaternions and reconstructed angular rates. For the third scenario, IMU-based quaternions are reconstructed, that can express the same inertial attitude as the star camera quaternions, but are limited at low frequencies due the angle random walk in the IMU measurements. By computing a daily average correction based on the quaternion differences between the IMU-based and the nominally reconstructed quaternions and applying it to the latter, FoV errors are reduced. For the last scenario, the same procedure as with the previous one is followed, but now steering mirror quaternions are used instead. For the two scenarios that make use of steering mirror measurements, the x-component of the reconstructed quaternions cannot be corrected for FoV errors, since the steering mirrors do not provide any roll information. This can easily be addressed by applying a correction from only the x-component of the IMU-based quaternions.

   All three additional scenarios were able to correct the star camera FoV errors equally well, however, the second one (cf. Figure 7.15) is chosen as the proposed method to reconstruct the attitude of the GRACE-FO satellites. The reason for this choice is that it can properly incorporate the steering mirror measurements which are more accurate than the star camera ones at frequencies below 65 mHz.

3. **To what extent can the newly-developed methods improve the already existing satellite attitude dataset for the GRACE-FO mission?**
At the level of quaternions, the proposed attitude reconstruction method, provides a solution that performs as good as the the Kalman filter approach with noticeable improvements at frequencies above 10

mHz. In general, the new attitude dataset succeeds in fully exploiting at lower frequencies the low noise of star camera and steering mirror quaternions and at higher frequencies the low noise of the attitude quaternions resulting from the smoother reconstructed angular rates. In other words, below 65 mHz, the final attitude is predominately based on star camera and steering mirror measurements, while above that, on IMU measurements. For this reason, in the case of GRACE-FO C, where the star camera data were a bit more noisy than GRACE-FO D, the proposed method could still provide a smooth attitude, in comparison to the Kalman filter approach, which fails to extensively benefit from the advantages of the IMU.

4. **To what extent can an improved attitude reconstruction method benefit the GRACE-FO mission?** Once again, at frequencies greater than 10 mHz, the proposed attitude reconstruction method exhibits a better performance than the Kalman filter at the level of the AOC for range, range rate and range acceleration. However, due to the KBR system noise being the dominant source at higher frequencies, only minor improvements are expected at the level of gravity field.

Given the answers to the previous questions, the main research question can now be addressed properly. All in all, it can be stated that the proposed attitude data fusion method produces an improved attitude solution that incorporates more accurately the noise and error characteristics of the instruments under consideration than the official solution. This leads to noticeable improvements at the level of quaternions at frequencies above 10 mHz. The new attitude dataset comprises at low frequencies of accurate star camera and steering mirror data and at high frequencies of IMU data. Within this work, two ways to accurately and appropriately incorporate steering mirror measurements have been illustrated. Their inclusion in the final attitude solution appears to be highly beneficial, due to their lower noise and their advantage of not being affected by FoV errors.

Although, the achieved improvements in the attitude dataset are not expected to show any considerable changes in the derived gravity field, because of KBR system noise prevailing at high frequencies, the findings of this thesis could be essential for the design of future gravity missions such as the NGGM. Given the estimated noise characteristics of the above instruments and the proposed angular rate reconstruction method, the most favorable placement of the accelerometers was found to be in the along-track direction. If an accelerometer fails in this configuration, the noise in the required centrifugal and Euler acceleration corrections will be less than that of the laser ranging system. This information should be taken into account during the design of the NGGM, so that either the accelerometers are placed in the most advantageous position or the satellites are equipped with the correct attitude sensors to meet the science objectives of the mission.

8.2. Recommendations

Regardless of the numerous analyses performed in this research and the improvements of the new attitude reconstruction method, there are a few interesting points that require further investigation and could provide even additional improvements for GRACE-FO and for future gravity missions. These recommendations are listed below in order of significance:

- In this work, the analyses were limited to a relatively small time scale, i.e. a period of one month. The next step would be to investigate the long-term characteristics of quaternions, angular rates and pointing angles measured by the star cameras, the IMU and the steering mirrors respectively. Such analysis could reveal additional systematic errors in the data at very low frequencies that could later be modelled and removed from the attitude solution. These errors can include temperature dependencies that can affect the measurements of the instruments. For example, the latter could be indicated by examining any correlations with the β' angle (i.e. the angle between the vector to the Sun and the satellite orbit). In case of thermal dependencies on star camera data, the proposed attitude reconstruction method can easily account for them. For instance, during the estimation of the constant biases, additional parameters can be added that can model the temperature induced variations, as it was also performed for GOCE by Siemes et al. [2018]. Overall, to be successful in this investigation, a good knowledge at the level of system performance is required, since at those very low frequencies the latter has a higher significance than merely sensor performance.

- Moreover, the optimal combination of star camera quaternions could be further improved by extending the approach presented in this thesis to account for the higher noise in the measurements obtained in the proximity of invalid data. In general, quaternions measured a few epochs just before data are declared invalid, due to the detection of a big bright object in the FoV, have a degraded accuracy. Therefore,

as an example, a lower weight could be assigned on these measurements during the combination. The same idea could be applied to epochs where there is a transition from two (or three) to one star camera.

- To gain a complete understanding of the star camera and steering mirror measurement performance, additional research could be performed in this area. More specifically, it would be essential to identify for which instrument the orientation with respect to the satellite frame can be determined more precisely. This can have a positive effect on the AOC for range rate and subsequently on the gravity field.

- From the analysis on the estimated noise of the star cameras, it was found that camera 2 of GRACE-FO C was not performing as accurately as expected as the other ones. The reason for this behavior was assumed to originate from the unexpected blinding from the Sun at locations where camera 3 of GRACE-FO D, that views similar part of the sky, kept on providing nominal attitude data. Nevertheless, the latter has not been verified as the main cause, but could be confirmed by analysing the star camera pointing and the relative location of the Sun at the epochs of interest. In any case, it would be beneficial to investigate further the behavior of that camera, but also the in-flight performance of all cameras at longer timescales.

- Given the estimated noise characteristics of the star cameras, the steering mirrors and the IMU, and the proposed angular rate reconstruction method, the most favorable placement of the NGGM accelerometers was found to be in the along-track direction. A key variable of the centrifugal and Euler acceleration correction is the distance of the accelerometer from the CoM. In this work, a distance of 10 cm was assumed, but a more accurate estimation should be considered to ensure that the noise in the required correction will still be less than that of the laser ranging system in the event that one of the accelerometers fails.

- Finally, despite the fact that only the GRACE-FO C accelerometer can accurately measure the angular accelerations of the satellite, it would still be of interest to properly calibrate and process the accelerometer measurements and then use them within the attitude reconstruction method presented in this thesis. Additionally, the comparison of the angular acceleration measurements with those derived from the reconstructed attitude could potentially be useful for understanding the degraded performance of the GRACE-FO D accelerometer.

A

Appendix A: Reference Frames

In this appendix the definitions of the various time and coordinate frames used within GRACE-FO Level-1 data products will be presented. The information was retrieved from Wen et al. [2019].

A.1. Time Frames

A.1.1. Receiver Time

Each of the GRACE-FO satellites is equipped with an Ultra-Stable Oscillator (USO) which serves as the time and frequency reference for that satellite and is used to define the Receiver Time. Thus, it can be said that the Receiver Time refers to its specific realization on-board each satellite. The GPS and K-band ranging (KBR) measurements as well as the Instrument Processing Unit (IPU) are time-tagged to within 50 pico-seconds of the Receiver Time. The time-tags of the latter in the Level-1 products are given in seconds since the epoch of January 01, 2000, noon 12:00 hours (GPS time).

A.1.2. OBC Time

The OBC Time is defined based on its internal quartz oscillator, unlike the receiver time which is based on the USO. The OBC time-tagging is used for any measurements that are not GPS, KBR or IPU. The OBC to receiver time mapping is available in the telemetry measurements.

A.1.3. GPS Time

The GPS Time for the two GRACE-FO satellites is defined as seconds since the epoch of January 01, 2000, noon 12:00 hours. This definition is different from the ones of other mission that express GPS time as seconds past January 06, 1980, 00:00:00.

A.1.4. LRI Time

The LRI Time is defined based on the USO frequency and hence, at first glance it runs at the same rate as the Receiver Time. However, since it is initialized via a signal sent from the OBC, a delay or bias, called the datation bias, is introduced, which persists until the LRI is rebooted again.

A.1.5. Timing

All Level-1B data products are time-tagged in GPS Time and no additional time-tag corrections are required to use them. The Level-1A data products that contain measurements are time-tagged in OBC Time with a few exceptions. For example, the IHK1A product that contains housekeeping data, is time-tagged in Receiver Time and the LRI measurements are time-tagged in LRI time. Figure A.1 describes the process of converting LRI and OBC time-tags to GPS time-tags.

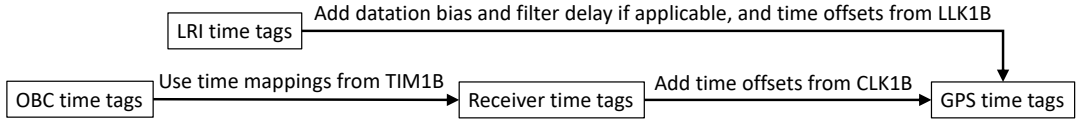

Figure A.1: Process to convert time tags from one GRACE-FO time frame to another. Source: [Wen et al., 2019]

A.2. Coordinate Systems

Figure A.2 illustrates the various body-fixed coordinate frames, used by the Level-1 data products. All of these frames are explained in the following subsections.

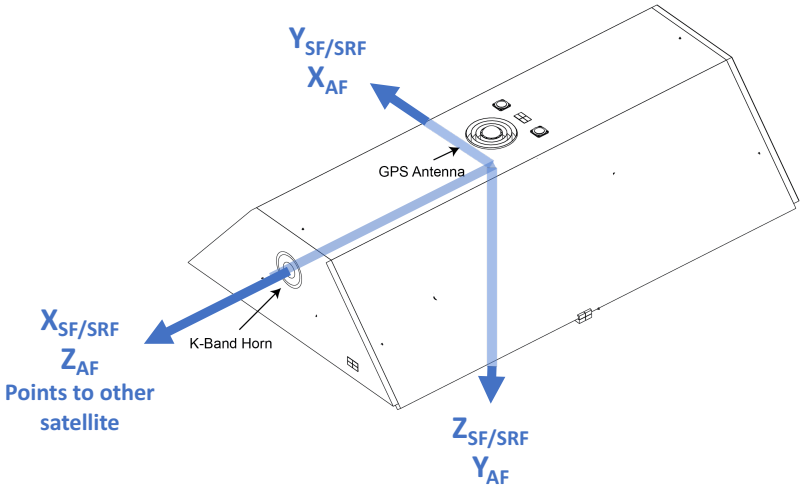

Figure A.2: The GRACE-FO satellite-body fixed frames, namely the satellite frame, the accelerometer frame and the science reference frame, in relation to the satellite body. Source: [Wen et al., 2019]

A.2.1. Satellite Frame - SF

The satellite frame has the same origin as the accelerometer frame, which is within 0.1 mm of the satellite's CoM. The coordinate axes of SF are defined as follows:

- X_{SF} is the roll axis of the satellite and it points from the origin to a target location on the phase center of the K/Ka Band horn
- Y_{SF} is the pitch axis of the satellite and it forms a right-handed triad with X_{SF} and Z_{SF}
- Z_{SF} is the yaw axis, normal to the roll axis and to the plane of the main equipment platform and positive towards the Earth.

A.2.2. Accelerometer Frame - AF

As the name suggests, the origin of the accelerometer frame is defined to be at the CoM of the ACC proof mass and its coordinate axes are defined as follows:

- $X_{\mathrm{AF}} = +Y_{\mathrm{SF}}$
- $Y_{\mathrm{AF}} = +Z_{\mathrm{SF}}$
- $Z_{\mathrm{AF}} = +X_{\mathrm{SF}}$

A.2.3. Science Reference Frame - SRF

The science reference frame has the same origin and coordinates axes as the satellite frame. To keep consistency within the Level-1B products, all of them are provided in the SRF.

A.2.4. Star Camera Frame - SCF

Each star camera on-board the GRACE-FO satellite has it own star camera frame. The origin of all SCFs is at the intersection of the boresight axis with mounting plane for each star tracker head. The +Z axis of the SCF is extended out along the boresight axis and the +X and +Y axes are found on the optical plane of the star tracker. The QSA1B data product contains the quaternions that define the rotation from each SCF to the SRF.

A.2.5. K-frame

The K-band ranging antenna horn is related to this frame. Its origin is the CoM maintained by the Center of Mass Calibration and Trim maneuver and its axes are defined as follows [Bandikova, 2015]:

- X_{KF} coincides with the calibrated center-of-mass to phase center vector
- Y_{KF} forms a right-handed triad with X_{KF} and Z_{KF}
- Z_{KF} is computed with $X_{\mathrm{KF}} \times Y_{\mathrm{SF}}$

A.2.6. Line-of-Sight frame

The axes of the Line-of-Sight frame are defined as follows [Bandikova, 2015]:

- X_{LOSF} coincides with the imaginary line that connects the GRACE-FO C CoM with the one of GRACE-FO D
- Y_{LOSF} is computed as the cross product of X_{LOSF} and the position vector of one satellite defined in the inertial Earth-centered frame
- Z_{LOSF} forms a right-handed triad with X_{LOSF} and Y_{LOSF}

B

Appendix B: Quaternions

The presented information on quaternions was retrieved from Diebel [2006].

B.1. General Quaternions

A quaternion $\mathbf{q} \in \mathbb{H}$, can be represented as a vector:

$$\mathbf{q} = [q_0,\ q_1,\ q_2,\ q_3]^T = \begin{bmatrix} q_0 \\ \mathbf{q}_{1:3} \end{bmatrix} \tag{B.1}$$

where q_0 is the real element of the quaternion and q_1, q_2 and q_3 are the imaginary elements. The conjugate, norm and inverse of the quaternion $\mathbf{q}$ are defined respectively as:

$$\overline{\mathbf{q}} = \begin{bmatrix} q_0 \\ -\mathbf{q}_{1:3} \end{bmatrix} \tag{B.2}$$

$$\|\mathbf{q}\| = \sqrt{q_0^2 + q_1^2 + q_2^2 + q_3^2} \tag{B.3}$$

$$\mathbf{q}^{-1} = \frac{\overline{\mathbf{q}}}{\|\mathbf{q}\|} \tag{B.4}$$

For a unit quaternion, we have $\|\mathbf{q}\| = 1$. It should be noted that the quaternion multiplication is not commutative. Quaternion multiplication between quaternions $\mathbf{q}$ and $\mathbf{p}$ is defined by:

$$\begin{aligned} \mathbf{q} \cdot \mathbf{p} &= \mathbf{q}_m(\mathbf{q}, \mathbf{p}) \\ &= \begin{bmatrix} q_0 p_0 - \mathbf{q}_{1:3}^T \mathbf{p}_{1:3} \\ q_0 \mathbf{p}_{1:3} + p_0 \mathbf{q}_{1:3} - \mathbf{q}_{1:3} \times \mathbf{p}_{1:3} \end{bmatrix} \end{aligned} \tag{B.5}$$

Quaternion multiplication can also be written as the second quaternion pre-multiplied by a matrix-values function of the first quaternion, i.e.:

$$\mathbf{q} \cdot \mathbf{p} = \mathbf{q}_m(\mathbf{q}, \mathbf{p}) = Q(\mathbf{q})\mathbf{p} = \overline{Q}(\mathbf{p})\mathbf{q} \tag{B.6}$$

where the quaternion matrix function, $Q : \mathbb{H} \to \mathbb{R}^{4\times4}$ is defined by:

$$Q(\mathbf{q}) = \begin{bmatrix} q_0 & -q_1 & -q_2 & -q_3 \\ q_1 & q_0 & q_3 & -q_2 \\ q_2 & -q_3 & q_0 & q_1 \\ q_3 & q_2 & -q_1 & q_0 \end{bmatrix} \tag{B.7}$$

and the conjugate quaternion matrix function $\overline{Q}$ is define by:

$$\overline{Q}(\mathbf{q}) = \begin{bmatrix} q_0 & -q_1 & -q_2 & -q_3 \\ q_1 & q_0 & -q_3 & q_2 \\ q_2 & q_3 & q_0 & -q_1 \\ q_3 & -q_2 & q_1 & q_0 \end{bmatrix} \tag{B.8}$$

B.2. Quaternions and angular rates

The attitude of a rigid body can be represented by a unit quaternion. Considering a vector $\mathbf{z} \in \mathbb{R}^3$ in the global coordinates and $\mathbf{z}' \in \mathbb{R}^3$ the vector in the body-fixed coordinates, then the following relation holds:

$$\begin{aligned} \begin{bmatrix} 0 \\ \mathbf{z}' \end{bmatrix} &= \mathbf{q} \begin{bmatrix} 0 \\ \mathbf{z} \end{bmatrix} \mathbf{q}^{-1} \\ &= \mathbf{q} \begin{bmatrix} 0 \\ \mathbf{z} \end{bmatrix} \overline{\mathbf{q}} \\ &= \overline{Q}(\mathbf{q})^T Q(\mathbf{q}) \begin{bmatrix} 0 \\ \mathbf{z} \end{bmatrix} \end{aligned} \tag{B.9}$$

The quaternion rates $\dot{\mathbf{q}}$ are related to the angular rate and can be determined by taking the time derivative of a unit quaternion. The function that maps a unit quaternion and its temporal derivative to the angular rate in body-fixed coordinates is $\omega_q : \mathbb{H} \times \mathbb{R}^4 \to \mathbb{R}^3$ and defined as:

$$\begin{bmatrix} 0 \\ \omega_q(\mathbf{q}, \dot{\mathbf{q}}) \end{bmatrix} = 2\overline{\mathbf{q}} \cdot \dot{\mathbf{q}} = 2Q(\mathbf{q})^T \dot{\mathbf{q}} \tag{B.10}$$

or more compactly:

$$\omega_q(\mathbf{q}, \dot{\mathbf{q}}) := 2W(\mathbf{q})\dot{\mathbf{q}} \tag{B.11}$$

where the quaternion rate matrix $W : \mathbb{H} \to \mathbb{R}^{3\times 4}$ is defined by:

$$W(\mathbf{q}) = \begin{bmatrix} -q_1 & q_0 & -q_3 & q_2 \\ -q_2 & q_3 & q_0 & -q_1 \\ -q_3 & -q_2 & q_1 & q_0 \end{bmatrix} \tag{B.12}$$

The inverse mapping, i.e. to derive quaternion rates from angular rates and the unit quaternion is the function $\mathbf{q}_\omega : \mathbb{H} \times \mathbb{R}^3 \to \mathbb{R}^4$ defined as:

$$\dot{\mathbf{q}}_\omega(\mathbf{q}, \omega) = \frac{1}{2}\mathbf{q} \cdot \begin{bmatrix} 0 \\ \omega \end{bmatrix} = \frac{1}{2} Q(\mathbf{q}) \begin{bmatrix} 0 \\ \omega \end{bmatrix} \tag{B.13}$$

which is also equal to:

$$\dot{\mathbf{q}}_\omega(\mathbf{q}, \omega) := \frac{1}{2} W(\mathbf{q})^T \omega \tag{B.14}$$

Another representation used in the literature to relate quaternion rates to angular rates is [Groves, 2008]:

$$\dot{q}_{A\to B} = q_{A\to B} \mathbf{W}^B_{A,B} \tag{B.15}$$

where the quaternion $q_{A\to B}$ represents the rotation from reference frame A to reference frame B and $\mathbf{W}^B_{A,B}$ is a vector that contains the angular rates:

$$\mathbf{W}^B_{A,B} = \begin{bmatrix} 0 & \omega^B_{A,B,x}/2 & \omega^B_{A,B,y}/2 & \omega^B_{A,B,z}/2 \end{bmatrix}^T \tag{B.16}$$

where $\omega^B_{A,B}$ is the angular rate vector describing the rate of rotation of the B-frame axes with respect to a stationary A-frame axes, resolved about the B-frame axes.

B.3. Quaternions and angular acceleration

Furthermore, a relation exists between the angular acceleration, expressed in the global and body-fixed coordinate frame, and the quaternion time derivatives, that is given by:

$$\begin{aligned} \begin{bmatrix} 0 \\ \dot{\omega} \end{bmatrix} &= 2\overline{\mathbf{q}} \cdot \ddot{\mathbf{q}} + 2 \begin{bmatrix} \|\dot{q}\|^2 \\ 0 \end{bmatrix} \\ &= 2Q(\mathbf{q})^T \ddot{\mathbf{q}} + 2 \begin{bmatrix} \|\dot{q}\|^2 \\ 0 \end{bmatrix} \end{aligned} \tag{B.17}$$

or more compactly:

$$\dot{\omega}_q(\mathbf{q}, \dot{\mathbf{q}}) := 2W(\mathbf{q})\ddot{\mathbf{q}} \tag{B.18}$$

The inverse mapping, i.e. to derive the second derivative of the quaternion from angular accelerations, is given by:

$$\ddot{\mathbf{q}}_\omega(\mathbf{q}, \dot{\omega}) := \frac{1}{2} W(\mathbf{q})^T \dot{\omega} \tag{B.19}$$

B.4. Hamilton versus Shuster quaternion multiplication

The Hamilton and Shuster quaternion multiplication is a salient aspect in the algebraic properties of quaternions, because if the convention used is not specified, it could lead to completely different rotations. According to Hamilton's multiplication, the product of two quaternions, $\mathbf{q}\odot\mathbf{p}$, corresponds to the product of two corresponding direction cosine matrices (DCM), $\mathbf{C}_S$, but with reversed order. In equation form, this can be written as

$$\forall \mathbf{q},\mathbf{p} \in \mathscr{U} : \mathbf{C}_S(\mathbf{q}\odot\mathbf{p}) = \mathbf{C}_S(\mathbf{p})\cdot\mathbf{C}_S(\mathbf{q}) \tag{B.20}$$

which means that the mapping from DCMs to unit length quaternions is not a homomorphism, but an anti-homomorphism. Therefore, the Shuster's solution to this problem was introduced, for which the quaternion multiplication is defined as

$$\mathbf{q}\otimes\mathbf{p} := \mathbf{p}\odot\mathbf{q} \;\Rightarrow\; \mathbf{C}_S(\mathbf{q}\otimes\mathbf{p}) = \mathbf{C}_S(\mathbf{q})\cdot\mathbf{C}_S(\mathbf{p}) \tag{B.21}$$

For the GRACE-FO mission, the Shuster's method is used to convert a unit quaternion to its rotation matrix representation. For more information about the Hamilton and the Shuster methods the reader is referred to Sommer et al. [2018].

Bibliography

Abich, K., Abramovici, A., Amparan, B., Baatzsch, A., Okihiro, B. B., Barr, D. C., Bize, M. P., Bogan, C., Braxmaier, C., Burke, M. J., Clark, K. C., Dahl, C., Dahl, K., Danzmann, K., Davis, M. A., De Vine, G., Dickson, J. A., Dubovitsky, S., Eckardt, A., … Zimmermann, M. (2019). In-Orbit Performance of the GRACE Follow-on Laser Ranging Interferometer. *Physical Review Letters*, *123*, 31101. https://doi.org/10.1103/PhysRevLett.123.031101

Airbus Defense and Space. (2020). Astrix 120. https://www.airbus.com/en/products-services/space/equipment/avionics/astrix-inertial-measurement-iru-series. Accessed: 22-22-2022

Anlauf, H., Pingel, D., & Rhodin, A. (2011). Assimilation of GPS radio occultation data at DWD. *Atmospheric Measurement Techniques*, *4*(6), 1105–1113. https://doi.org/10.5194/amt-4-1105-2011

Bandikova, T. (2015). *The role of attitude determination for inter-satellite ranging* (Dissertation) [ISBN: 978-3-7696-5170-6]. Wissenschaftliche Arbeiten der Fachrichtung Geodäsie und Geoinformatik der Leibniz Universität Hannover, Nr. 318.

Bandikova, T., & Flury, J. (2014). Improvement of the GRACE star camera data based on the revision of the combination method. *Advances in Space Research*, *54*(9), 1818–1827. https://doi.org/10.1016/j.asr.2014.07.004

Bar-itzhack, I. Y., & Harman, R. R. (2002). In-Space Calibration of a Skewed Gyro Quadruplet. *Guidance, Control, and Dynamics*, *25*(5). https://doi.org/10.2514/2.4978

Castini, G., & Cesare, S. (2008). *Gradiometer On-Orbit Calibration Procedure Analysis* (tech. rep.) [GO-TN-AI-0069]. Alenia Aerospazio.

Christophe, B., Boulanger, D., Foulon, B., Huynh, P. A., Lebat, V., Liorzou, F., & Perrot, E. (2015). A new generation of ultra-sensitive electrostatic accelerometers for GRACE Follow-on and towards the next generation gravity missions. *Acta Astronautica*, *117*, 1–7. https://doi.org/10.1016/j.actaastro.2015.06.021

Diebel, J. (2006). Representing Attitude: Euler Angles, Unit Quaternions, and Rotation Vectors. *Matrix*, *58*.

Eisenman, A. R., & Liebe, C. C. (1998). The advancing state-of-the-art in second generation star trackers. *1998 IEEE Aerospace Conference Proceedings (Cat. No.98TH8339)*, *1*, 111–118. https://doi.org/10.1109/AERO.1998.686810

Gath, P. (2016). *Integration und Test der GRACE Follow-On Satelliten* (tech. rep.) [DocumentID: 420305]. Deutscher Luft- und Raumfahrtkongress, 2016.

Gomez, A., Perosanz, F., Sacleux, B., Biancale, R., Balmino, G., Foulon, B., & Touboul, P. (2007). ELECTROSTATIC ACCELEROMETER AS AN ADVANTAGEOUS COMPONENT OF PRECISE ATTITUDE AND ORBIT CONTROL SYSTEM. *IFAC Proceedings Volumes*, *40*, 259–264. https://doi.org/10.3182/20070625-5-FR-2916.00045

Goswami, S., Francis, S. P., Bandikova, T., & Spero, R. E. (2021). Analysis of GRACE Follow-On Laser Ranging Interferometer Derived Inter-Satellite Pointing Angles. *IEEE Sensors Journal*, *21*(17), 19209–19221. https://doi.org/10.1109/JSEN.2021.3090790

Groves, P. D. (2008). *Principles of GNSS, Inertial, and Multisensor Integrated Navigation Systems* (1st edition). Artech House. Boston/London.

Haagmans, R., Siemes, C., Massotti, L., Carraz, O., & Silvestrin, P. (2020). ESA's next-generation gravity mission concepts. *Rendiconti Lincei*, *31*, 15–25. https://doi.org/10.1007/s12210-020-00875-0

Harvey, N. (2016). GRACE star camera noise. *Advances in Space Research*, *58*(3), 408–414. https://doi.org/10.1016/j.asr.2016.04.025

Harvey, N., & Sakumura, C. (2019). Results from a GRACE/GRACE-FO attitude reconstruction Kalman filter. *Journal of Geodesy*, *93*(10), 1881–1896. https://doi.org/10.1007/s00190-019-01289-z

Herceg, M., Jørgensen, P., & Jørgensen, J. (2017). Characterization and compensation of thermo-elastic instability of SWARM optical bench on micro Advanced Stellar Compass attitude observations. *Acta Astronautica*, *137*, 205–213. https://doi.org/https://doi.org/10.1016/j.actaastro.2017.04.018

Horwath, M., Lemoine, J. M., Biancale, R., & Bourgogne, S. (2011). Improved GRACE science results after adjustment of geometric biases in the Level-1B K-band ranging data. *Journal of Geodesy*, *85*(1), 23–38. https://doi.org/10.1007/s00190-010-0414-2

Jafari, M. (2015). Optimal redundant sensor configuration for accuracy increasing in space inertial navigation system. *Aerospace Science and Technology*, *47*, 467–472. https://doi.org/10.1016/j.ast.2015.09.017

Jekeli, C. (2001). *Inertial Navigation Systems with Geodetic Applications*. Walter de Gruyter. Berlin, Boston, 2001.

Jørgensen, P., Jørgensen, J., Denver, T., & van den Braembuche, P. (2012). The Micro Advanced Stellar Compass for ESA'S Proba 2 Mission. *Small Satellites for Earth Observation*, (1), 299–303. https://doi.org/10.1515/9783110919806.299

JPL GRACE-FO project. (2019). GRACE-FO Level-1A Release version 4.0 from JPL in ASCII. https://podaac.jpl.nasa.gov/dataset/GRACEFO_L1A_ASCII_GRAV_JPL_RL04 . Accessed 15-10-2020

Klinger, B., & Mayer-Gürr, T. Combination of GRACE star camera and angular acceleration data. In: *EGU General Assembly 2014. Vol. 16*. Geophysical Research Abstracts. 2014.

Kornfeld, R. P., Arnold, B. W., Gross, M. A., Dahya, N. T., Klipstein, W. M., Gath, P. F., & Bettadpur, S. (2019). GRACE-FO: The gravity recovery and climate experiment follow-on mission. *Journal of Spacecraft and Rockets*, *56*(3), 931–951. https://doi.org/10.2514/1.A34326

Landerer, F. W., Flechter, F., Save, H., Dahle, C., & Watkins, M. (2020). *GRACE Follow-On Science Data System Newsletter* (tech. rep.) [Aug / Sep 2020 (No. 15)]. NASA Jet Propulsion Laboratory, California Institute of Technology.

Landerer, F. W., Flechtner, F. M., Save, H., Webb, F. H., Bandikova, T., Bertiger, W. I., Bettadpur, S. V., Byun, S. H., Dahle, C., Dobslaw, H., Fahnestock, E., Harvey, N., Kang, Z., Kruizinga, G. L., Loomis, B. D., McCullough, C., Murböck, M., Nagel, P., Paik, M., ... Yuan, D. N. (2020). Extending the Global Mass Change Data Record: GRACE Follow-On Instrument and Science Data Performance. *Geophysical Research Letters*, *47*(12), 1–10. https://doi.org/10.1029/2020GL088306

Liebe, C. C. (2002). Accuracy performance of star trackers - a tutorial. *IEEE Transactions on Aerospace and Electronic Systems*, *38*(2), 587–599. https://doi.org/10.1109/TAES.2002.1008988

Mandea, M., Holschneider, M., Lesur, V., & Lühr, H. (2010). The Earth's Magnetic Field at the CHAMP Satellite Epoch. *System Earth via Geodetic-Geophysical Space Techniques* (pp. 475–526). Springer Berlin Heidelberg. https://doi.org/10.1007/978-3-642-10228-8_42

Markley, F. L., & Crassidis, J. L. (2014). *Fundamentals of Spacecraft Attitude Determination and Control*. Springer. New York, 2014.

Massotti, L., Siemes, C., March, G., Haagmans, R., & Silvestrin, P. (2021). Next Generation Gravity Mission Elements of the Mass Change and Geoscience International Constellation: From Orbit Selection to Instrument and Mission Design. *Remote Sensing*, *13*(19). https://doi.org/10.3390/rs13193935

McCullough, C. M., Harvey, N., Save, H., & Bandikova, T. (2019). *Description of Calibrated GRACE-FO Accelerometer Data Products (ACT)* (tech. rep.) [JPL D-103863]. Jet Propulsion Laboratory, California Institute of Technology.

Muller, V. (2013). *Simulations for LISA & GRACE-Follow-On: Satellite constellations at Lagrangian points for LISA-like missions - Interferometer simulations for the GRACE Follow-On mission* (Master Thesis). Gottfried Wilhelm Leibniz Universität Hannover. https://www.vimu.de/thesis/Mueller-Master-Thesis.pdf. Accessed 10-10-2020.

NASA/JPL-Caltech. (2020). Grace-fo rendering. https://gracefo.jpl.nasa.gov/resources/36/grace-fo-rendering/ . Accessed 29-10-2020

National Academies of Sciences, Engineering & Medicine. (2018). *Thriving on our changing planet: A decadal strategy for earth observation from space*. The National Academies Press. Washington, DC. https://doi.org/10.17226/24938

Pail, R., Bingham, R., Braitenberg, C., Dobslaw, H., Eicker, A., Güntner, A., Horwath, M., Ivins, E., Longuevergne, L., Panet, I., & Wouters, B. (2015). Science and User Needs for Observing Global Mass Transport to Understand Global Change and to Benefit Society. *Surveys in Geophysics*, *36*(6), 743–772. https://doi.org/10.1007/s10712-015-9348-9

Pingel, D., Rhodin, A., Wergen, W., Tomassini, M., Gorbunov, M., & Wickert, J. (2010). Assimilation of CHAMP and GRACE-A Radio Occultation Data in the GME Global Meteorological Model of the German Weather Service. *System Earth via Geodetic-Geophysical Space Techniques* (pp. 461–471). Springer. Berlin, Heidelberg. https://doi.org/10.1007/978-3-642-10228-8_41

Pittelkau, M. E. (2005). Calibration and Attitude Determination with Redundant Inertial Measurement Units. *Guidance, Control, and Dynamics*, *28*(4). https://doi.org/10.2514/1.7040

Romans, L. (2003). Optimal combination of quaternions from multiple star cameras. https://podaac-tools.jpl.nasa.gov/drive/files/allData/grace/docs/quaternion_memo.pdf . Accessed 10-10-2020

Rummel, R., Balmino, G., Johannessen, J., Visser, P., & Woodworth, P. (2002). Dedicated gravity field missions - principles and aims. *Journal of Geodynamics*, *33*(1-2), 3–20. https://doi.org/10.1016/S0264-3707(01)00050-3

Saptari, V. (2003). *Fourier Transform Spectroscopy Instrumentation Engineering*. SPIE Optical Engineering Press. Bellingham, Washington, 2003. https://doi.org/https://doi.org/10.1117/3.523499

Schütze, D., Stede, G., Müller, V., Gerberding, O., Bandikova, T., Sheard, B. S., Heinzel, G., & Danzmann, K. (2014). Laser beam steering for GRACE Follow-On intersatellite interferometry. *Optics Express*, *22*(20), 24117–24132. https://doi.org/10.1364/oe.22.024117

Sheard, B. S., Heinzel, G., Danzmann, K., Shaddock, D. A., Klipstein, W. M., & Folkner, W. M. (2012). Intersatellite laser ranging instrument for the GRACE follow-on mission. *Journal of Geodesy*, *86*(12), 1083–1095. https://doi.org/10.1007/s00190-012-0566-3

Siemes, C. (2018). *GOCE Level 1B Gravity Gradient Processing Algorithms* (tech. rep.) [ESA-EOPSM-GOCE-TN-3397]. ESA.

Siemes, C., Rexer, M., & Haagmans, R. (2018). GOCE star tracker attitude quaternion calibration and combination. *Advances in Space Research*, *63*(3), 1133–1146. https://doi.org/10.1016/j.asr.2018.10.030

Siemes, C., Rexer, M., Schlicht, A., & Haagmans, R. (2019). GOCE gradiometer data calibration. *Journal of Geodesy*, *93*(9), 1603–1630. https://doi.org/10.1007/s00190-019-01271-9

Sommer, H., Gilitschenski, I., Bloesch, M., Weiss, S., Siegwart, R., & Nieto, J. (2018). Why and how to avoid the flipped quaternion multiplication. *Aerospace*, *5*(3), 72. https://doi.org/10.3390/aerospace5030072

Stummer, C., Fecher, T., & Pail, R. (2011). Alternative method for angular rate determination within the GOCE gradiometer processing. *Journal of Geodesy*, *85*(9), 585–596. https://doi.org/10.1007/s00190-011-0461-3

Stummer, C., Siemes, C., Pail, R., Frommknecht, B., & Floberghagen, R. (2012). Upgrade of the GOCE Level 1b gradiometer processor. *Advances in Space Research*, *49*(4), 739–752. https://doi.org/10.1016/j.asr.2011.11.027

Teunissen, P. J. G. (2003). *Adjustment theory* (Vol. Series on Mathematical Geodesy and Positioning). DUP Blueprint. Delft, 2003.

Teunissen, P. J. G., & Montenbruck, O. (2017). *Springer Handbook Global Navigation Satellite Systems* (1st edition). Springer International Publishing. Switzerland, 2017. https://doi.org/10.1007/978-3-319-42928-1

Touboul, P., Foulon, B., Christophe, B., & Marque, J. P. CHAMP, GRACE, GOCE Instruments and Beyond. In: *Kenyon S., Pacino M., Marti U. (eds) Geodesy for Planet Earth: Proceedings of the 2009 IAG Symposium. 136*. Springer, Berlin, Heidelberg, 2009. https://doi.org/10.1007/978-3-642-20338-1_26.

Touboul, P., Foulon, B., Rodrigues, M., & Marque, J. P. (2004). In orbit nano-g measurements, lessons for future space missions. *Aerospace Science and Technology*, *8*(5), 431–441. https://doi.org/10.1016/j.ast.2004.01.006

Wegener, H., Müller, V., Heinzel, G., & Misfeldt, M. (2020). Tilt-to-Length Coupling in the GRACE Follow-On Laser Ranging Interferometer. *Journal of Spacecraft and Rockets*, *57*(6), 1362–1372. https://doi.org/10.2514/1.A34790

Wen, H. Y., Kruizinga, G. L. H., Paik, M., Landerer, F. W., Bertiger, W. I., Sakumura, C., Bandikova, T., & McCullough, C. (2019). *Gravity Recovery and Climate Experiment Follow-On (GRACE-FO) Level-1 Data Product User Handbook* (tech. rep.) [JPL D-56935]. NASA Jet Propulsion Laboratory, California Institute of Technology.